DYNAMIC MICROMECHANICAL FABRY–PÉROT CAVITY SENSORS FABRICATED BY MULTIPHOTON ABSORPTION ONTO OPTICAL FIBER TIPS

THESIS

Jeremiah C. Williams, 2d Lt, USAF

AFIT-ENG-MS-20-M-074

DEPARTMENT OF THE AIR FORCE
AIR UNIVERSITY

AIR FORCE INSTITUTE OF TECHNOLOGY

Wright-Patterson Air Force Base, Ohio

AFIT-ENG-MS-20-M-074

DYNAMIC MICROMECHANICAL FABRY–PÉROT CAVITY SENSORS FABRICATED BY MULTIPHOTON ABSORPTION ONTO OPTICAL FIBER TIPS

THESIS

Presented to the Faculty

Department of Electrical and Computer Engineering

Graduate School of Engineering and Management

Air Force Institute of Technology

Air University

Air Education and Training Command

in Partial Fulfillment of the Requirements for the

Degree of Master of Science in Electrical Engineering

Jeremiah C. Williams, B.S.M.E.

2d Lt, USAF

March 26, 2020

AFIT-ENG-MS-20-M-074

DYNAMIC MICROMECHANICAL FABRY–PÉROT CAVITY SENSORS FABRICATED BY MULTIPHOTON ABSORPTION ONTO OPTICAL FIBER TIPS

THESIS

Jeremiah C. Williams, B.S.M.E.
2d Lt, USAF

Committee Membership:

Dr. Hengky Chandrahalim, Ph.D
Chair

Maj. Tod V. Laurvick, Ph.D
Member

Dr. Michael A. Marciniak, Ph.D
Member

Dr. Nicholas G. Usechak, Ph.D
Member

Dr. Joseph S. Suelzer, Ph.D
Member

AFIT-ENG-MS-20-M-074

Abstract

This thesis presents research into low size, weight, and power (SWAP) sensors fabricated by two-photon polymerization (2PP) micro-fabrication onto the cleaved ends of optical fibers. The 3D freedom afforded by this technique is leveraged to create devices with dynamic mechanical features. Integration with low-loss optical fibers allows these devices to be conveniently operated remotely from any analytical equipment by long distances. Three monolithically integrated devices are included in this work: a mechanically enabled Fabry–Pérot (FP) cavity refractive index (RI) sensor, a high-deflection spring-body pressure sensor, and a micro-anemometer flow sensor. The RI sensor utilized a multi-position hemispherical mirror to enable reflective coating deposition by traditional micro-fabrication techniques. It also demonstrated multi-purpose sensing of liquid RI, air temperature, and vacuum pressure. The spring-body pressure sensor demonstrated a measurable deflection in response to ambient pressure, and achieved a high sensitivity. It also realized complex geometries in the spring body, multi-positional mirror cap, and adhesive retaining features that can only be fabricated at this scale with 2PP micro-fabrication. The micro-anemometer flow sensor showcased a spinning rotor with three integrated mirrors and a speed determined by incident flow. The device demonstrated a wide range and fine resolution, and highlighted the iterative design process enabled by 2PP micro-fabrication. These devices represent successful technology demonstrates for future work in low-SWAP optical sensors.

Acknowledgements

I would like to express my sincere gratitude to my academic advisor, Dr. Hengky Chandrahalim for his expert guidance and relentless support throughout this work. His outstanding dedication at any hour made these achievements possible. I would also like to thank Dr. Joseph Suelzer Dr. Nicholas Usechak for their assistance with and generous access to the advanced facilities at AFRL, in addition to their extremely helpful input to my work. Thanks as well to Maj. Tod Laurvick and Dr. Micahel Marciniak for joining my committee and providing outstanding feedback on my thesis.

Additionally, I would like to express my appreciation to Richard Johnston and Adam Fritzschefor for providing training in the AFIT cleanroom and dedicated support to even the most cantankerous equipment. I would also like to thank Dr. Abigail Juhl for training on the Nanoscribe at AFRL, and Ecklin Crenshaw for his technical assistance and stimulating conversation during the hours spent fabricating these devices. Also from AFRL, I would like to thank Dr. Kevin Leedy, Jason Hickey, and Andrew Browning for their time and help depositing reflective coatings to get my research started.

Finally, I would like to thank my friends and family for their unending support and encouragement throughout this research. In particular, I could not have gotten here without the dedication and love of my amazing wife, thank you for everything.

Jeremiah Williams

Table of Contents

Page

List of Figures

Figure Page

List of Tables

DYNAMIC MICROMECHANICAL FABRY–PÉROT CAVITY SENSORS FABRICATED BY MULTIPHOTON ABSORPTION ONTO OPTICAL FIBER TIPS

I. Introduction

1.1 Motivation

Modern technology has been spurred foreword by the advancement and miniaturization of sensors. It is paramount to observe and quantify environmental phenomenon for automation and intelligent decision making. Sensors are the eyes and ears of a mechanical system, and the more information they can gather, the better. Automation can only be achieved safely if there is sufficient data and feedback to correct errors, and the more data that can be gathered for decision makers, the greater their situational awareness. Like all components, sensors must carefully balance their size, weight, and power (SWAP) with their performance. Lowering the SWAP of sensors without sacrificing utility and accuracy can free up power and weight on sensitive platforms such as aircraft and satellites for other hardware. Furthermore, smaller sensors can interrogate more individual points before overlapping with one another. An array of small, inexpensive sensors can provide a more complete picture of a situation than a single, large, high-quality sensor. Developing low SWAP sensors can bring these benefits to defense technology.

This research explores one promising fabrication technique for creating low SWAP sensors, two-photon polymerization (2PP) micro-fabrication. This process is able to create unprecedented sub-micron resolution 3D mechanical structures easily and

quickly. Capt John Smith, a previous Air Force Institute of Technology (AFIT) graduate, was able to integrate 2PP micro-fabrication with low loss optical fibers at the Air Force Research Laboratory (AFRL) located at Wright-Patterson Air Force Base (WPAFB). This work aims to expand upon Capt Smith's success to further leverage the 3D freedom afforded by this process to create low SWAP sensors for defense applications.

The first potential application of this work is a mysterious challenge currently facing the Air Force. At the time of writing, a number of pilots across several different high-performance aircraft have experienced symptoms of hypoxia (oxygen deprivation) for unknown reasons. A sensor could be integrated to the breathing mask or cockpit of affected aircraft to monitor the gas composition in real time to help discover the cause of this problem, such as the device discussed in [30]. This device is promising, but requires a large bundle of fiber optic cables and a significant hole in the pilot's mask. The first device discussed in this reserach could lead to such a sensor that could be easily integrated with current systems. The chemical make-up of air determines its refractive index (RI), so changes in RI could be evaluated to determine the composition of air. A small, single-fiber device could also be integrated with existing architecture with very little modification. In a complex system like combat aircraft, every ounce must be accounted for, so a micron-scale sensor would require very little re-design for the new weight. The device would also need a low detection limit, able to distinguish between the very similar refractive indices of atmospheric gasses. Chapter III presents a micron-scale optical fiber tip refractive index sensor that could be further explored to meet these requirements.

The Air Force also has an interest in miniaturizing aircraft and their components. A ubiquitous parameter to monitor on an aircraft is pressure. For one, the altitude of an aircraft can be determined by the pressure of the atmosphere around it. Miniatur-

ized aircraft could self-reference their altitude with a miniaturized barometric pressure sensor to increase their autonomy. Additionally, it is critical to understand the pressure at specific points inside a jet turbine to ensure its optimal performance. Miniaturized pressure sensors could provide multiple data points inside a turbine without seriously altering the overall geometry. An improved understanding of the pressure situation inside a turbine during its operation can inform operators on how to improve its efficiency and performance. Furthermore, the extreme temperatures inside a jet engine pose a continuing challenge that warrants examining different sensing schemes. Chapter IV presents a micron-scale optical fiber environmental pressure sensor that could be explored for various pressure-sensor applications that would benefit from miniaturization.

There has also been a push in the Air Force towards in-situ monitoring of flow fields around airfoils and unmanned aerial vehicles (UAVs). For UAVs in particular, "smart wings" have been proposed that would communicate with arrays of small flow sensors to automatically adjust to gusts of wind. For this, sensors consisting of carbon nanotube forests grown onto glass fibers and inserted into a capillary tube with electrodes have been developed by AFRL [26]. While impressive devices, they require several precise fabrication steps, are currently limited to sensing low speeds, and need electrical routing. The 3D freedom of 2PP micro-fabrication could be used create a superior geometry with a wider operating range that maintains a small footprint. The number of fabrication steps could also be reduced. Additionally, a fiber optic sensor would require no electrical connections, and remain immune to EM interference. Chapter V presents a micro-anemometer that provides many of these advantages and could potentially be integrated into future smart-wings.

1.2 Assumptions/Limitations

The main limitation of this work was choosing a single fabrication technique to investigate. Several methods have been demonstrated to produce optical fiber-tip sensors, as discussed in Chapter II, but this work only considers 2PP micro-fabrication. This method requires devices be fabricated from the bottom up, and must be supported during polymerization. This greatly influenced the design of each device. Additionally, only one 2PP lithography system was used, the Nanoscribe GT Photonic Professional [31].

Testing was also limited by the timeline of this research, with the vast majority taking place at AFIT to ensure completion. The variable wavelength laser utilized had two issues that were overcome with software: its wavelength-dependent output power and the mechanical vibrations caused by its motor during a sweep. The software solutions are discussed in section 3.2. Upgrades to testing equipment such as the flow meter, vacuum chamber, and hotplate may also provide superior data, but were not implemented in the scope of this work.

General assumptions were made regarding environmental properties of the test lab, including relative humidity, ambient temperature, and atmospheric pressure. The refractive index of each test is also assumed to be constant over the bandwidth of interest. Calculations for optical properties when a specific wavelength was not known, or to generalize over a bandwidth were made at 1550 nm. This is a common telecommunications wavelength at which most of the hardware was built to operate. It is also near the center of the available bandwidth of the variable-wavelength laser.

1.3 Contributions

Contributions from this work to the defense-focused research of AFIT include:

- Demonstrated advanced capabilities of 2PP micro-fabrication, an emerging field offering unparalleled design freedom at the sub-micron scale.
- Developed a low SWAP multi-purpose mechanically enabled Fabry–Pérot (FP) cavity RI sensor with a multi-positional mirror that enables high quality thin-film depositions on complex geometries.
- Realized a microscopic high-deflection spring-body on the tip of an optical fiber that deflections in response to external ambient pressure.
- Integrated a dynamic flow sensor on the tip of an optical fiber that could be integrated with rigid air-frames for high resolution flow-field analysis.

1.4 Thesis Overview

This thesis is organized into five chapters. The second chapter presents a literature review of the primary physics utilized in this work and previously demonstrated devices comparable to those presented here. Chapters three, four, and five each describe a prototype device: a hinged FP cavity RI sensor, a hinged spring-body pressure sensor, and a rotating, micro-anemometer flow sensor. Each chapter contains the methodology of design, fabrication, and testing the device, the results of the experiments, and concluding remarks with potential future work. Figure 1 presents false-color scanning electron microscope (SEM) images of the three devices.

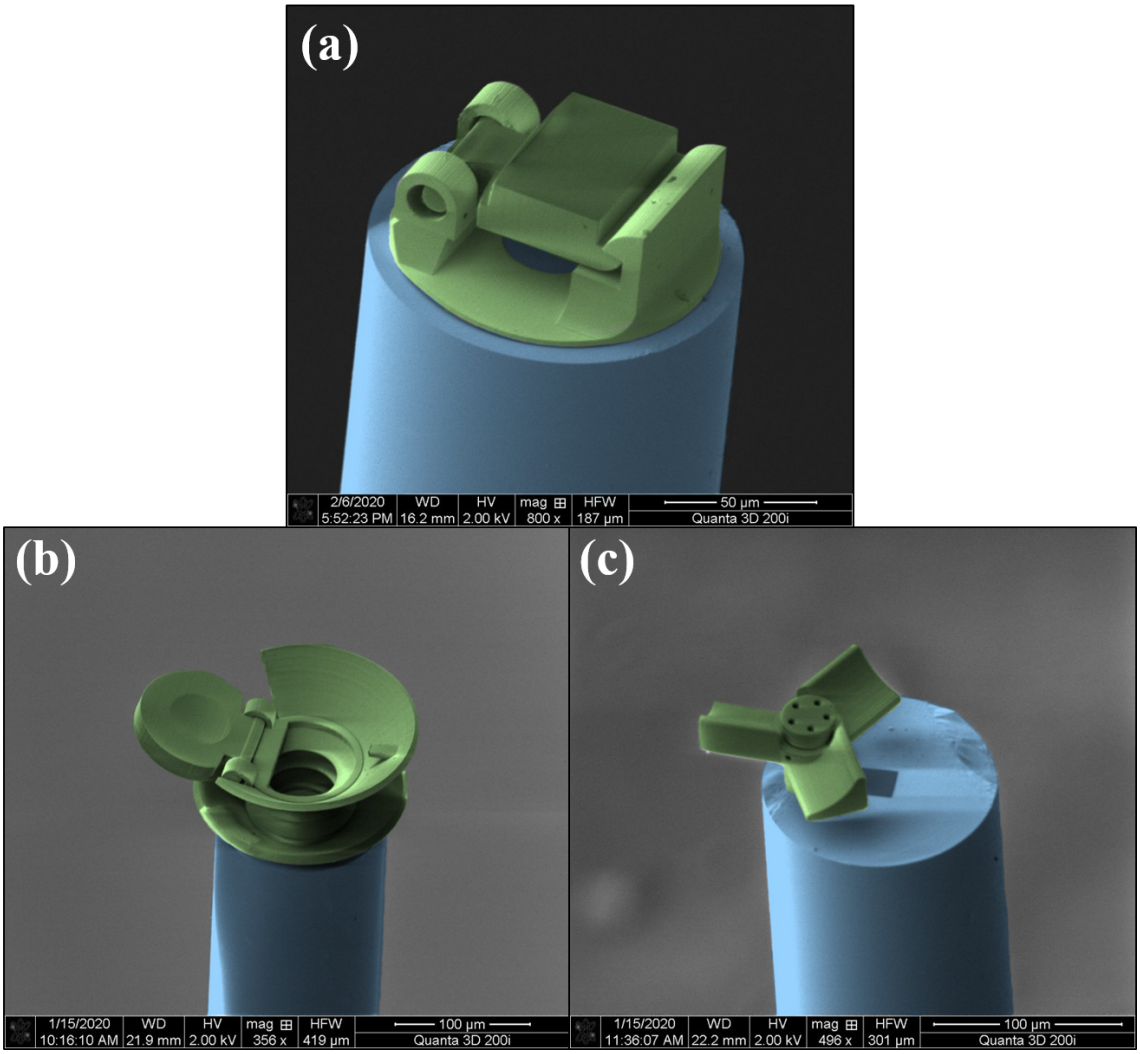

Figure 1: False color SEM images of each device. (a) Hinged FP Cavity RI sensor. (b) Hinged spring-body pressure sensor. (c) Micro-anemometer flow sensor.

II. Background and Literature Review

This chapter first explores the fundamental physics utilized in this work. These devices rely on two fundamental optical elements, the Fabry–Pérot (FP) cavity and the optical fiber. This chapter then presents the current state of the art in dual-photon stereo-lithography, the fabrication method integral to this research. This chapter also surveys examples of successful on-fiber sensors that can be compared to this work.

2.1 Optics and Physics

2.1.1 Fabry–Pérot Cavity

The FP cavity is an important optical element consisting of two optical surfaces parallel to one other, separated by some interstitial medium such as air. A portion of light incident onto the cavity transmits through the first optical element into the interstitial medium. This light is reflected multiple times inside the cavity between the two elements. The output of an FP cavity is modelled by integrating the intensity of the multiple reflections. This follows the Airy distribution, and is included in equation 1.

$$I_{out} = \frac{I_{in}(1-R)^2}{(1-R)^2 + 4Rsin^2(\delta/2)} \tag{1}$$

where δ is the phase shift experienced by one of the reflected beams on a round trip through the cavity. This is dependant on the wavelength as well as the refractive index (RI), and length of the cavity:

$$\delta = \frac{4\pi}{\lambda_0} nL \tag{2}$$

When this phase shift is a multiple of 2π, the output intensity defined by equation 1

will be its maximum, corresponding to peak transmission through the cavity. This is due to constructive interference among the reflected beams, that results in a coherent output from the cavity. This event is also known as resonance, and the constructive interference between the multiple internal reflections along the optical axis is known as the longitudinal resonance mode. The wavelengths at which this occurs can be determined by:

$$\lambda_m = \frac{2nl}{m} \tag{3}$$

where m is the integer longitudinal mode order, n is the RI of the interstitial medium, and l is the length of the FP cavity [32]. Non-resonant wavelengths are reflected by the cavity. This leads to the traditional wavelength-dependent transmission spectrum seen in figure 3. A FP laser cavity is made by inserting a gain medium such as a gas, semiconductor, or opto-fluidic dye, into an FP cavity. Input light excites optical resonance inside the gain medium which constructively interferes with its own emissions to create a coherent transmission out of the cavity in the form of a laser beam [33].

The FP cavity has several key aspects that make it a powerful tool for micro-optics.

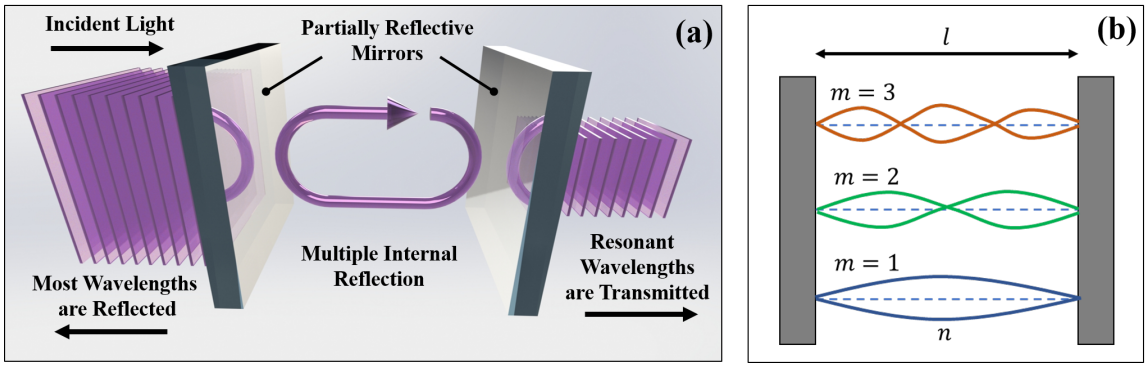

Figure 2: Graphic depicting the optical behavior of a FP cavity resonator, (a) a 3D rendering with important features annotated, (b) a 2D representation of the first three resonant modes.

The longitudinal resonance mode is tightly confined and particularly prominent, leading to a small mode volume compared to other optical resonators such as photonic crystals, distributed feedback gratings, and whispering gallery mode (WGM) ring resonators [34]. Very high quality factors have also been reported with micro-FP cavities. The quality factor of an FP cavity's response is defined as,

$$Q = \frac{\lambda_0}{\Delta\lambda_{FWHM}} \tag{4}$$

where λ_0 is the resonant wavelength of interest and $\Delta\lambda_{FWHM}$ full-width half-max (FWHM) of the peak feature. The FWHM is related to another figure of merit often used for FP cavities, the finesse. This is defined as,

$$f = \frac{\Delta\lambda_{FSR}}{\Delta_{FWHM}} \tag{5}$$

where λ_{FSR} is the distance between two resonant wavelengths, or the free spectral range (FSR). For a given resonant wavelength at normal incidence, the FSR can be predicted from the cavity properties,

$$\Delta\lambda_{FSR} = \frac{\lambda_0^2}{2nl} \tag{6}$$

where λ_0 is the resonant wavelength, l is the length of the cavity, and n is the RI of the cavity. The finesse of a cavity, and therefore the FWHM and quality factor, is related to the reflectance of the two optical elements through the coefficient of finesse:

$$f = \frac{\pi\sqrt{F}}{2} \tag{7}$$

$$F = (\frac{2\sqrt{R}}{1-R})^2 \tag{8}$$

where f is the finesse, F is the coefficient of finesse, and R is the reflectance of the cavity's optical elements [32]. Taking advantage of this relationship, highly reflective surfaces such as mirrors are desired to increase the finesse of a cavity. Auality factors as high as 10^5 have been achieved on micro-FP cavities by using stacked dielectric mirrors [35].

The cavity of a FP resonator can also be open to the environment. This allows different interstitial media to be interrogated or used as a gain medium. Additionally, the FP cavity does not require a different RI inside and outside the cavity, as is required in the ring resonator [36]. While an open cavity increases the utility of a device, it also leads to losses due to poor lateral confinement. Since it is impossible

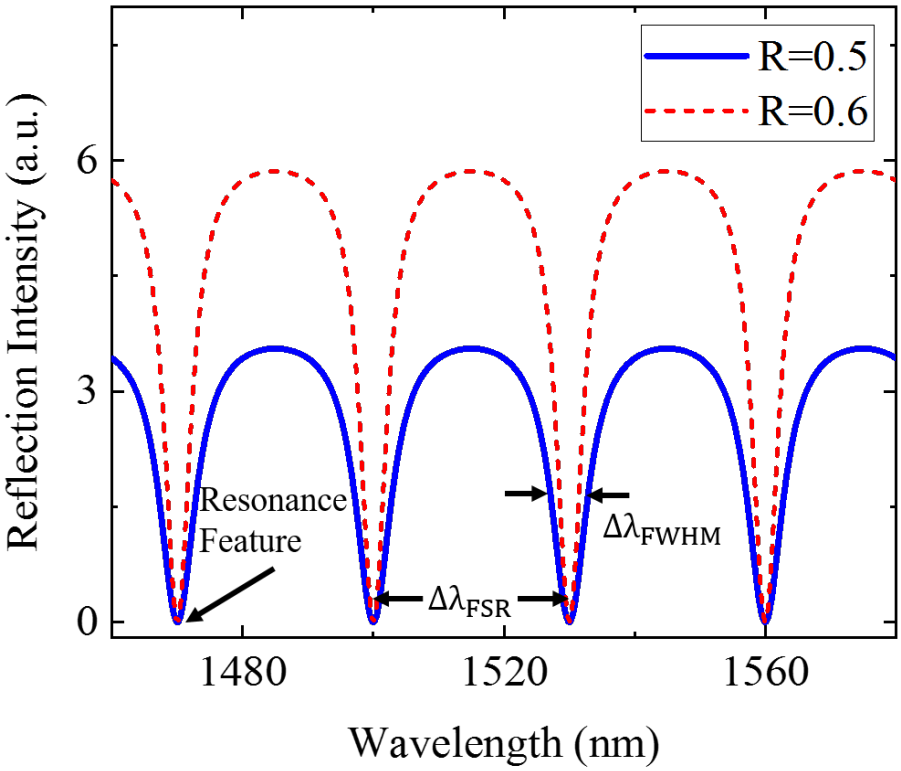

Figure 3: Generic FP Cavity Reflection Spectrum Modelled with an Airy Distribution.

to perfectly align a physical device, after several reflections resonant light eventually walks off the edge of the mirror and is lost. This problem is exacerbated when the two mirrors are misaligned. Even a few degrees of misalignment has been shown to have detrimental impact on the quality factor of a device [35]. One popular way to reduce misalignment sensitivity and improve lateral confinement is to use curved mirrors [37, 38, 36], although this usually makes fabrication more complicated. The manufacturing technique investigated in this research, two-photon polymerization (2PP) micro-fabrication, makes creating such features very simple.

These advantageous qualities have made the FP cavity the cornerstone of many exciting applications. Used as a laser cavity, researchers have examined several exotic gain mediums such as biological tissues [39], optical fluids [35, 36], and silicon nanowires [40]. Micro-Electro-Mechanical Systems (MEMS) have been integrated with an FP cavity to create both tunable optical filters [41], and miniaturized tunable lasers [42, 43]. Open FP cavities are also powerful tools for spectroscopy. They have been used in human breath analysis [44], microfluidic interrogation on a microchip [45], compact imaging spectrometers [46], and the interrogation of living cells [47]. The FP cavity is also key to cavity quantum electrodynamics (CQED), the physics behind quantum computing. It has been used to couple to a trapped atom [48], for frequency splitting of polarization eigenmodes [49, 50], and as a highly controlled photon emission source [51, 37]. Finally, the response of a FP cavity can be used to sense any phenomenon that affects the RI or length of the cavity. As shown in equations 3 and 13, both the resonant wavelengths and the FSR of the response will be affected by changes in RI and cavity length. This relationship has been used to sense many phenomenon including force [52, 8], temperature [53, 54, 11, 55, 56, 57, 58, 7, 59, 60, 61], liquid RI [62, 63], pressure [63, 18, 18, 19, 63, 59, 64, 65, 66, 56, 61], gravitational waves [67], acceleration [68], and gas composition [69]. One powerful platform for

micro-FP sensors is the optical fiber due to its low optical losses, small form factor, and well known mode structure [70].

2.1.2 Optical fibers

The optical fiber is an integral component of modern photonics. Since the late 1800s, the controlled propagation of light by total internal refraction has been demonstrated through streams of water or glass "light pipes" [33]. These early demonstrations have evolved into modern optical fibers. With the invention of the laser, guiding light has become a high priority research area for both commercial and defense applications.

To guide light, an optical fiber relies on the phenomenon of total internal reflection. This occurs when light originating inside a medium of higher RI reflects off of an interface with a medium of lower RI at an angle beyond its critical angle. Optical fibers consist of two layers of glass, a core and a cladding. The core has slightly higher RI than the cladding, thus trapping and propagating light incident to the cladding at an angle beyond its critical angle. This angle is determined by the RI of the cladding n_{cl} and the RI of the core n_{co}, [70],

$$sin\theta_c = (n_{co}^2 - n_{cl}^2)^{1/2} \tag{9}$$

Light entering the fiber below this angle is propagated within the fiber by total internal reflection between the core and the cladding. Typically, this glass is covered in a protective polymer jacket to prevent the fiber from breaking when bent. Figure 4 shows a cutaway view of a typical optical fiber with the dimensions of the fiber used in this research.

There are several types of optical fiber, defined by the properties of the light they propagate [71]. The most common commercial fibers are multimode stepped-

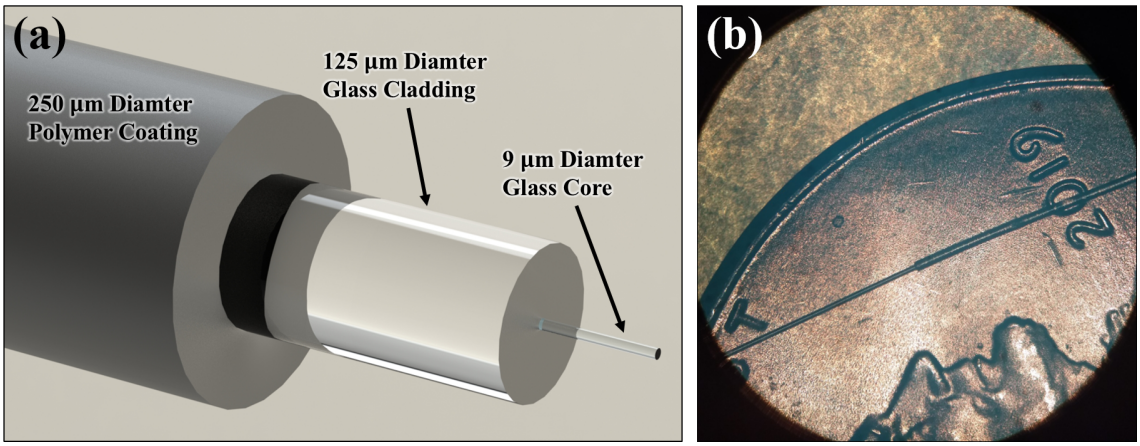

Figure 4: (a) Typical single mode fiber (SMF). The scale and dimensions represent the fiber used in this research. (b) An example of the fiber used in this research compared to a penny.

index, multimode graded-index, and single mode step index. The output and general internal geometry of these is included in figure 5. Maxwell's equations in cylindrical coordinates show that only specific modes will propagate based on the geometry of the fiber as shown in [70]. The number of propagated optical modes, the mode volume, is found to be [70]:

$$V = \frac{2\pi an}{\lambda}\sqrt{2\Delta} \tag{10}$$

$$\Delta = \frac{n_{co}^2 - n_{cl}^2}{2n_{co}^2}, \tag{11}$$

where a is the diameter of the fiber core, and λ is the wavelength of incident light. Step indexed fibers simply feature a different RI in the core and cladding. If the core is large enough to allow many modes, as is the case in multi-mode fiber, some will propagate at a slightly different angle based on their angle of incidence. This leads to different optical path lengths for different modes, resulting in a time delay upon exiting the fiber. This is a problem for data transfer, which relies on precise timing to

discern each bit of a transmission. To combat this, graded index fibers change index more gradually. This reduces the number of allowed modes by occasionally focusing the propagating light with a series of gradual refractions. The highest information bandwidth can be achieved with single mode fiber (SMF). This fiber uses a small core on the order of the wavelength of the incident light, typically $9\mu m$ for 1550nm light, to constrain the number of allowed modes. The geometry only allows light to propagate down the axis of the fiber. The conditions for single mode operation occur when equation 10 is less than 2.405 [70]. When only a single mode is present, all light exiting can be precisely timed to hold the most data. This also greatly reduces the noise from the different reactions of multiple modes when optical fibers are used as sensors [70]. This work uses SMF.

Optical fibers can achieve very low losses, which is demonstrated in their dominance of long distance telecommunications. Signals carried on ordinary copper wires must be re-amplified about every kilometer, and coaxial cables about every 2-6km.

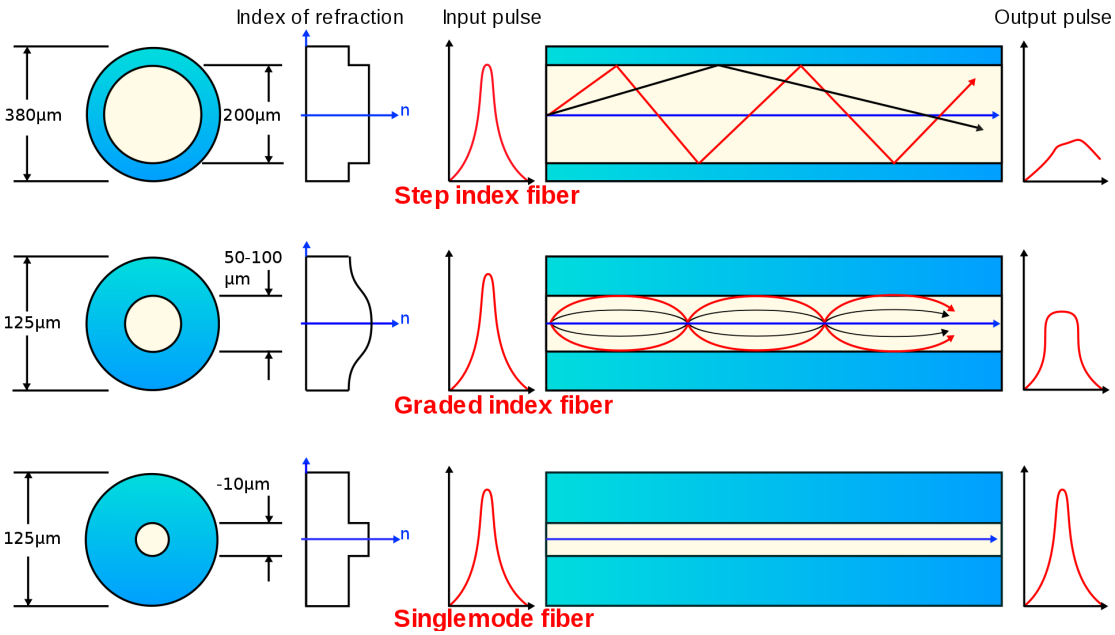

Figure 5: The three common types of commercial optical fibers [1].

Modern optical fibers require re-amplification only after 80km [33]. For fiber based sensors, this opens the possibility of extremely remote operation. The expensive and bulky analysis equipment could be centrally located kilometers away from the sensors themselves. Additionally, this efficiency leads to less bulky re-amplification hardware, giving optical fiber communications lower size, weight, and power (SWAP) than traditional wired connections. The related hardware requirement combined with the small, light, micron-scale dimensions of most fibers make them attractive for the military's low SWAP platforms such as aircraft and satellites [71].

Fiber optics are also capable of carrying more information than electrical, radio, or even microwave communications. This is because the available bandwidth of a communication system increases with the frequency of the carrier signal. The high frequency (small wavelength) light used for optical fibers can, in theory, exceed the information capacity of microwave communications by a factor of 10^5 [71]. The Pacific Light Cable Network Fiber, a submarine transpacific data link, transmits 144 tera-bits/s using six pairs of commercial fiber optic cables [72]. In the state of the art, researchers have been able to reach a record 10 peta-bits/s over 11.3km using a single highly customized multi-core fiber [73].

Fiber optics are also immune to electromagnetic (EM) interference and the effects of EM pulses, making them more robust than electrical signal carrying wires [71]. This is particularly valuable to military applications, where communication lines may be targeted by EM attacks. Fiber optic communication is also highly secure. While radio and microwave signals can be intercepted passively and discretely, the light propagated by an optical fiber is entirely contained. The line would need to be cut into by an eavesdropper, immediately notifying the intended recipient the communication was being tampered with when they failed to receive the message [71]. This is beneficial to military systems where the security of real-time data can be key to

battlefield success. Such benefits make fiber optics an attractive possible compliment to wireless communication for secure military communications.

2.1.3 Two-Photon Polymerization (2PP) Microfabrication

An important enabling technology for this work is 2PP microfabrication. This technique begins with a drop of photosensitive resin placed on a substrate. The chemical make-up of the resin allows it to polymerize into a solid, but only when exposed to a high threshold energy. Single photon absorption is often achieved in stereolithography 3D printing with ultraviolet (UV) light. Any resin in contact with the beam absorbs enough energy to crosslink and solidify. Thus structures can be built layer-by-layer by scanning a UV laser through the resin. The same energy can be imparted to the resin with two photons from a high intensity visible light source, at double the wavelength of the UV light. The power distribution inside the beam capable of initiating this reaction is a nonlinear function of the distance from the focal point. Thus, only the very center of the beam's focal point will have enough energy to initiate 2PP and crosslink the resin [74]. A graphic depicting the reduced size of the reaction site is included in figure 6. Advances in femtosecond laser technology provided an ideal laser source which can be focused to small diameter beams at high intensity and pulsed with precise timing. The three-dimensional reaction site is called the "voxel," a 3D equivalent of the pixel. The voxel size represents the resolution of a 2PP microfarication system. The equipment used in this work, the Nanoscribe GT Photonic Professional, could achieve a voxel size of 200nm $\times$ 200nm $\times$ 200nm with the recommended settings.

To guide the laser, software known as a slicer deconstructs a 3D model into layers, which are polymerized one at a time to construct the desired structure surrounded by undeveloped liquid resin. This resin is rinsed away in solvents, leaving behind

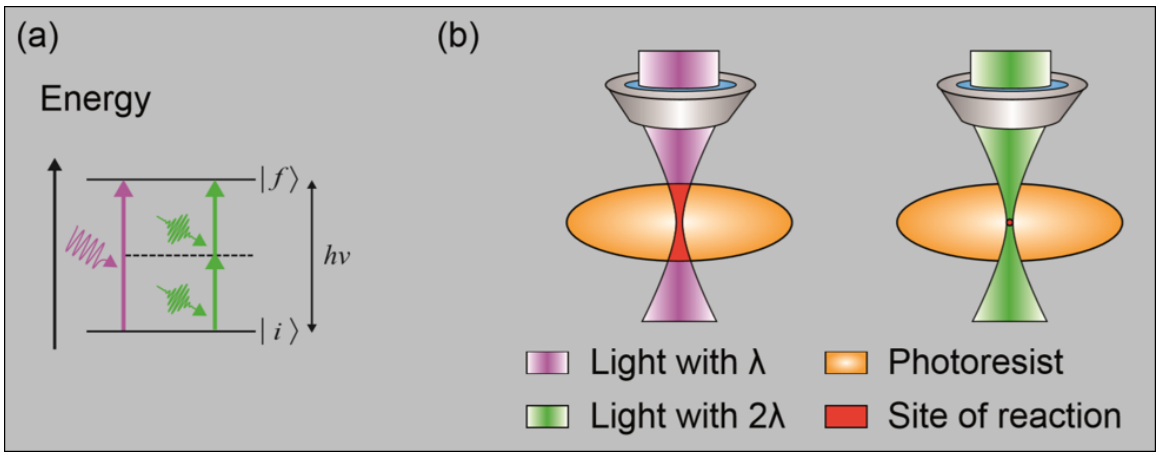

Figure 6: A graphic depicting (a) the energy imparted by traditional UV light and by two-photon polymerization and (b) the significantly smaller reaction site during 2PP microfabrication [2]

.

the solidified structure. This technique allows for true 3D freedom compared to the planar semiconductor fabrication techniques often used in MEMS fabrication. Previously impossible models and mechanical parts have been demonstrated on a sub-micron scale. Arbitrary curved geometries such as statues and figurines are shown in [4] and [75]. Meta-materials can be made with new shapes, not achievable with any other method. Recent examples are collected in [76]. Devices made by 2PP have demonstrated high optical quality and can be integrated with complementary metal oxide semiconductor (CMOS) technology as demonstrated by the compound microlenses in [5]. There have even been impressive demonstrations of remote control of moving parts such as gears and levers by optical force [3], and magnetically by polymerizing a ferrofluid resin [77]. Figure 7 includes reproduced images of several of these impressive devices.

2.1.4 Two-Photon Polymerization onto Optical Fibers

Optical fibers present a natural and powerful platform for 2PP micro-fabrication. A fiber's optical signal can easily interact with the polymer structures, the end of

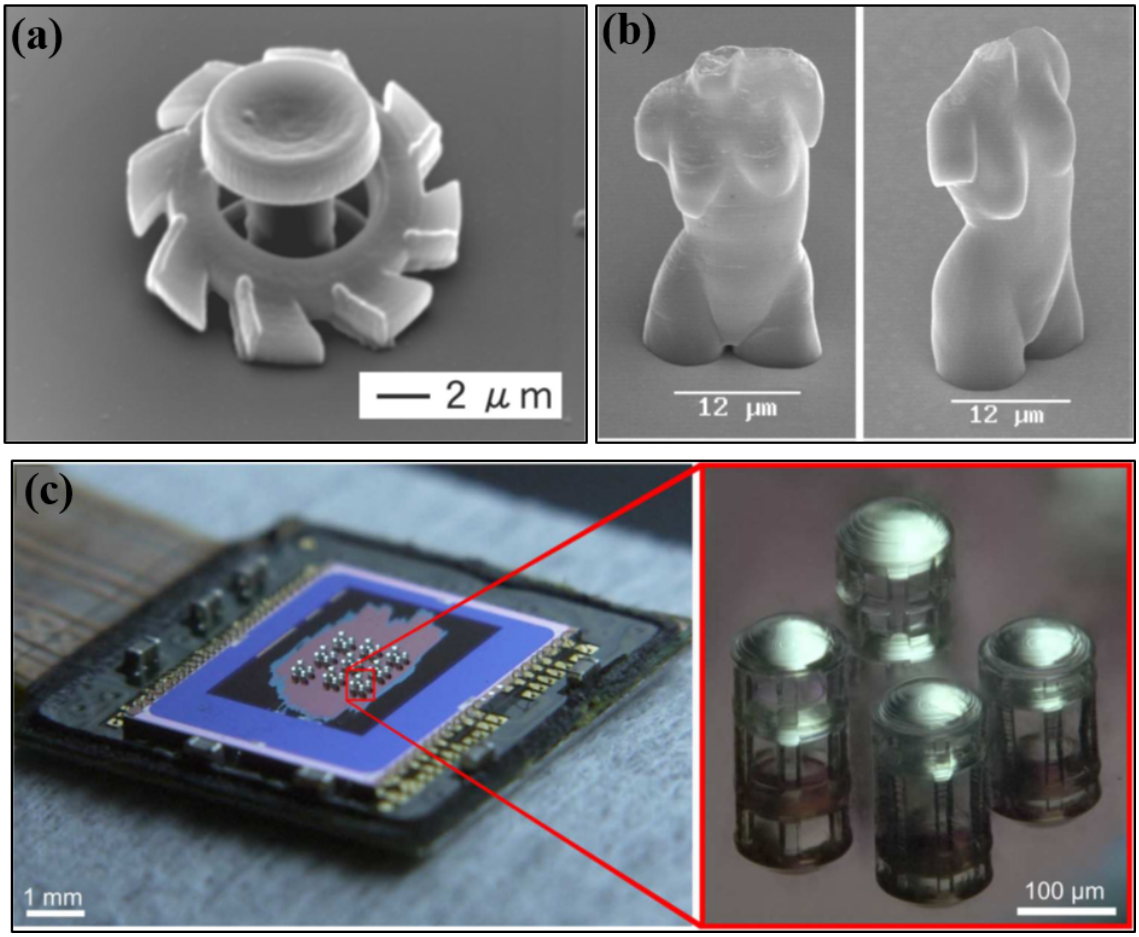

Figure 7: Reproduced images of devices utilizing 2PP micro-fabrication.(a) Optically driven micro-gear [3] (b) Statue demonstrating curvature [4] (c) Compound micro-lens integrated with a CMOS optical sensor [5]

.

a fiber can be precisely cleaved to provide a flat substrate, and the standard fiber dimensions encourage device geometry that is fabricated in a matter of minutes. A range of optical and mechanical devices have been fabricated onto optical fibers, showcasing their natural synergy with 2PP micro-fabrication.

The immediate access to the guided light output by an optical fiber makes fabricating optical elements a natural choice. Anti-reflective metamaterials can be integrated directly onto an optical fiber as shown by [78] and [79]. Lenses are also a promising component, with successful demonstrations of imaging multi-lens objectives [80],

increased numerical aperture lenses [81], and collimators [82]. Other devices include WGM resonators [83, 7], photonic crystal strutures [9, 80], a polarization controller [84], Mach-Zehnder Interferometers [21, 22], optical tweezers [85], and Bragg gratings [86]. Some devices take great advantage of the 3D freedom afforded by 2PP micro-fabrication to build impressive mechanically enabled structures. Examples include a force-sensitive microgripper [8], and a miniature microphone [64]. This work strives to similarly leverage 2PP micro-fabrication to mechanically enable sensors.

The FP resonator, of particular importance to this work, is another popular optical device for 2PP micro-fabrication onto fiber tips. It provides all the benefits as a resonator discussed in subsection 2.1.1, conveniently located on top of a highly versatile light source. A FP cavity can be polymerized with liquid resin still inside of the cavity [60], but the resin will slowly polymerize if exposed to ultraviolet light, and the cavity is closed off to the environment. Several open resonators, very comparable to this work, were fabricated onto conventional substrates, then attached to an optical fiber with optical adhesive as shown in [66] and [86]. While an impressive fabrication feat, this additional step and possible misalignment can be avoided by fabricating directly onto the fiber. On-fiber FP resonators comparable to this thesis are presented in [87] and [6]. Images of select on-fiber 2PP micro-fabrication devices are reproduced in figure 8.

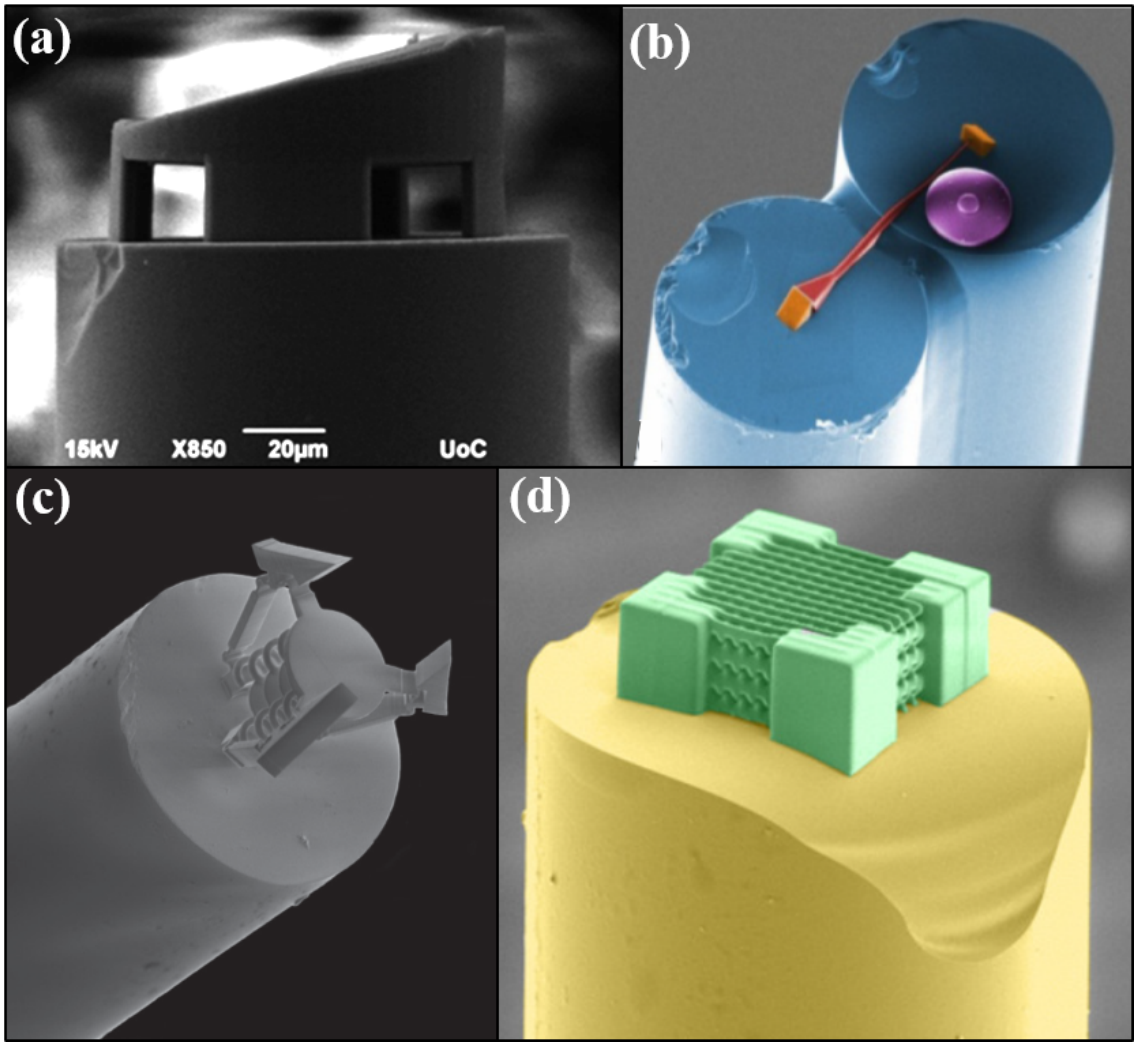

Figure 8: Scanning electron micrographs of several devices fabricated by 2PP onto optical fibers. (a) Open FP Cavity RI Sensor [6]. (b) Whispering gallery mode resonator [7]. (c) Force-sensitive microgripper [8]. (d) Woodpile photonic crystal structure [9].

2.2 Fiber Optic Sensors

2.2.1 Bragg Gratings

Fiber Bragg gratings (FBGs) have been made since the 1990s by creating a pattern of lines with different RI inside the core of an optical fiber. This grating pattern is transparent to most wavelengths, but reflects a certain wavelength whose optical path

interacts with the dimensions of the grating to interfere coherently, much as in a FP cavity. This wavelength is determined by Bragg's law [88]:

$$\lambda_B = 2n_{eff}\Lambda \tag{12}$$

where n_{eff} is the grating's effective RI, and Λ is the spacing between grating elements. This wavelength will shift when the fiber housing is exposed to various stimuli, most notably strain and temperature. A variable wavelength laser source is coupled to a fiber containing a grating through an optical circulator, a device discussed later in section 3.2. The grating reflects one wavelength based on its strain and temperature, and changes in these factors change the wavelength that is reflected. This resonant wavelength is monitored to determine a change in the sensed parameter. Considerable work has been done to characterize and improve these sensors.

Being contained within their optical fiber, FBGs are particularly robust without

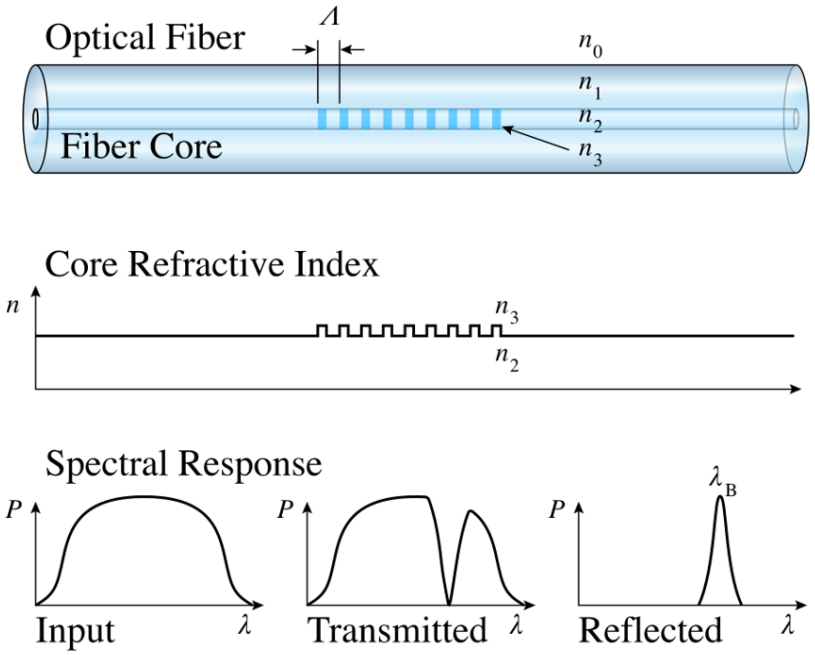

Figure 9: fiber Bragg grating (FBG) and Transmission Spectrum [10].

requiring additional packaging. This, in addition to the EM immunity experienced by all fibers, allows them to be used in hostile environments where other sensors may not survive or function properly. The additional protection limits direct interaction with the environment, limiting the parameters that can be sensed by FBGs. Creative engineering has been able to transduce some external factors into temperature or strain, such as the coating used by [88] to introduce strain when exposed to hydrogen, but such solutions are rare. Further reading on FBGs sensors can be found in [89, 88, 54, 15, 90]. While important devices, this work utilizes FP cavity and simple reflectors for sensing as opposed to FBGs.

2.2.2 Spliced Fibers

One method for creating a microscale FP cavity on an optical fiber is to splice together different fibers. Precise and repeatable fiber splicing is achieved by first cleaving the end face of each fiber, carefully aligning these faces, and effectively arc-welding them together. Researchers have built FP cavities by splicing a traditional fiber to a hollow core fiber (HCF) with some kind of membrane or cap on the end. This technique has been demonstrated as an airflow sensor, capped with another length of SMF [91]. Sensors have also been made that can interact with the environment such as a moisture-sensitive cap of chitosan used as a humidity sensor [92]. Spliced fibers coated with sensitive materials have also measured volatile organic compounds in polluted soil [93]. A sensor has even been reported utilizing three types of fiber spliced together. A SMF is spliced to a HCF which acts as the cavity body and is spliced to a perforated photonic crystal fiber (PCF). The small waveguide holes of air in the PCF allow gas to enter the cavity, changing its RI and reflection response [13]. Another creative use of fiber splices used an intentional defect on the surface of the fiber caused by a femtosecond laser to create a bubble during the splice [11]. This

also created a curved mirror surface in the FP cavity, gaining the benefits discussed in subsection 2.1.1. This device was able to sense RI and temperature change. Another technique involved splicing off the end of an attached HCF to create a closed bubble of air inside the glass [12]. Examples of spliced fiber sensors are included in figure 10.

The main problem with splicing multiple types of fibers is repeatability. The process often involves time-consuming setups, and the splice may be different every time. Thisleads to changes in device geometry and/or cause failures. The 2PP micro-fabrication used in this research is highly repeatable and allows for arbitrary geometries not limited by the functional dimensions of fiber splices.

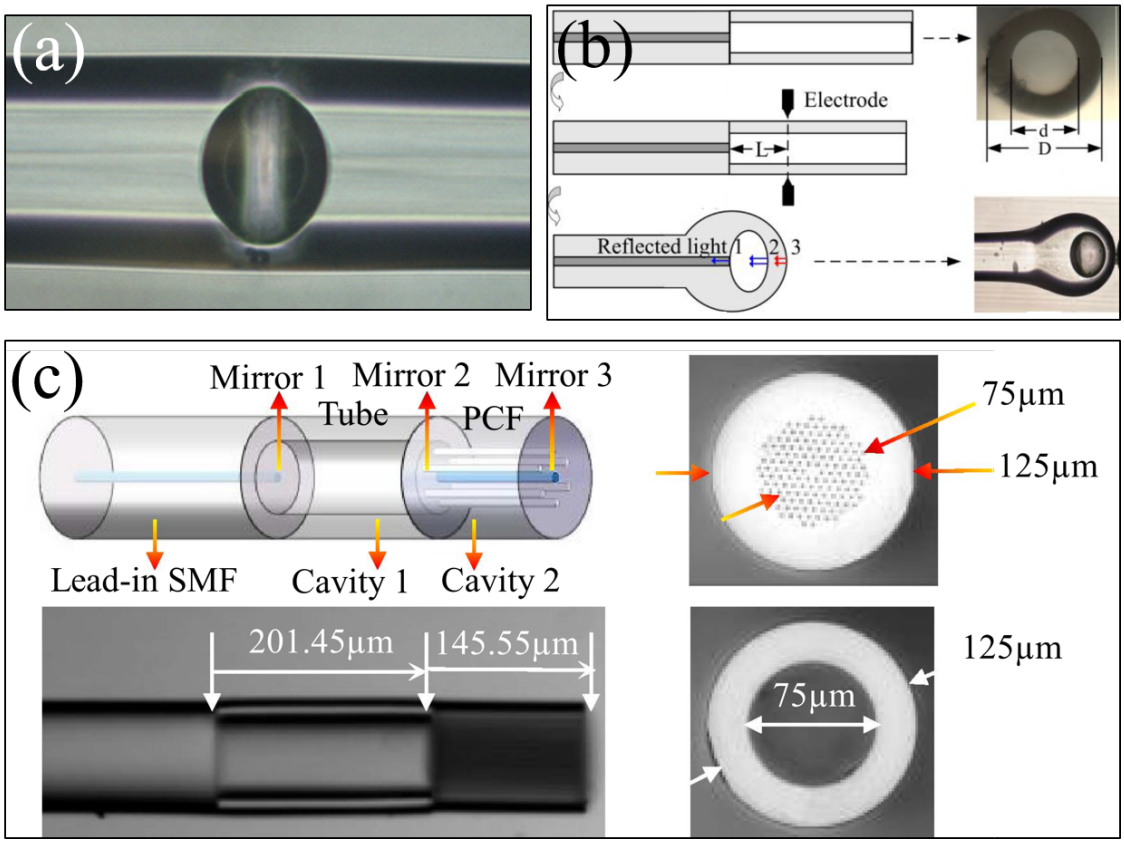

Figure 10: Examples of Spliced Fiber Sensors. (a) Glass bubble by splicing around a defect caused by a femtosecond laser [11] (b) Glass bubble by splicing the end of a HCF [12] (c) RI sensor with three different fiber types spliced together [13]

.

2.2.3 Subtractive Manufacturing

Another promising method for fabricating fiber tip sensors is subtractive manufacturing by removing portions of the fiber. This technique enables high precision FP cavities that are open to the environment. It is possible to simply remove part of the fiber with a femtosecond laser, and create an opening to serve as a cavity and sense temperature [16, 57] as well as RI changes of an interstitial medium [94]. A similar technique uses a focussed ion beam (FIB) to remove material. Cavities formed by a FIB have been demonstrated on a 10-μm tapered fiber [58, 15], and combined with a bi-metalic coating [55] to produce temperatures sensors. A more complicated fabrication scheme used hydroflouric acid (HF) to selectively etch the cores of two different fibers to achieve smaller cavities in a dual temperature and pressure sensor [56]. A very promising method uses a femtosecond laser to degrade part of the fiber, which is then etched away with HF [14]. The degraded portion of the laser beam can be scanned through the fiber at any height to achieve 3D freedom. The size of features made with this process is still limited, as the HF etches selectively, not exclusively. Precise timing and careful planning is necessary to account for the etching into the unexposed features. The surface finish of the etch is also rather poor. Lack of precise control is the main constraint on subtractive manufacturing. Glass also presents some problematic material properties, being brittle and rigid compared to most 2PP photoactive resins. Images of sensors made with subtractive manufacturing are included in figure 11.

2.2.4 Additive Manufacturing

The final fabrication technique to be discussed is additive manufacturing. The 2PP micro-fabrication used in this work is additive manufacturing in the purest sense, but other notable techniques have been demonstrated. The simplest method care-

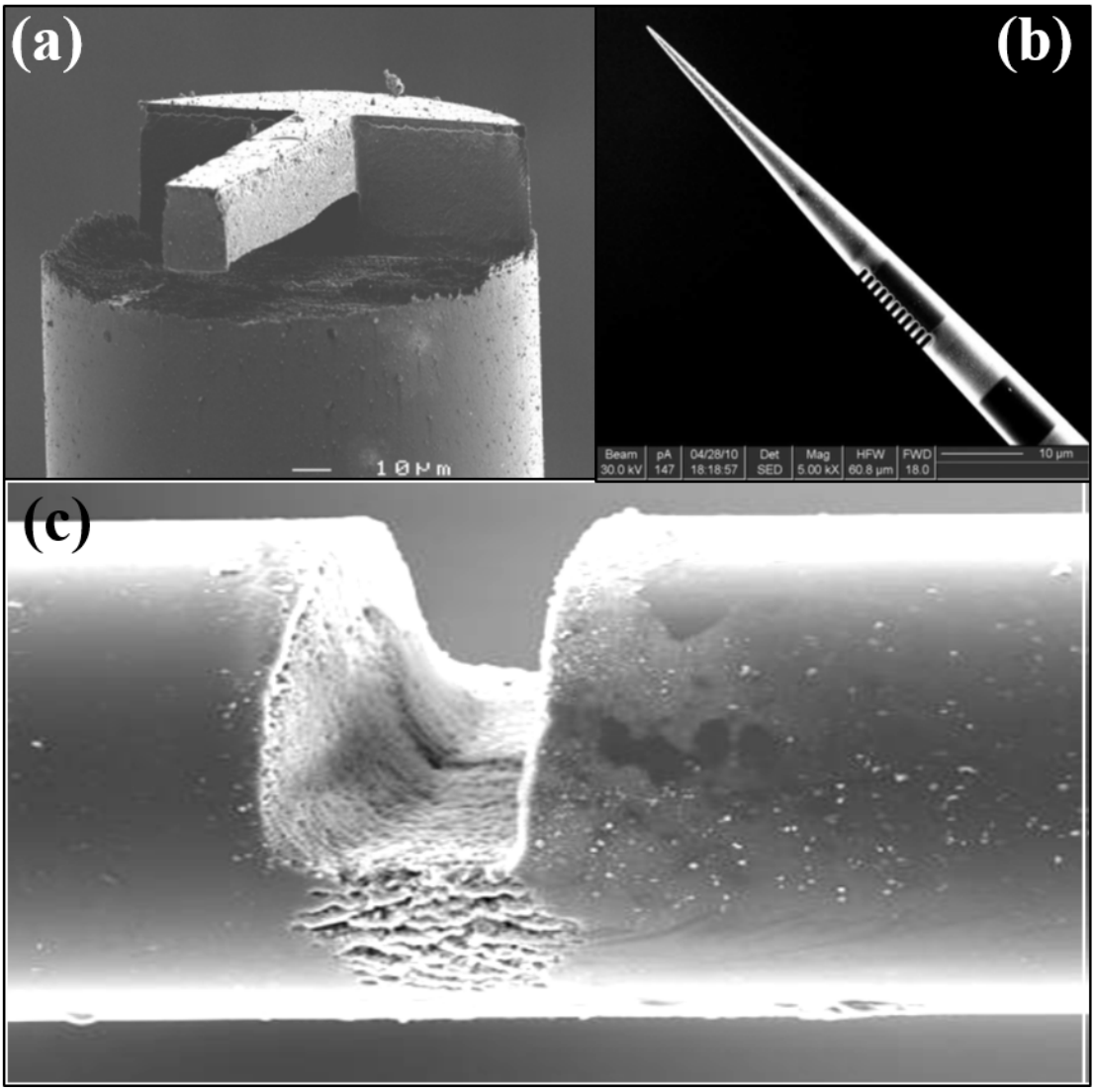

Figure 11: Devices made with subtractive manufacturing. (a) Femtosecond laser and HF to create a free cantilever [14]. (b) Bragg grating on a tapered fiber made with FIB milling [15]. (c) A groove FP cavity made with femtosecond laser micromachining [16].

fully places a droplet of UV-curable optical adhesive onto a cleaved fiber to create a dual temperature and pressure sensing FP cavity [59]. While very limited in possible geometries, this work establishes a precedent for the precise application of optical adhesive, which is used in this research and discussed in subsection 4.2.3. Other demonstrations of optical adhesive use another fiber to mold an adhesive cavity [19],

glue a capillary tube around a cleaved fiber to build a pressure sensor [18], create a domed cover to a spliced HCF for another pressures sensor [17], and adhere a fiber to a silicon-based photonic crystal mirror to make an acoustic sensor [95]. Incorporating silicon chips is particularly interesting for integrating with CMOS technology and leveraging standard semiconductor fabrication processes. Specifically, deposition techniques such as magnetron plasma sputtering [19, 18, 96], thermal evaporation [20], e-beam evaporation [95], chemical vapor deposition (CVD), and atomic layer deposition (ALD) can deposit reflective materials to increase the quality of an FP cavity's response as discussed in subsection 2.1.1. The popularity of sputtering is likely due to its conformal coverage, rapid deposition, and relative ease of operation. Sputtering was also used in this work, with specific settings included for each device in their respective fabrication sections. Several adhesive-based devices are pictured in figure 12

Adhesive-based sensors are primarily limited in their geometry. The glue is either molded, or another part is attached, both of which constrain the shape of any device. True 3D freedom is achieved by using some form of sterolithography to solidify a photoactive polymer resin layer-by-layer. One group was able to create a custom system that sprays a layer of photoresist, selectively exposes the layer, and repeats the process to construct impressive 3D features [61]. The process is rather time consuming, and limits on the x, y, and z resolution are set by the quality of the exposure and layer deposition. The purpose-built solution is a 2PP micro-fabrication system as described in subsection 3.2.3. An innovative method for integrating 2PP micro-fabrication with optical fibers is to create a device on a planar substrate and adhere it to a fiber as a seperate step [66, 22]. This allows the 2PP system to be used without modification, but adds considerable complexity to the fabrication and limits the possible features at the face of the fiber. With some minor modifications,

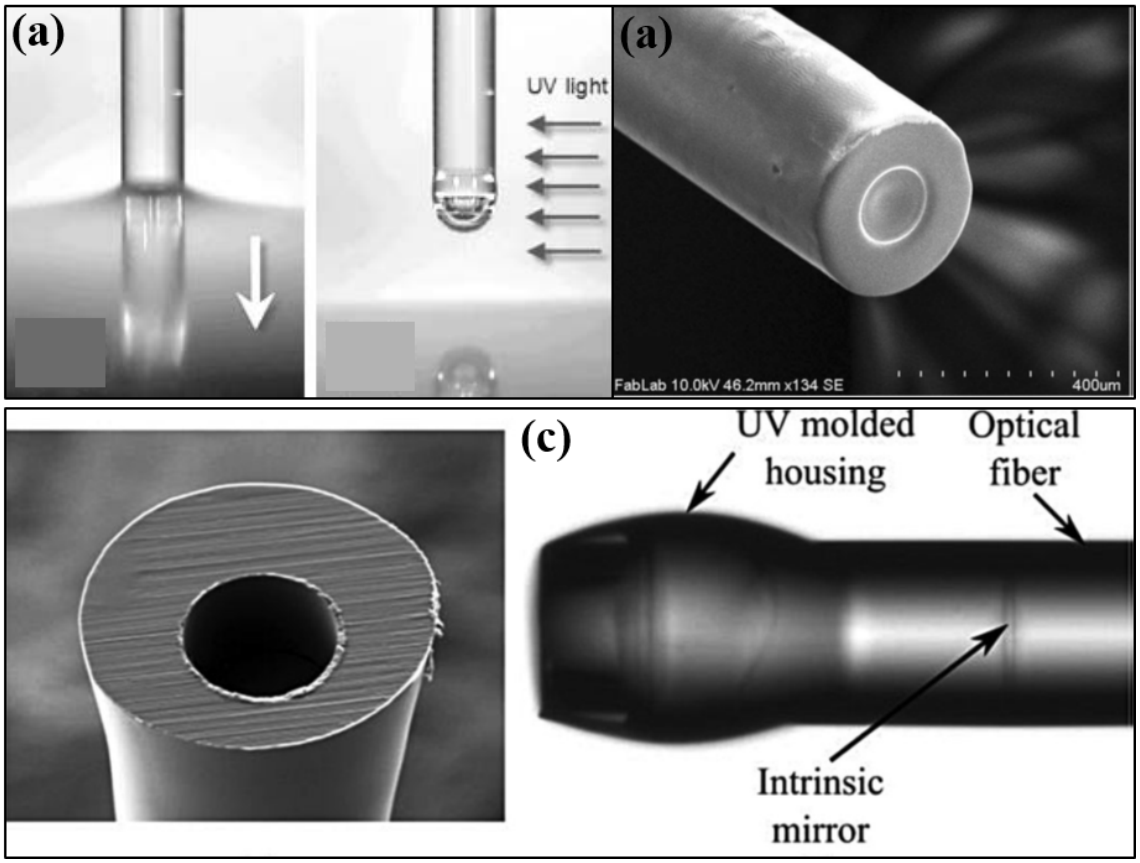

Figure 12: Adhesive-based fiber tip sensors. (a) A polymer droplet cap to a spliced fiber [17]. (b) A capillary tube adhered around an optical fiber [18]. (c) An adhesive molded cavity [19].

it is possible to perform 2PP micro-fabrication directly onto the cleaved face of an optical fiber [27]. Fiber tip sensors utilizing this technique include an open FP cavity RI sensor [6], a "radar-like surface enhanced Raman scattering sensor" [20], a WGM resonators for vapor interrogation [83] and temperature sensing [7], a Mach-Zehnder interferometer RI sensor [21], a fluid filled cavity temperature sensor [60], and a micro-scale microphone with spring bodies [64]. Several of these devices are pictured in figure 13. This research aims to expand on this work to take full advantage of the 3D freedom afforded by 2PP micro-fabrication to enable low-SWAP fiber optic sensors.

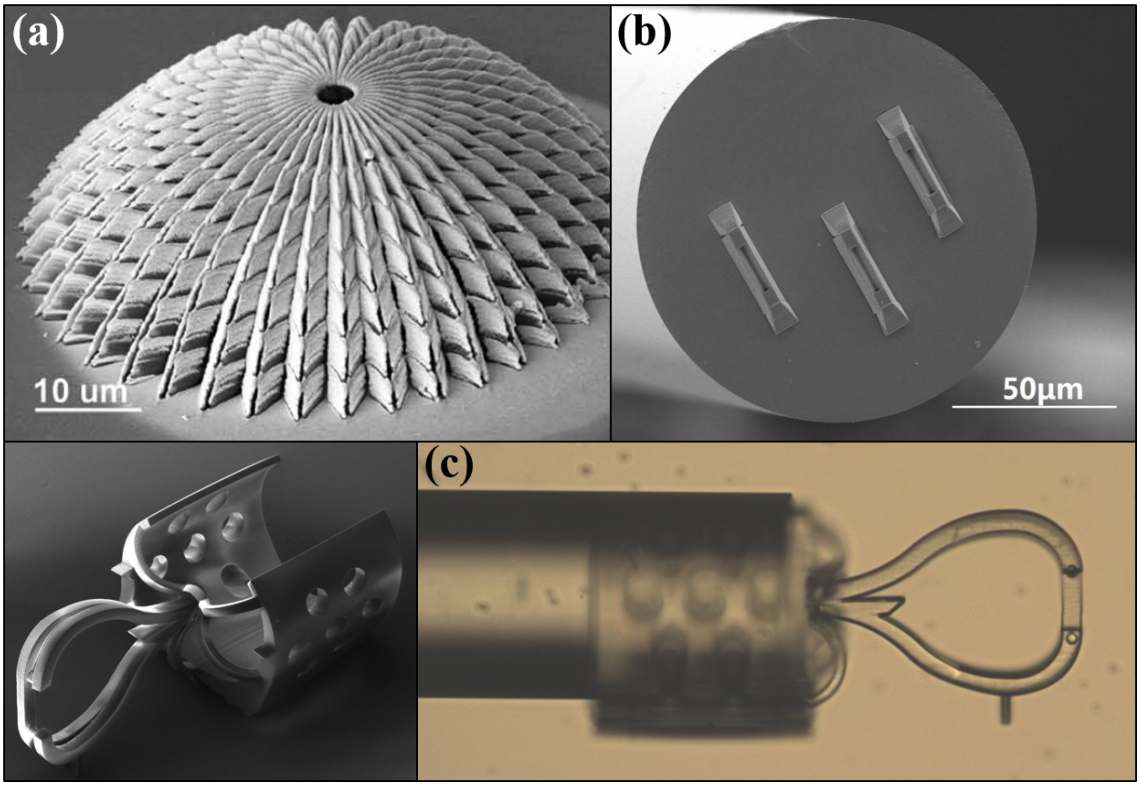

Figure 13: Fiber tip sensors made with 2PP micro-fabrication. (a) Surface Enhanced Raman scattering sensor [20]. (b) Mach-Zehnder interferometer RI sensor [21]. (c) A Mach-Zehnder interferometer fabricated on a planar substrate and adhered to a fiber [22].

2.2.5 Fiber Optic Flow Sensors

Several different flow sensors have been demonstrated on or using optical fibers. One popular method is to heat a FP cavity, immerse it in a flowing media, and monitor the shift in resonant wavelength caused by the subsequent cooling. This has been done with a polymer cap of optical adhesive fixed to a resistance heater, [97], silicon cylinders adhered to an array of fibers in a multi-bore micro tube and heated with a laser [25, 98], and fiber Bragg grating mirrors placed inside [99] and alongside [100] flow channels. This is an effective method, but requires a source of heat, either from a resistance heater or by a powerful laser down the fiber which would add to the bulk of any final product. They are also sensitive to changes in flow temperature,

which would need to be calibrated and held constant to make reliable readings.

Another fiber based flow sensor simply monitors the deflection caused on a FP cavity by incident flow [101, 102]. These sensors will also be vulnerable to the effects of thermal expansion and the thermo-optic effect that will change their cavity length and interstitial medium RI respectively. The flow must also be powerful enough to cause a noticeable deflection, limiting the device's operating regime. Two such sensors can be integrated to compensate for temperature changes as shown in [102], but this increases the size and complexity of the device.

A very simple sensing mechanism is to place a fiber in a flow stream and monitor the bending loss as the flow around the fiber increases [103]. This type of device has a limited operating range defined by the maximum bending of the fiber, and occupied a large volume of the flow channel. A similar deflection-response device utilized an artificial hair consisting of a fiber coated in carbon nanotubes (CNTs) placed into a flow field [26]. The deflection of the fiber pressed the CNTs into electrodes to produce an electrical signal. This device must be extended relatively far into the flow field, and is again limited to measuring strong flows able to produce a deflection, but not too strong to reach maximum deflection. It also requires electrical routing to communicate with the electrodes and several precise fabrication steps. Another creative technique has been demonstrated to monitor the vibration of a fiber caused by flow [24]. This method would struggle to monitor flow from different directions, and must be monitored by a charge coupled device (CCD) placed near the fiber. This greatly increased the footprint of the device. One very promising device introduced a dual FP cavity miniature pitot-tube into a fiber optic [23]. This device showed a good operating range and resolution, but required complicated fabrication consisting of two fiber splices, HF etching, and femtosecond (fs) laser machining. Some examples of these alternate fiber flow sensors are included in figure 14. The flow sensor presented

in this work features safe, a simple fabrication which is safe and offers low-power optical operation, and an advanced geometry with range-scaling potential.

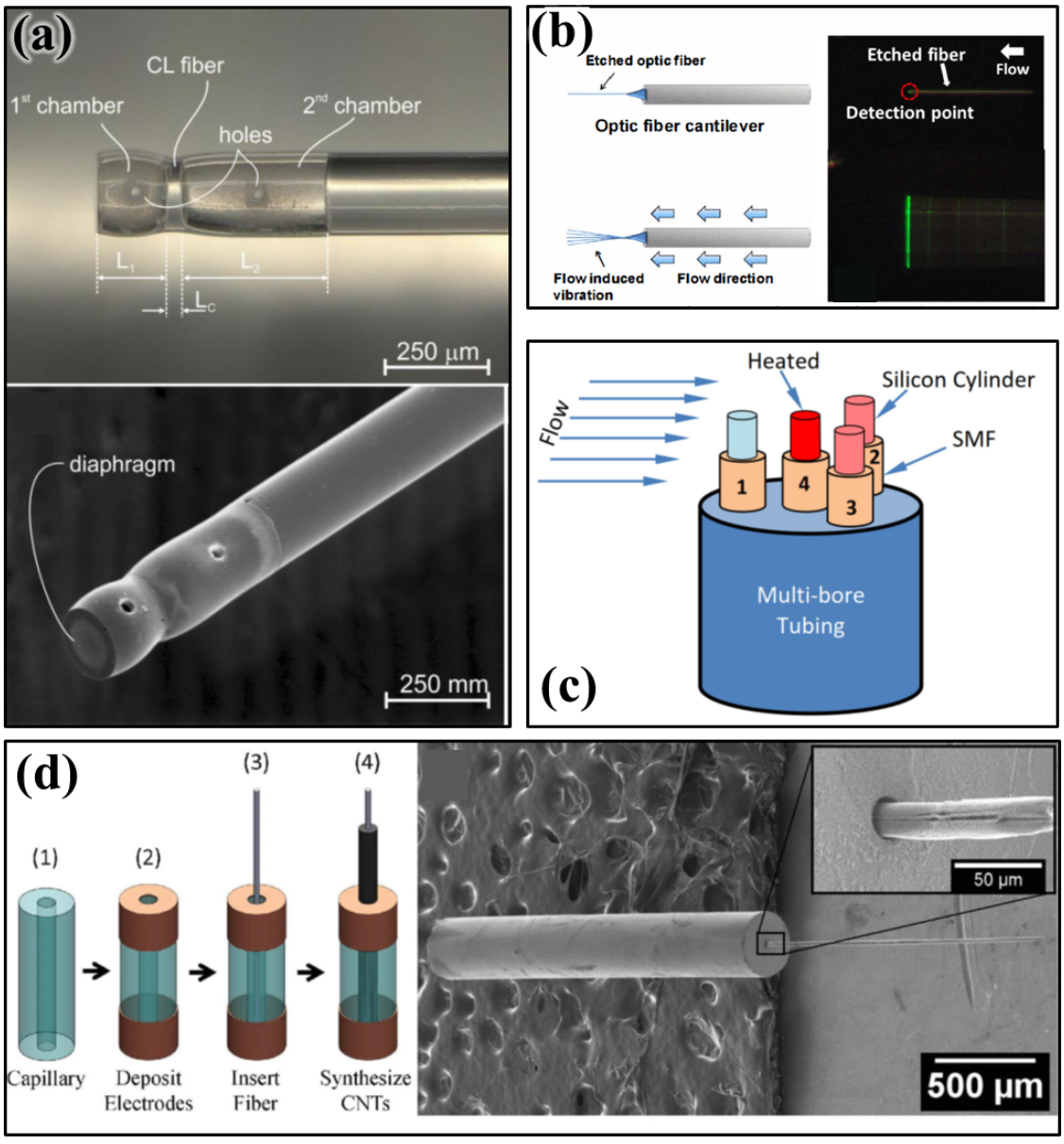

Figure 14: Reproduced images of several optical fiber flow sensors. (a) Miniature pitot tube [23]. (b) Flow-induced vibration monitor [24]. (c) Laser-heated FP Cavity array [25]. (d) Artificial hair CNT coated fiber [26].

III. Mechanically Enabled Fabry–Pérot Cavity Refractive Index Sensor

3.1 Chapter Overview

This first device we studied was a mechanically enabled Fabry–Pérot (FP) cavity refractive index (RI) sensor constructed by two-photon polymerization (2PP) microfabrication on the tip of a low-loss single mode fiber (SMF). The device features a mechanically enabled mirror that can be maneuvered into several positions: half-open, fully open, and closed. An SEM image of the device showing two of the mirror's positions is included in figure 15. The device is fabricated in the half-open position, which requires minimum support material. The fully open position enables the precise application of reflective coatings with common semiconductor fabrication techniques such as plasma sputtering onto features that would otherwise be covered. A locking mechanism holds the arm in the closed position to maintain alignment in both vapor and liquid environments. The reflection spectrum of the device aligns well with the response predicted by FP resonator theory, and changes in response to the interstitial medium of the open cavity. This enables the device to sense liquid composition, gas composition, temperature, and pressure. Integration with SMF enables remote sensing potentially over several kilometers, allowing the analytical equipment and optical sources to be conveniently located away from the sensor. The hinge and locking features highlight the potential of 2PP microfabrication, and represent an enabling technology for future devices.

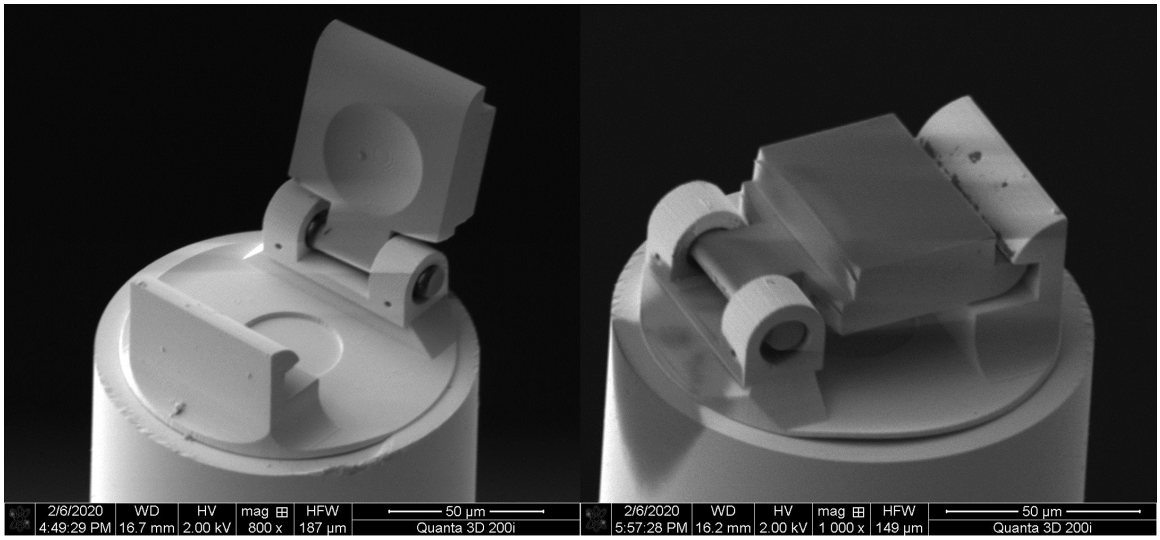

Figure 15: SEM image of the mechanically enabled FP cavity RI sensor. (a) The half-open position it is fabricated in. This image was taken after metal deposition so the hinge is slightly ajar. (b) The closed, operational position. The shadow caused by the open device during metal deposition can be seen underneath the pin housing.

3.2 Methodology

3.2.1 Operating Principle

The reflection response of a FP cavity, as discussed in 2.1.1, is determined by the physical properties of the cavity and the wavelength of the incident light. An important and easily measured metric is a cavity's free spectral range (FSR), which is the wavelength shift between two resonance features. Figure 3 contained an example reflection spectrum, and figure 16 shows the FP resonator interaction occurring inside the device. The FSR of a cavity is [33],

$$\Delta\lambda_{FSR} = \frac{\lambda_0^2}{2nl} \tag{13}$$

where λ_0 is the central resonant wavelength, n is the RI of the medium inside the cavity, and l is the length of the cavity. While changes in the FSR are informative, they must be measured over a large bandwidth, containing as many peaks as possible

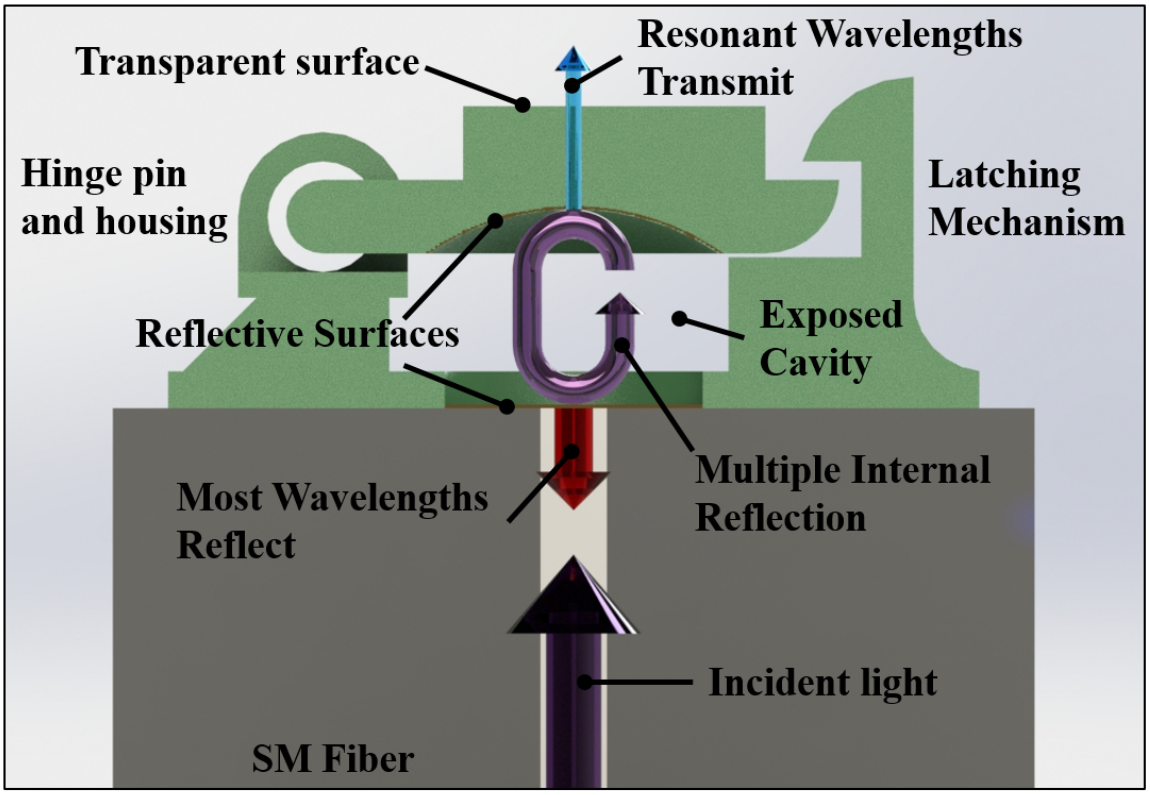

Figure 16: The optical response of the mechanically enabled FP cavity sensor.

to be accurate. Smaller changes in cavity length and RI can be determined by taking the derivative of equation 3,

$$\lambda_0 = \frac{2nl}{m} \tag{14}$$

$$d\lambda_0 = \frac{2n}{m}dl + \frac{2l}{m}dn, \tag{15}$$

rearranging equation 14 to produce $m = \frac{2nl}{\lambda_0}$ and substituting this into equation 15,

$$d\lambda_0 = \frac{\lambda_0}{l}dl + \frac{\lambda_0}{n}dn. \tag{16}$$

Collecting terms and assuming the linear approximation $dx \approx \Delta x$ yields,

$$\frac{\Delta\lambda_0}{\lambda_0} \approx \frac{\Delta l}{l} + \frac{\Delta n}{n}, \tag{17}$$

thus if the other is assumed to be constant, any environmental factor that changes in cavity length and RI can be extracted from changes in the resonant wavelength. This device focused on measuring changes in RI, and the phenomenon that cause them, and was fabricated with two open sides so the cavity could interact with the environment. Liquids or gasses with various compositions and known RIs could be identified by cross-referencing with accepted data.

It is also known that the RI of air is dependent on both its temperature and pressure. Assuming the other properties of the air are constant, changes and temperature or pressure can be extracted from changes in RI. The National Institute of Standards and Technology (NIST) provides a program to estimate the RI of air based on pressure, temperature, wavelength, and relative humidity based on the modified Edlén equation in their metrology database [28]. This was the source of the RI values compared with the measured results in section 3.3.

If the device is used to sense temperature, the FSR of the device will also change as the cavity length changes due to thermal expansion of the polymer. This expansion is based on the material's coefficient of thermal expansion α, the original length l_0, and the change in temperature ΔT. Since the device contains two mechanically decoupled features, the mirror and the base, there are two competing expansion events to consider: the base expanding upward to reduce the cavity length, and the mirror expanding outward to reduce the cavity length. The total change in length can be expressed as:

$$\Delta l_{total} = \Delta l_{base} - \Delta l_{mirror} = (l_{0base} - l_{0mirror})\alpha\Delta T. \tag{18}$$

Thus, temperature can be determined if pressure and cavity geometry are known, and pressure can be determined if temperature is known.

3.2.2 Device Design

The mechanically enabled FP cavity was designed to enable metal deposition onto three faces of a dual-cavity device like those created by Air Force Institute of Technology (AFIT)'s Capt John Smith [27]. A dual FP cavity sensor could simultaneously measure temperature and other RI changes by referencing a polymer cavity that only experiences thermal expansion. Most reflective-coating deposition systems, including sputtering and evaporation, have directional deposition. This made it difficult to deposit evenly on all three surfaces due to shading from the other features. A reflective coating was highly desired to improve the quality of the reflection response as described in subsection 2.1.1.

Initiially, atomic layer deposition (ALD) was considered initially because the self-limiting reactions are fully conformal to any geometry. Despite this impressive advantage, ALD is a very time consuming and offers a limited selection of materials. A more accessible deposition method was desired. An initial study was performed evaluating plasma sputtering and plasma-enhanced chemical vapor deposition (PECVD). Glass slides (76mm x 24mm x 1mm) were coated on each side with four metals and five dielectrics of various thicknesses as described in table 1.

Table 1: Reflective coating evaluation on 76mm x 24mm x 1mm glass slides

Material	**Deposition Method**	**Thickness Series**
Aluminum Oxide	plasma Sputtering	50 nm, 100 nm, 150 nm
Zinc Oxide	plasma Sputtering	50 nm, 100 nm, 150 nm
Silicon Nitride	PECVD	50 nm, 100 nm, 150 nm
Gold	plasma Sputtering	20 nm, 40 nm, 80 nm
Aluminum	plasma Sputtering	20 nm, 40 nm, 80 nm
Platinum	plasma Sputtering	20 nm, 40 nm, 80 nm

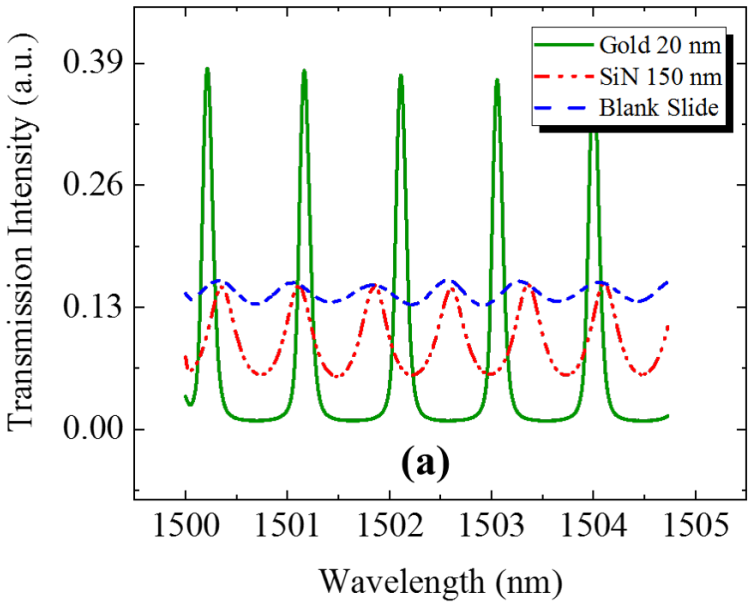

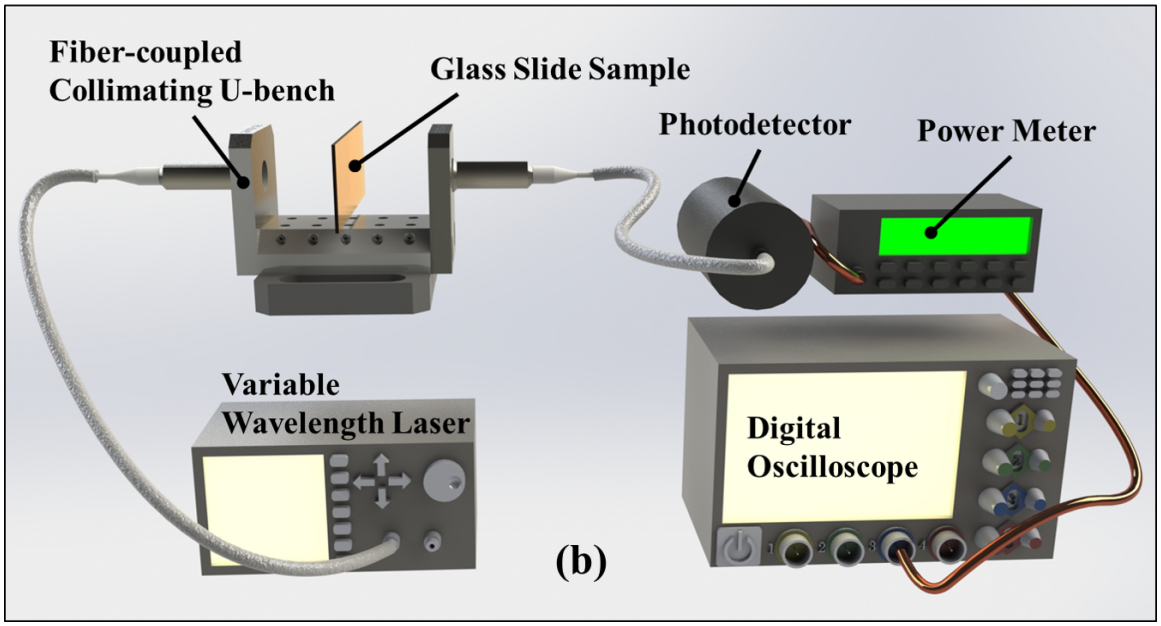

Figure 17: Reflective coating study. (a) Selected reflection responses. (b) Experimental setup.

Gold provided the highest quality factor during this study. It was also easily available in the AFIT cleanroom and could be deposited quickly with plasma sputtering, so gold was used as the reflective coating for the rest of this research. The transmission responses of several reflective coatings from this experiment are included

in figuer 17 (a). The measurement setup used is described in subsection 3.2.4, and a graphic is included in figure 17 (b). To confirm an improvement in the reflection response, a reflective gold coating was deposited onto one of Capt Smith's flat mirror devices as described in [27]. The results were very promising, significantly improving the quality factor of the resonance. This is pictured in figure 18.

Successful deposition parameters proved challenging to determine. The 20-nm deposition that was successful on glass slides was too thick for the fiber-tip devices. All resonance features were washed out by a constant reflection. The deposition rate was also highly dependent on the orientation and location of the device inside the sputtering process chamber. The most successful positioning for the flat mirror device was centered in the chamber, lying on its side with all three faces perpendicular to the sputtering target. The most successful power and time was 100 W for 120 sec.

While the reflective coating appeared to function as intended, the measured FSR corresponds to only one cavity between the top of the polymer and the fiber face. This eliminates the self-referencing ability of the sensor as there is no reflection feature

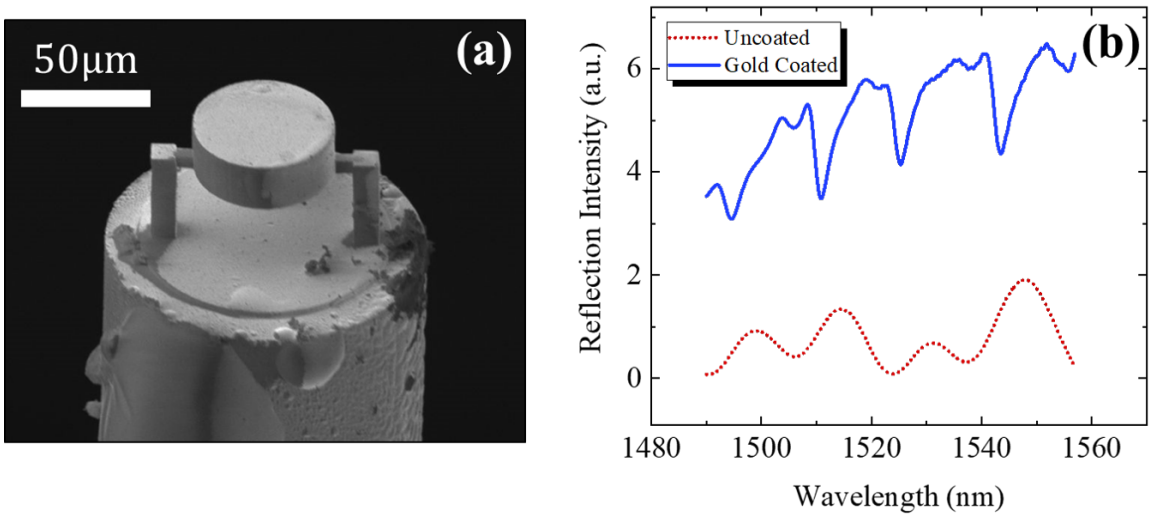

Figure 18: Flat mirror FP cavity device improved with a gold reflective coating. (a) SEM image of the device taken by Capt Smith [27] (b) Original and improved reflection response.

that changes only with temperature. The hinge, as seen in figures 15 and 16, was introduced to enable more consistent deposition accessible to all three mirrors.

There were also difficulties sputtering onto confocal devices. The benefits of a confocal FP cavity include improved alignment insensitivity and lateral confinement. Capt Smith successfully demonstrated a confocal device made by 2PP microfabrication in his thesis research [27], but it was difficult to add a reflective coating to this design. Various confocal geometries were attempted, with only one success in a large, 60-μm cavity. The other designs performed significantly worse after gold deposition, most likely because the fiber face received gold while the inner face was shaded by the curve of the mirror. The successful confocal device is pictured in figure 19. The confocal device successfully measured the RI of air and of liquid IPA, as observed by a change in FSR. The reflection response, and FSR between subsequent peaks is plotted in figure 20. The method for extracting resonant peak locations and the measurement uncertainty plotted as error bars is described later in subsection 3.2.4, and was used for this devices as well. The theoretical FSR was calculated using the measured locations of each pair of resonant peaks and an RI of 1.0003 for air and 1.3776 for IPA with equation 13.

The small FSR of the 60-μm cavity makes it difficult to distinguish changes in resonant wavelength. It also limits the detectable range of RI to one FSR if not measuring a lengthy spectrum with many resonant wavelengths. The hinge enabled equal deposition, ignoring shading based on curved features. Smaller cavities were also possible with the hinged device since shading within the cavity was not present during deposition. A smaller cavity was less sensitive to misalignment, provided a larger FSR, and experienced less thermal expansion.

The mechanically enabled FP cavity underwent several design iterations, some of which are included in figure 21. The 2PP microfabrication technique allowed

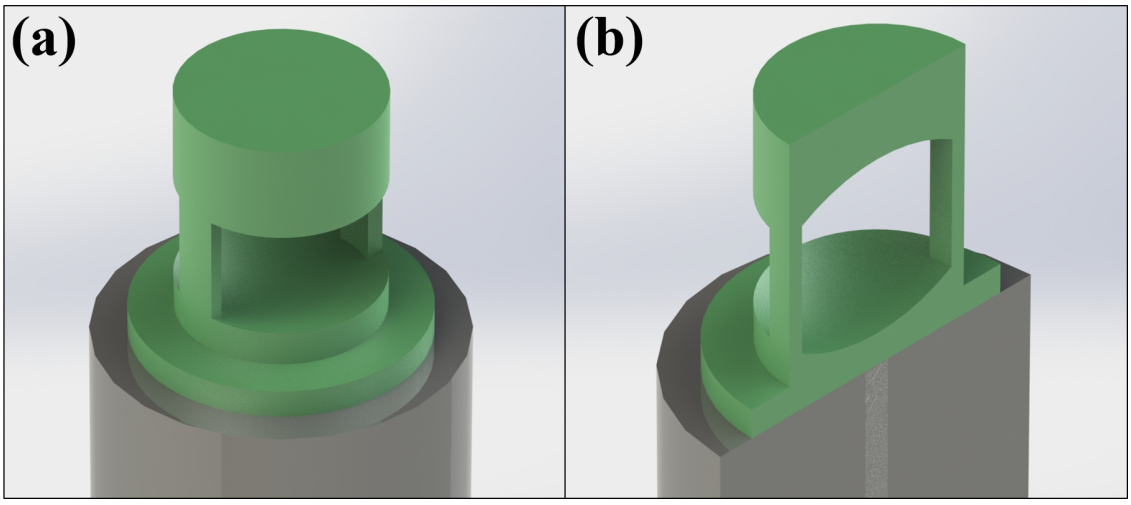

Figure 19: The successful confocal design with a 60-μm cavity length. (a) Isometric render. (b) Section view.

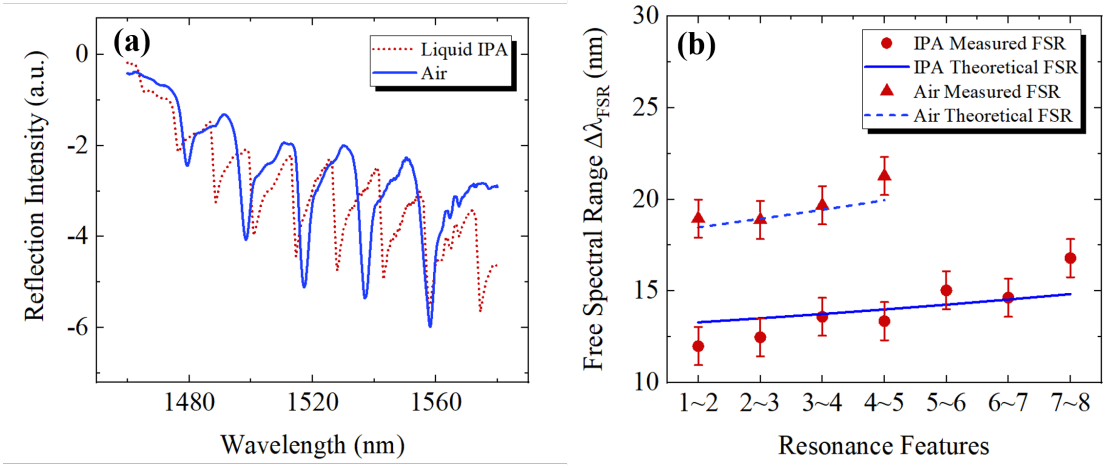

Figure 20: Measurement results of the confocal device. (a) Reflection spectrum in air and IPA. (b) Theoretical and measured FSR of the peak wavelengths. Error bars represent the uncertainty of the measurements, discussed later in subsection 3.2.4

for an iterative design process that would be very difficult to achieve with planar semiconductor fabrication. Each design was reproduced only a handful of times, and each iteration offered valuable design lessons that could be immediately implemented. Early devices struggled greatly from misalignment. As a result, a free hinge, depicted in figure 21 (b), was built to explore different alignment angles. This device also

performed poorly, indicating some kind of latch was necessary to control the variation allowed by the hinge pin clearance.

The latching feature was also extended over the entire depth of the rotating face, and a shelf was added to further align the mirror once closed. A curved mirror was added and the cavity length was reduced to 22μm to further improve misalignment sensitivity and lateral confinement. The pin was connected to the housing during fabrication by a thin, breakable support. The most successful support design was a series of five 1-μm diameter columns. The pin was 10μm in diameter, and had a 2.5-μm clearance from the housing. Holes were included in the housing to allow developer to penetrate between the tight clearances when washing away undeveloped resin as discussed in subsection 3.2.3. The clearance between the pin and its housing caused some variability since the device moved when placed in liquids or after experiencing a shock. The shorter 22-μm cavity length greatly reduced this problem since, geometrically, light has less opportunity to walk-off from a slightly misaligned top mirror in a short cavity. All of these physical features contributed to the most stable hinged FP cavity produced in this research. A graphic depicting the primary features of the final device is included in figure 22.

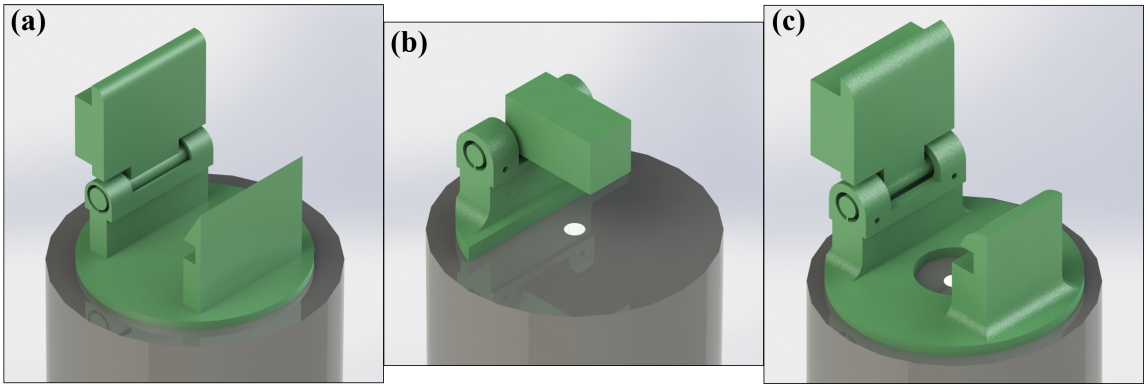

Figure 21: Earlier designs of the mechanically enabled FP cavity sensor. (a) Initial concept. (b) A non-latching, free hinge to explore alignment sensitivity. (c) The most successful flat cavity device.

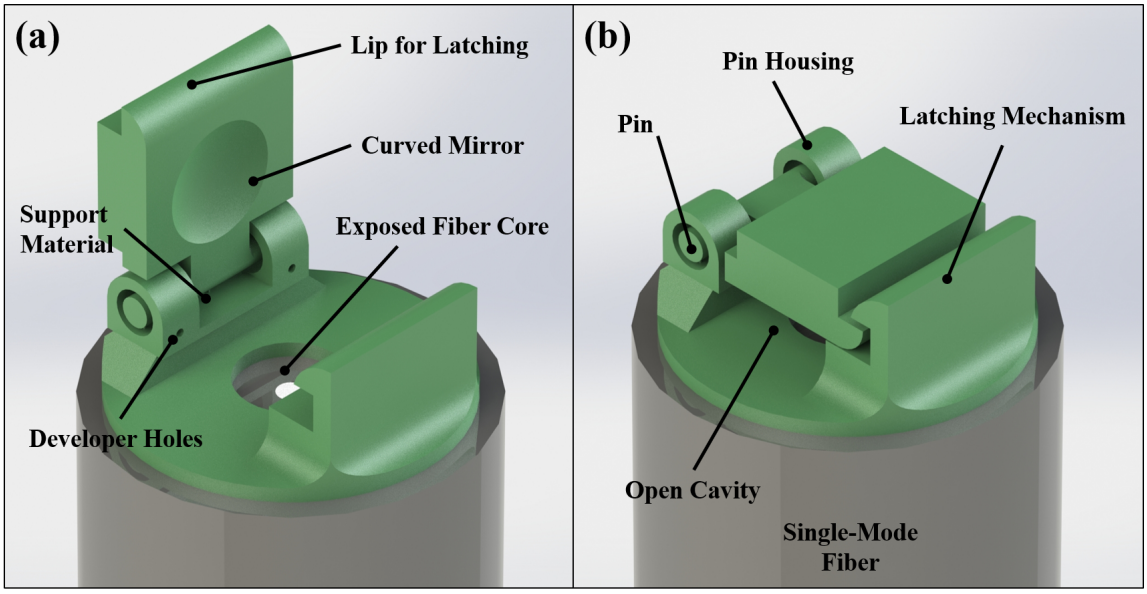

Figure 22: A render of the mechanically enabled FP resonator device with a 22-μm cavity used for testing. (a) The half-open position. (b) The closed, operating position.

Before the shorter cavity was attempted, a very similar hinged device was evaluated with a longer, 33-μm cavity. A graphic depicting this device and its reflection response is included in figure 23. It is important to observe the resonant peak envelope from this device, as these features are more separated in the final, 22-μm device. This envelope occurs because the curved mirror allows multiple resonant modes in addition to the primary logitudinal resonant mode which occur at slightly different but related wavelengths [104]. In a curved-mirror FP resonator, the FSR is measured from one peak to the corresponding peak in the next envelope. The distance between resonant modes within an envelope also related to the length of the cavity, but based on the location of the beam waist [104]. These features are not of particular interest to this work, but are noticeable in the reflection spectrum of the final device. They are not as easily visible in the static confocal device because the 60-μm cavity is so long that they blend in with the primary resonance feature.

New settings were needed to deposit a reflective coating that was not too reflective,

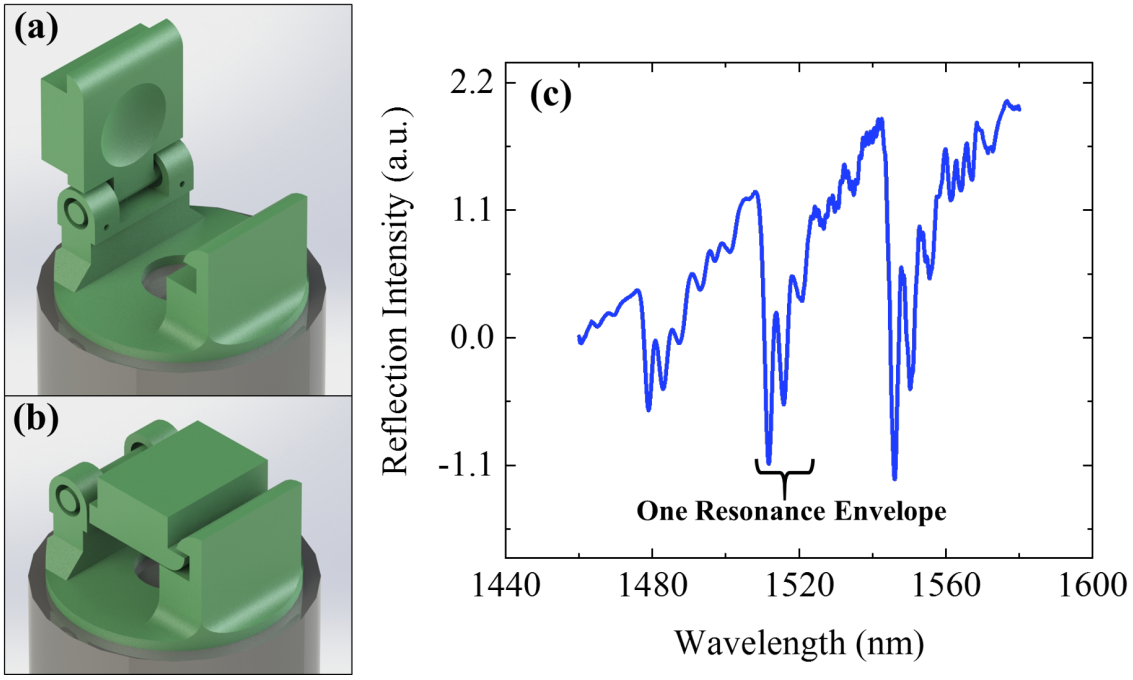

Figure 23: Taller hinged FP resonator device with a 33-μm cavity highlighting the resonance envelope created with a curved mirror. (a) The device as fabricated in the half-open position. (b) The closed device. (c) The reflection response in air with the power floor subtracted out and smoothed in MATLAB®.

but improved the Q-factor. The most successful placement of the device was centered in the process chamber, held vertically so each face is parallel to the sputtering target. The hinge was opened to its fully-open position, shadowing the top of the polymer cavity and encouraging equal deposition on both the fiber face and the bottom of the polymer cavity. A gold coating deposited at 100W for 52sec proved to be the most successful, and the key features of the recipe are included in table 3. The final hinged FP cavity sensor featured easily breakable supports, consistent alignment, and an improved quality factor.

3.2.3 Fabrication

The devices in this work were fabricated by 2PP microfabrication with the Nanoscribe GmbH Photonic Professional GT sterolithography system. First, the optical

fibers were cleaved with a Fujikura CT-30 high-precision fiber cleaver. They were mounted into a Newport FPH-S side-loading fiber chuck with approximately 1 mm extended from the end. This was mounted into a custom 3D-printed jig designed by Capt Smith and detailed in [27]. A drop of the Nanoscribe's IP-Dip photo-resin was then deposited onto the face of the fiber chuck, surrounding the fiber in resin. The jig was fastened to the 2" wafer plate provided with the Nanoscribe. This plate was used because it had three accessible threaded holes for mounting. To access the plate, the top light of the Nanoscribe was unscrewed and set aside. A picture of the Nanoscribe and several steps of this loading procedure is included in figure 24.

The laser aperture, a custom 63x objective lens, was raised manually to the fiber. The fiber was initially located by following the groove of the fiber chuck. Subsequently, the fiber was mounted in nearly the same location, so it could be approached directly based off of its last known location. A laser employing ultra-short pulses scanned through the resin layer-by-layer according to a computer aided design (CAD) file. The laser used a wavelength of 780 nm, a 80-MHz repetition rate, and a 120-femtosecond (fs) pulse duration. The CAD file was first generated in Solidworks, then partitioned into vertical layers by the DeScribe slicer software. Red light from a flashlight was coupled to the fiber to identify the core. A small disk on each device was used as an alignment mark to line up with the core, thus centering the device on the fiber. This was done by focusing the laser inside the fiber where it was still visible, but not polymerizing resin.

To ensure adhesion to the fiber face, each print was started approximately $5\mu m$ beneath the surface of the fiber such that the $5\mu m$ thick base pad would be traced inside the fiber, not the resin. Thus, it was only necessary to approximately locate the face of the fiber vertically, which had previously caused issues with adhesion. Since the interface was located manually by the operator for each device, the length

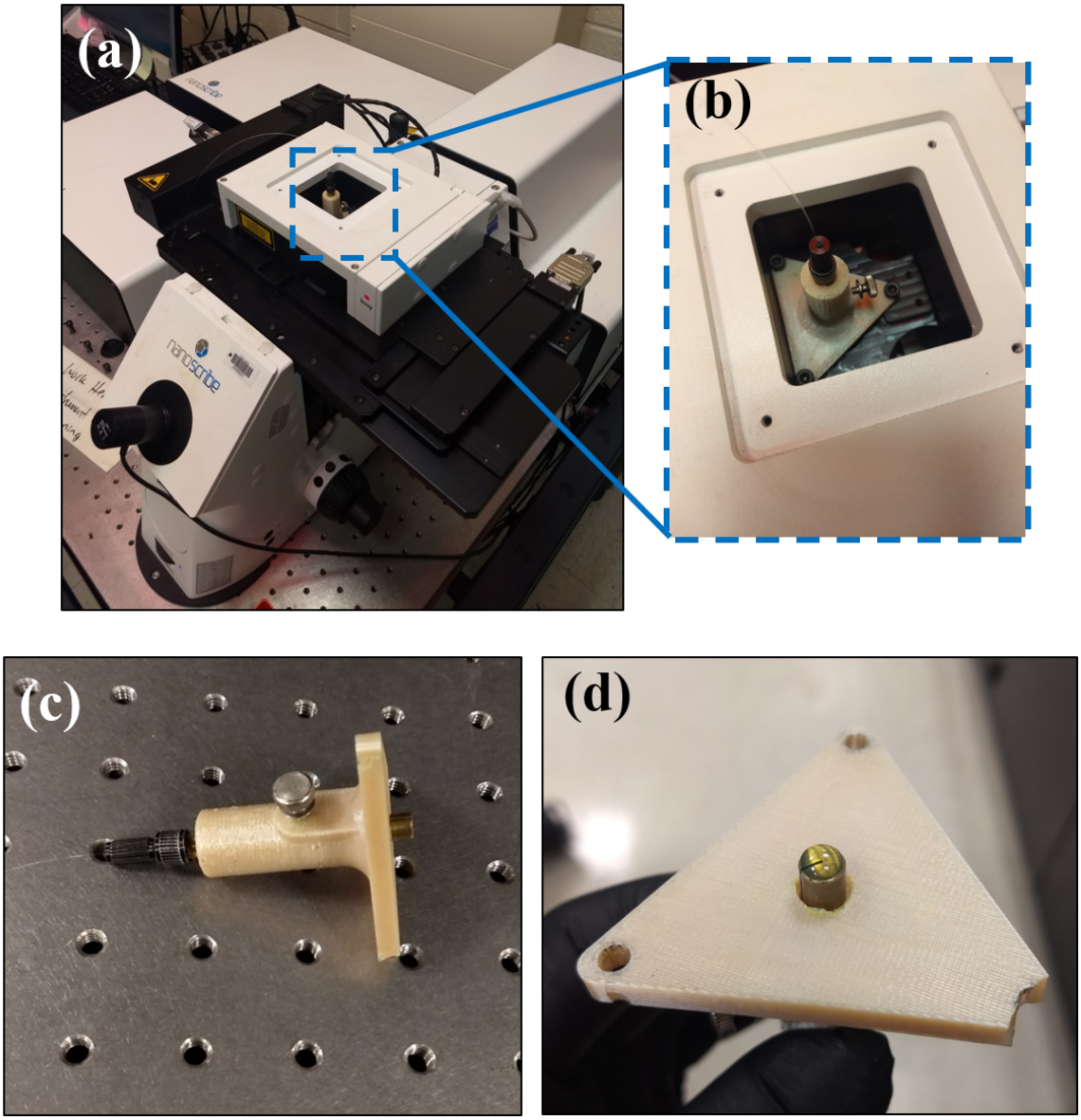

Figure 24: Important features of the fabrication process. (a) The Nanoscribe GmbH Photonic Professional GT microfabrication system. (b) A close-up of the fiber loaded in the machine. (c) The fiber chuck and custom jig. (d) IP-Dip resin deposited on the fiber chuck. Please note that while one of the corners of the jig is damaged, it was still able to screw securely into the substrate-plate and did not seem to influence fabrication.

of the cavity has a theoretical range of $+5\mu m$ with this process. The Nanoscribe was operated with the NanoWrite user interface. The key settings used for this device are included in table 2. Screen capture images of the Nanowrite software during

fabrication are included in figure 25.

The resin was specially formatted to only solidify after absorbing two-photons of a high energy threshold. This condition only occurred in a small portion of the laser beam, called the voxel (3D equivalent of a pixel). The minimum voxel size advertised by Nanoscribe was 150nm wide by 150nm long by 200nm tall. The voxel size used

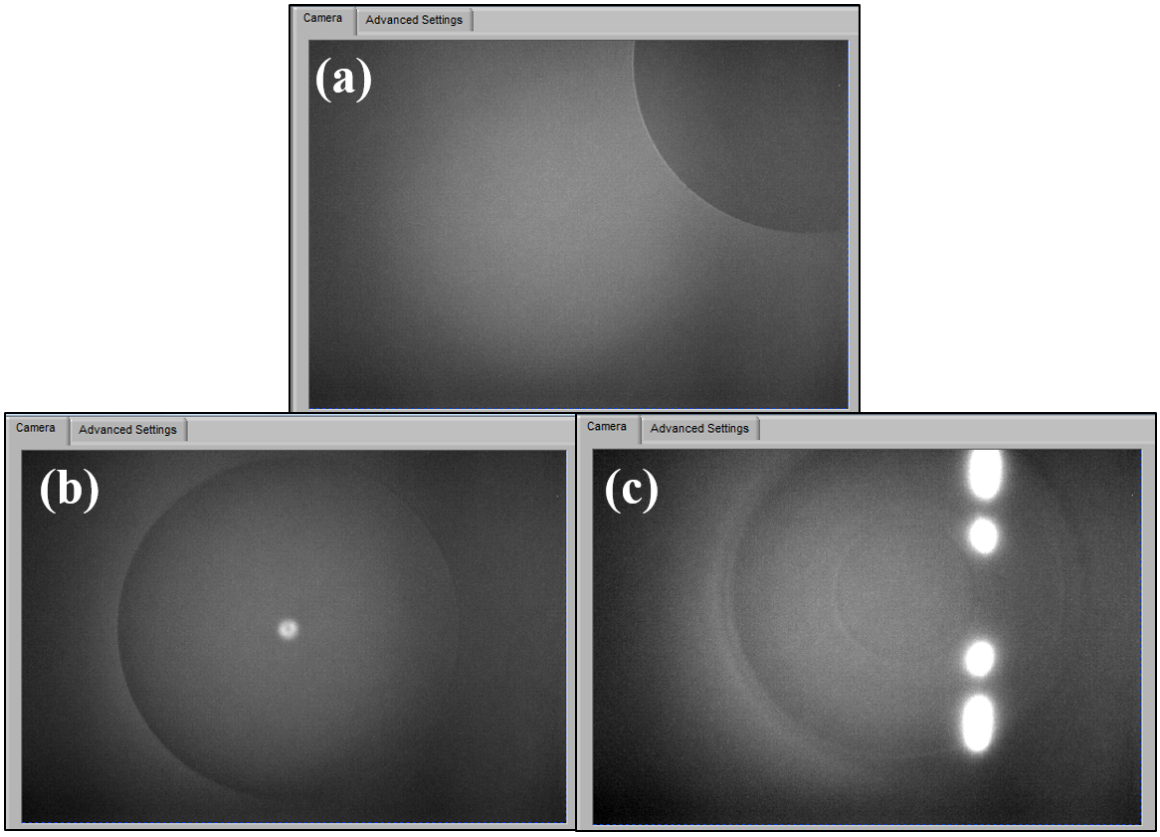

Figure 25: Screen capture images of the NanoWrite software during fabrication. (a) The fiber was located by raising the objective into the resin. (b) The of the fiber was used as an alignment mark. (c) The laser was scanned through the resin layer-by-layer according to the 3D model, in this case a spring-body pressure sensor was fabricated.

Table 2: Primary 2PP fabrication settings input to the Nanoscribe software.

XY Resolution	0.2	μm
Z Resolution	0.2	μm
Laser Power	40	%
Scan Time	10	mm/s

to fabricate the mechanically enabled FP cavity was 200nm wide by 200nm long by 200nm tall. The voxel traced through the design one layer at a time to produce a polymerized structure surrounded by resin. A graphic depicting this process is included in figure 26. This unexposed resin was developed away by soaking the fiber chuck inpropylene glycol methyl ether acetate (PGMEA), also called SU-8 developer. Halfway through the development, the fiber was extended several millimeters for the remaining 10 minutes to ensure no droplets of resin formed around the device. The device was bathed in Isopropyl Alcohol (IPA) for 10 min to remove the PGMEA. The device was then ready for manipulation or experimentation. Starting with a cleaved fiber, a single device took approximately 45 min to fabricate. Approximately 6 devices could be made in a 3-hour time block by running the Nanoscribe while other devices were bathed in the solvent.

The hinged FP cavity required three post-polymerization processes. First, the supports were broken and the hinged cavity was moved to the fully open position with a 5-μm diameter semiconductor analysis probe. This was performed under a microscope at 200x magnification, and required manual dexterity roughly equivalent to precise wire-bonding.

Next, a gold thin film was deposited onto the device to create the semi-reflective mirrors for the resonator. A small window of thicknesses existed for a successful device. A coating that was too thin would not improve the quality factor of the device, while a coating that was too thick would wash out all resonance features, reflecting all wavelengths. The most successful deposition for the final hinged device was performed at 100W for 52sec. The important recipe settings are included in table 3. Another deposition was attempted on the very top of the device in an effort to create a dual-cavity response. Unfortunately, this did not work as planned, and the device continued to exhibit a single-cavity response. This was because the third

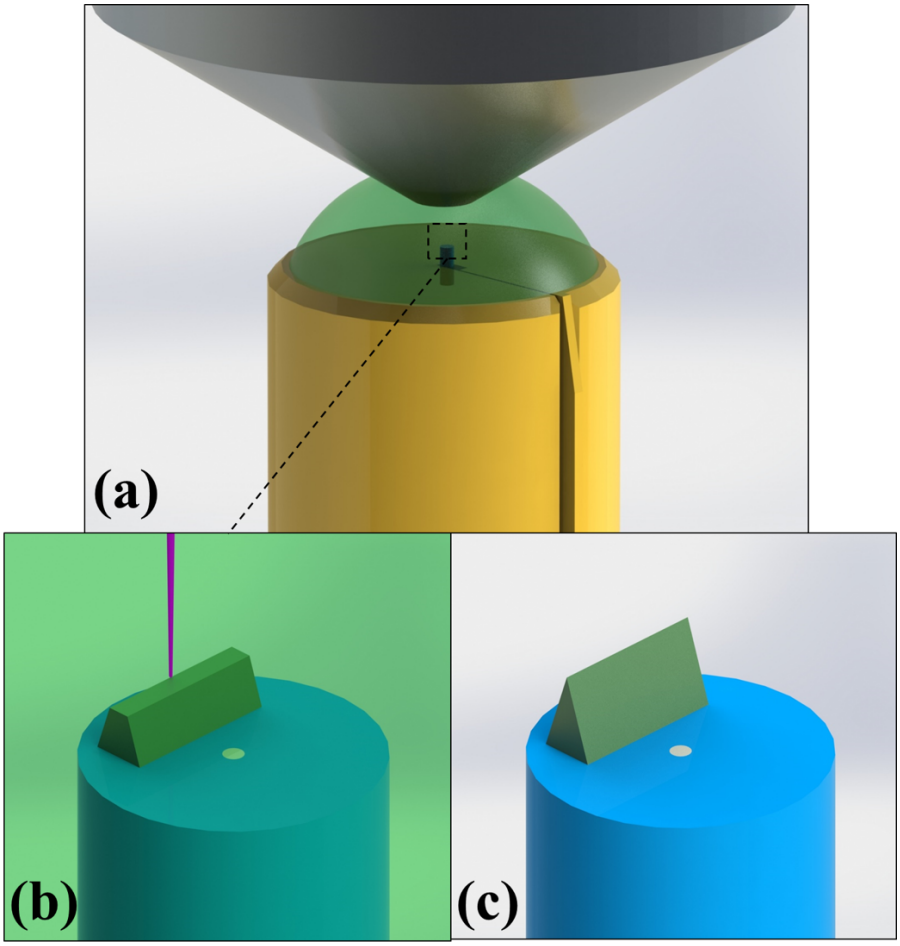

Figure 26: Graphic depicting the 2PP fabrication process. (a) Photoresin deposited onto a cleaved optical fiber loaded into a fiber chuck. The microscope objective of the Nanoscribe was lowered into the resin. (b) The laser was scanned through layer by layer to polymerize the desired structure. (c) The remaining photoresin was developed away to release the device.

mirror was flat, which scattered the reflections from the inner curved mirror. Future work could explore different sputtering settings and device geometries to achieve this, but there was not time to explore different options within the scope of this work.

Finally, the hinged portion was locked into the closed position. This was done in the same manner as opening the hinge. Best practice was to press one side of the hinge into the latch first, then press the rest into the stretched latch. The natural flexibility of the IP-Dip made such aggressive manipulations possible without damag-

Table 3: Plasma sputtering deposition settings used for the hinged FP cavity RI sensor reflective coating.

Gold in Lesker Plasma Sputtering System Cathode 1

Cathode Power	100	Watt
Cathode Mode	DC	
Burn-in Time	30	Sec
Burn-in Pressure	10	mTorr
Deposition Time	52	Sec
Deposition Pressure	5	mTorr
Stage Rotation	5	RPM
Fiber Placement	Center Stage	
Fiber Orientation	Vertical	

ing the device. Figure 27 shows optical microscope images of the post-polymerization manipulations. The device was then ready for RI sensing.

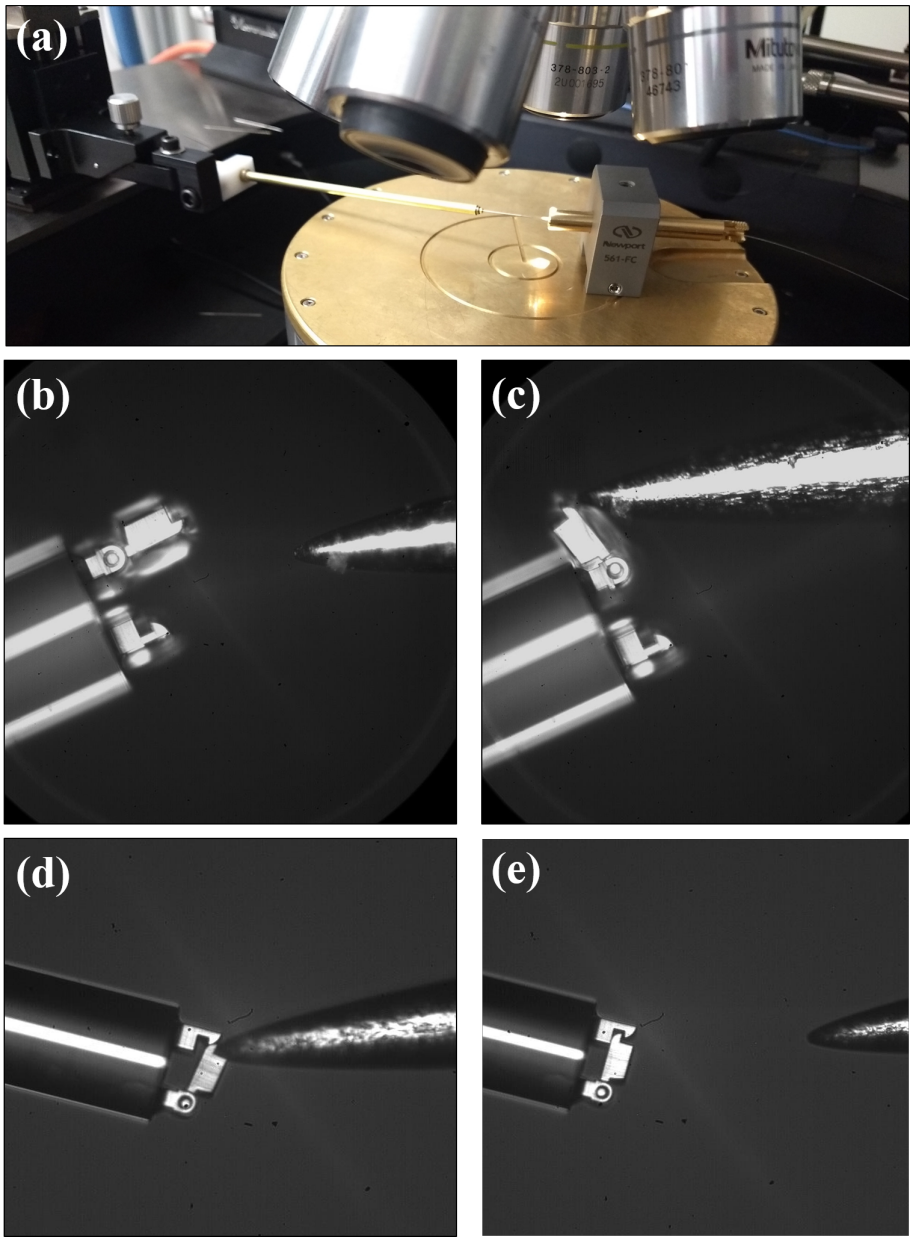

Figure 27: Optical microscope images of manipulating the hinged FP cavity with a probe. (a) Probe and fiber under a microscope. (b) Device as fabricated in half-open position (c) Device in fully-open position, ready for gold deposition (d) Device being closed after gold deposition (e) Device latched in place. Please note the device pictured is the slightly taller 33-μm device.

The variability in device geometry due to fabrication was dominated by the operator-dependant fabrication steps and various design choices. Most other uncertainty introduced by the fabrication equipment was assumed to be comparatively

negligible to maintain the scope of this work. Known sources of variability due to fabrication and their subsequent assumptions are:

- Adhesion pad scanned beneath the fiber face as located by the operator; $+5\mu m$ variation in cavity length.
- Alignment of the device to the core was performed manually by the operator; variation in lateral position was not included in the analysis of the results, but could be included in future, more robust analysis.
- Potential alignment error introduced during fabrication due to uneven tightening of the fiber-chuck jig onto the substrate plate; devices were visually inspected and thrown out if they contained a significant slant.
- The pin in its housing retained its clearance from fabrication; a variability in the cavity length of $\pm 1.25\mu m$ from movement of the pin could exist after the hinged mirror was latched in place. Angular misalignment caused by this clearance was not included in the analysis of the results.
- Uncertainty of the Nanoscribe's galvanometric and piezoelectric positioning system was $\pm 5nm$ according to the operating manual; the subsequent $\pm 5nm$ variability in height and lateral position were not included in the analysis of the results as they were significantly smaller than the other sources of variability.
- The reflective coating may have deposited differently to the slightly angled, polymer mirror compared to the flat, glass, fiber face; the reflective coating was assumed to be constant and uniform for this analysis.

3.2.4 Experiment Setup

The device fiber was spliced to an FC/APC patch cable from Fiber Instrument Sales (FIS) using a 3M Fibrlock II universal fiber splice. This enabled simple integration with optical equipment. A Sacher LaserTecnik TEC 520 variable wavelength laser and Pilot PZ 500 laserdiode controller was used as a light source. This was swept from 1460 - 1580nm at a rate of 1.6 nm per second using its internal stepper motor controlled by a LabView® virtual instrument (VI) on a laptop computer. On the same laptop computer, a function generator and the 3.5mm headphone jack were used to create a trigger to identify the start of the sweep. This functionality was not built into the Sacher laser. A mouse macro was used to ensure repeatable timing for each measurement. The sweep was inititated 6 ms after an impulse was sent by the function generator using the macro. Details of this software are included in appendix A.

The laser source was connected to the first port of a Thorlabs 6015-3-APC non-polarization maintaining optical circulator designed to operate from 1525-1610 nm. The optical circulator experiences low loss from port one to port two and from port two to port three, and experiences high losses in the reverse from port three to port two and from port two to port one. This creates a one-way device that allows the reflection from port two to be isolated and analyzed. Port two of the optical circulator was connected to a Thorlabs FPC025 two-paddle manual polarization controller, which was connected to the device fiber. Constant polarization improved the quality of the reflection response, but the specific polarization did not affect the results. Both paddles of the polarization controller were left in the upright position throughout testing. The other end of the polarization controller (port 2 of the optical circulator) was connected to the device fiber. The sensor fiber was spliced to a FIS simplex 9/125 FC/APC patch cable with a 3M Fibrlok II universal fiber splice. The third

port of the optical circulator was connected to a Newport model 1611 1-GHz low-noise photoreceiver. The DC output of the photoreciever was read by an Agilent 54641D mixed signal oscilloscope. This portion of the experimental setup was used in each test, and is pictured in figures 28, 29, and 30.

To measure the RI change of the water-IPA solution, the fiber was immersed in a vial containing a given mixture. The side-loading fiber chuck was mounted into a Newport 561-FC fiber chuck holder, essentially a steel block with a hole and set-screw. The holder made handling the device much easier, and was set on top of the glass vial to immerse the sensor. Solutions of different concentration were prepared by measuring the respective quantities of water and IPA. One graduation of the 5-ml graduated cylinder, $\pm$0.1ml, was taken as the confidence of each measured quantity. Multiple transfers were performed to create a final solution of 20ml. An uncertainty of $\pm$0.1ml was added for each use of the graduated cylinder to produce the volumetric concentration error bounds, which were carried into the % weight error bounds. The solution was vigorously mixed with a stainless steel straw for 30 sec prior to inserting the sensor. The fiber chuck was swirled through the solution for an additional 10 sec to encourage liquid to enter the cavity. The wavelength sweep was then initiated. After each test, the device was blown dry with compressed nitrogen for 30 seconds. One series was performed with concentrations varying from 40% to 100% IPA by volume at 10% intervals. The % weight of IPA in the solution was calculated using a density of 1g/ml for water and 0.785g/ml for IPA to compare with RI values reported in literature [105]. Three measurements were taken in each solution.

To measure temperature, the device was suspended above a hot plate by fixing a fiber chuck to an optical equipment stand. A thermocouple to monitor the air temperature was held at the same level fixed to another stand. The fiber chuck and device were maintained in the same position for the entire experiment. To take a reading,

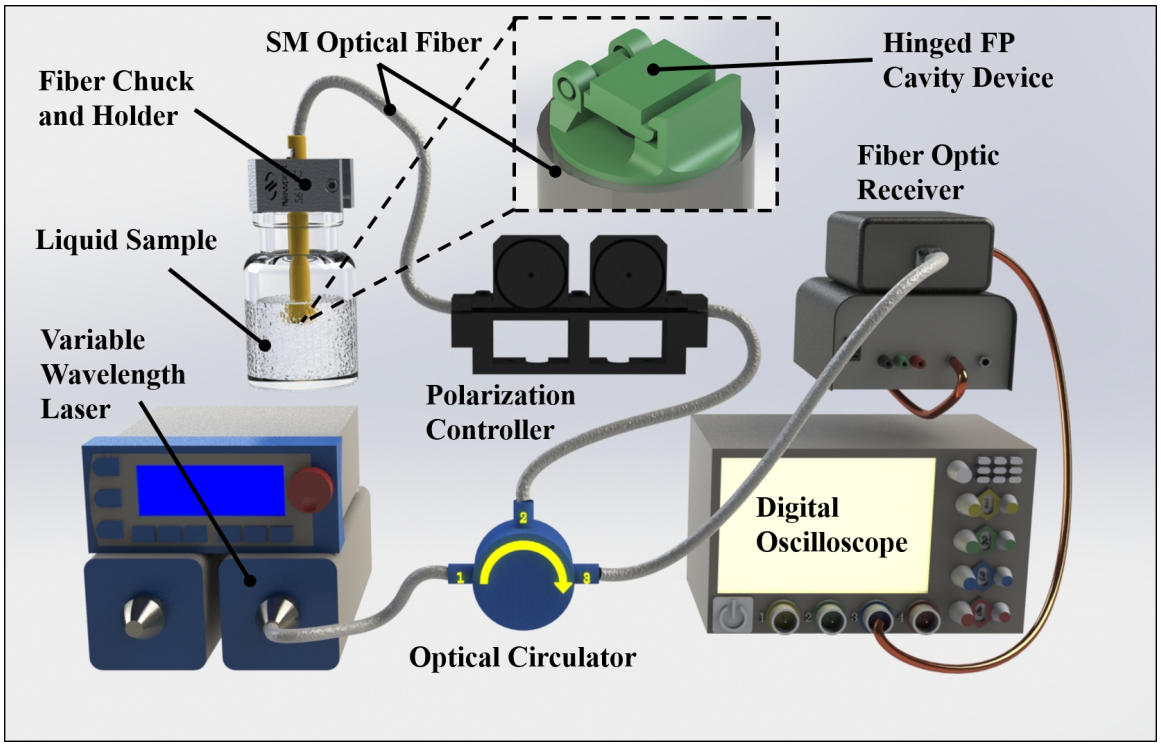

Figure 28: Experimental setup used to measure solution composition with the mechanically enabled FP Cavity device.

the hotplate was allowed to reach a particular temperature. The thermocouple was turned on as the wavelength sweep was started. The reading on the thermocouple at the end of the sweep was taken as the air temperature experienced by the device. The hotplate temperature was varied from room temperature to 250 °F at 50°F intervals. A measurement was only taken if the hotplate was within 2°F of its set point. The experiment was performed twice, once on the way up to 250°F and again on the way back down to room temperature in order to explore any hysteresis effects and gather more statistically significant data. The hotplate was brought to 300°C, but the data from this measurement was unfortunately lost. The thermocouple's operating manual reported an accuracy of ±(0.1%Reading +1°C), which was incorporated into each reported temperature. A graphic depicting the temperature measurement setup is included in figure 29.

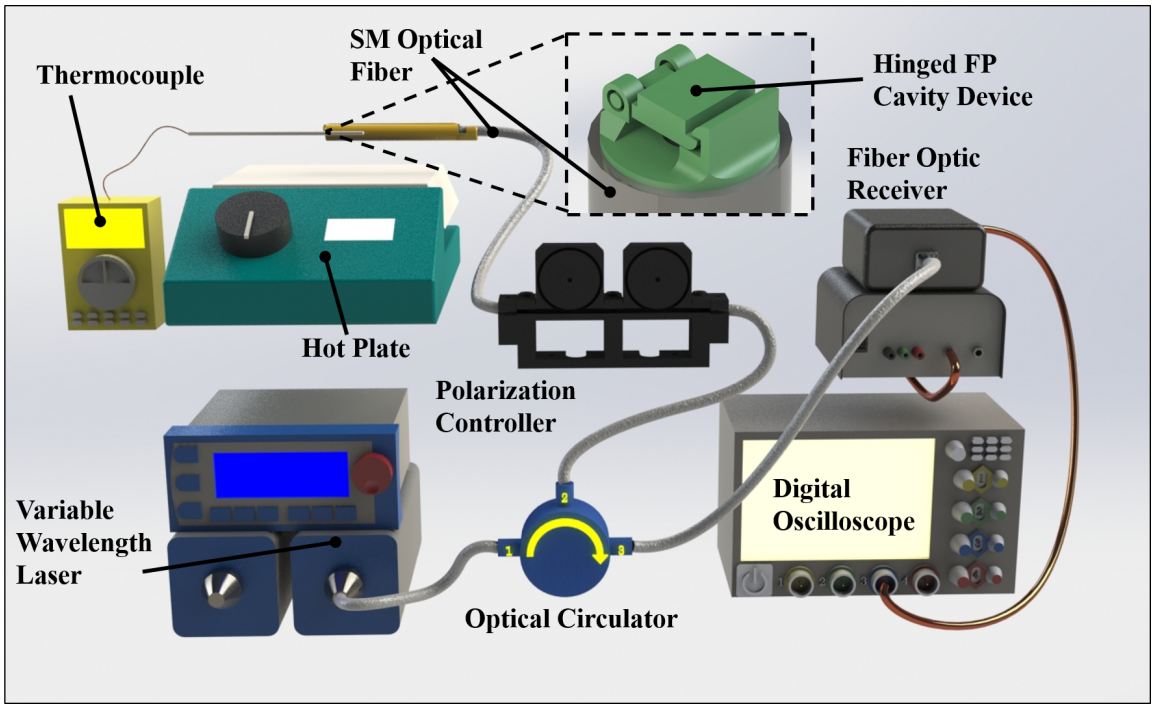

Figure 29: Experimental setup used to measure ambient temperature with the mechanically enabled FP Cavity device.

To measure pressure, the device was mounted inside a Best Value Vacs vacuum chamber. The fiber chuck and holder were used to hold the device again, and placed inside the chamber. A 1/4" hole was drilled into the acrylic top of the chamber to pass the fiber through. A piece of high density foam was cut and placed around the fiber to seal with the top of the chamber. A compression-fitting port on the chamber was connected to a Thomas 607CA32C electric vacuum pump. A small leak existed somewhere in the vacuum chamber, and a constant pressure was maintained by slightly opening the valve to the vacuum pump, pulling vacuum back to the desired level occasionally throughout a reading. This was done manually while observing the vacuum gauge. To account for this variation, an uncertainty of two graduations on the gauge above or below the desired reading was used, giving a confidence interval of $\pm 0.68 kPa$ for each reported pressure level. The pressure experiment was performed twice, once on the way down to 16.34 kPa and again on the way back to atmospheric

pressure in order to explore any hysteresis effects and gather more statistically significant data. A graphic depicting the pressure measurement setup is included in figure 30.

The variable wavelength laser had two problematic features that were removed from each measurement by processing the data in MATLAB®. First, the laser was designed primarily to operate within close proximity of a single wavelength, not swept over its entire operating range. Therefore, only the current could be controlled, so the output power was highly dependent on wavelength. This manifested as the curve seen in figure 31 (a). This wavelength-dependent floor was removed from the readings for analysis by measuring the response of a blank, cleaved fiber coated in a thick layer of gold, and subtracting this from each reading with a device. The laser's motor also introduced a high-frequency ringing as it moved the internal grating to sweep wavelength. This can be seen in figure 31 (b). This high frequency was particularly

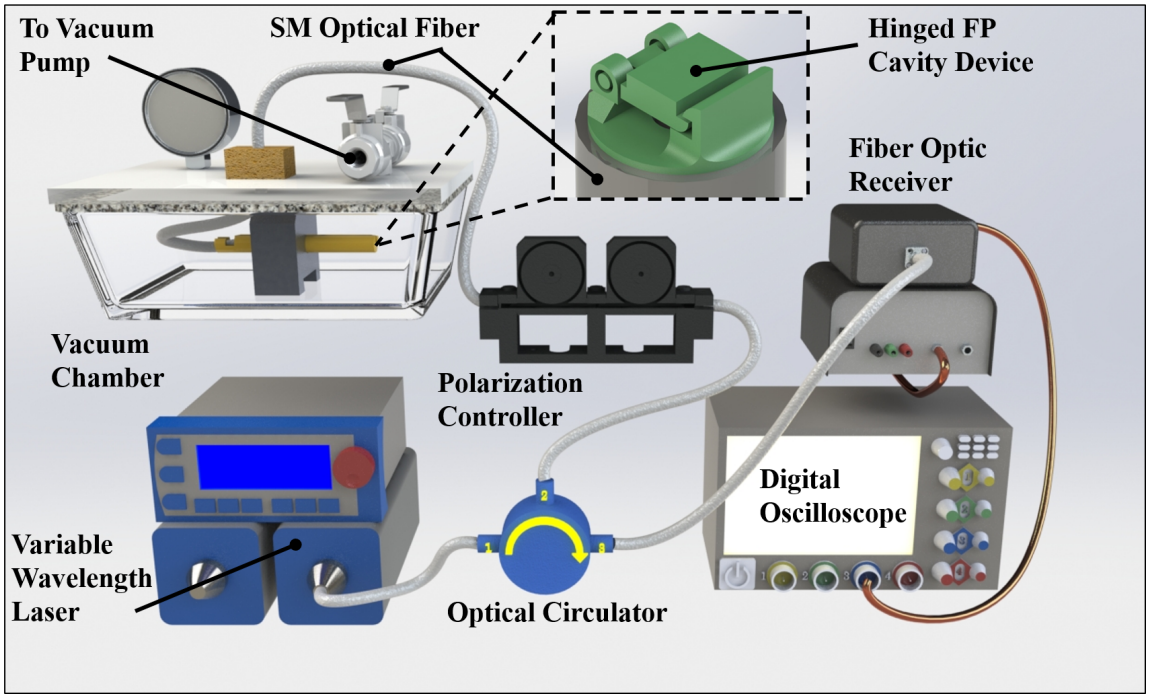

Figure 30: Experimental setup used to measure vacuum pressure with the mechanically enabled FP Cavity device.

problematic as it added significant confusion to the peak value of a resonant feature.. The ringing was suppressed in the data by using a moving average filter in MATLAB® using 20 points. This also reduced the quality factor of the resonant peaks, but the increased clarity in peak wavelength location was considered worth the loss of resolution. The same filter was applied to all measurements taken with this device. A selection of this code is included in appendix A. An example of the final data used for analysis can be seen in figure 31 (c). An alternative method for locating the resonant peak in the presence of the high frequency noise is to fit an appropriate distribution curve, which was not accomplished in the scope of this thesis, but would make for promising future work.

Several sources of systematic measurement uncertainty were folded into the confidence interval of each measurement. The accuracy of the laser was included in its

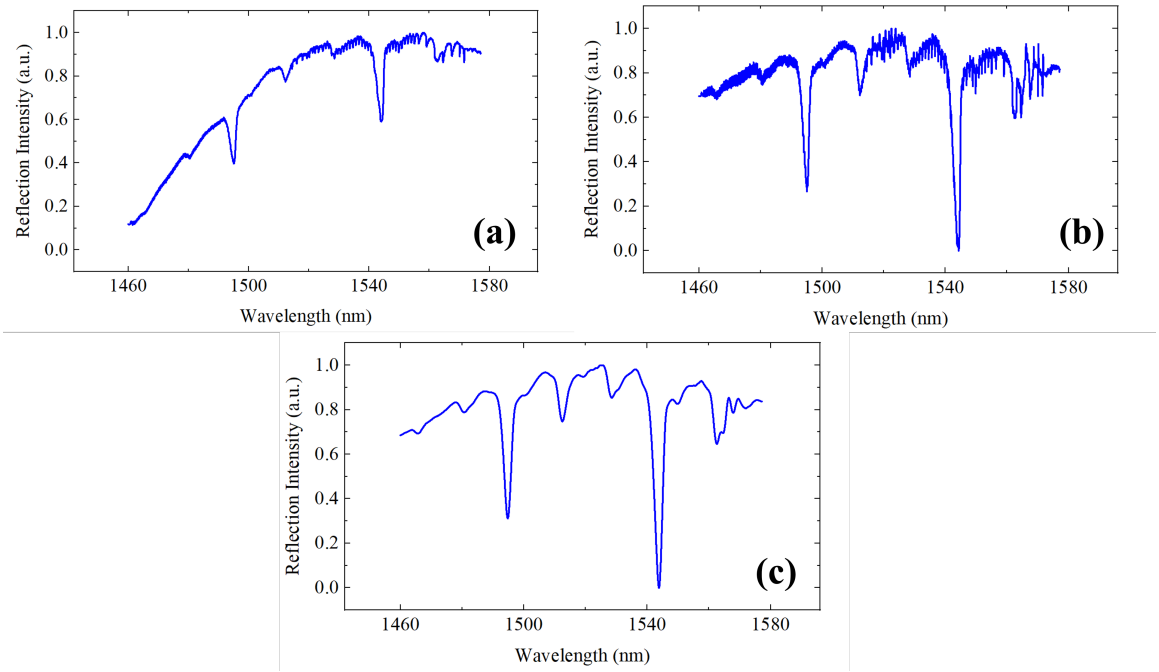

Figure 31: Filters applied to the the reflection data for more accurate analysis. (a) Raw output with power dependent on wavelength. (b) Spectrum after subtracting the power floor. (c) Equipment-induced ringing filtered out by MATLAB®.

operating manual as ±0.05nm. The horizontal (time domain) accuracy of the oscilloscope was calculated as directed in its operating manual and converted to wavelength by multiplying by the rate of the wavelength sweep. The documentation for the photoreciever did not include accuracy information, so it was calculated in the same way as the oscilloscope. Given that the photoreciever was at least 10 years newer than the oscilloscope and designed to capture high frequency signals, this was assumed to be a conservative estimate of its accuracy. To account for error introduced in the MATLAB® post-processing, 25 resonant peaks from several measurements were examined. Each peak was isolated from the rest of the spectrum and normalized to its minimum and maximum values, and the number of points above 0.95 (within 5% of the peak) were counted. The greatest number of points observed above this threshold was 12, with most peaks exhibiting between 6-10 points. The potential wavelength range over 12 points was used as a conservative estimate of the error introduced by the post-processing. These measurement-induced uncertainty values are collected in table 4.

For repeated experimental measurements, the standard error of the mean was calculated from the standard deviation, σ, and the number of measurements n to be:

$$SE = \frac{\sigma}{\sqrt{n}}. \tag{19}$$

This statistically derived uncertainty obtained from the measured values, U_A, was

Table 4: Collected measurement-induced wavelength location uncertainty

Source	**Uncertainty**	**Calculation**
Variable Wavelength Laser	± 0.05nm	Provided in manual
Oscilloscope	± 0.16nm	0.1% Screen Width +1 Sample Period
Photoreciever	± 0.12nm	0.1% Measurement Length +1 Rise Time
MATLAB® Post-Processing	± 0.48nm	1/2(12 points × 0.08nm/point)
Total from Measurement	± 0.52 nm	$\sqrt{U_{B1}^2 + U_{B2}^2 + U_{B3}^2 + U_{B4}^2}$

combined with the uncertainty of the instruments, U_B, to yield the total uncertainty:

$$U_{total} = \sqrt{U_A^2 + U_B^2}. \tag{20}$$

Several other sources of error could have impacted measurements, but were assumed to be negligible to maintain the scope of this work. A non-exhaustive list of these factors and their associated assumptions are:

- Variations in ambient temperature; assumed to be constant at 22°C.
- Variations in ambient relative humidity; assumed to be constant at 40%.
- Wavelength dependence of length, RI, and the speed of light; assumed to be independent of wavelength over the bandwidth of interest.

3.3 Results

Before it was used as a sensor, the reflection spectrum of the mechanically enabled FP cavity was compared to several popular models to determine device and signal properties. The most common model for a Fabry–Pérot cavity is the Airy Distribution [106],

$$I_{out} = \frac{I_{in}(1-R)^2}{(1-R)^2 + 4Rsin^2(\phi)}, \tag{21}$$

where R is the reflectance of the mirrors, assumed to be equal, and ϕ is half of the round-trip phase shift at a given frequency in terms of its distance from the resonant frequency v_0 at an FSR of Δv_{FSR} [106],

$$\phi = \pi \frac{v - v_0}{\Delta v_{FSR}}. \tag{22}$$

The Airy distribution was modeled over our available bandwidth, 1460 - 1580 nm, and subtracted from 1 to simulate reflection,

$$I_{refl} = 1 - I_{out}. \tag{23}$$

Since it was being used to estimate reflectively, several key factors were taken from the measured spectrum. The resonant wavelength and FSR were taken from the measured result, and both the reflection spectrum and Airy distribution was normalized between zero and one to ensure matching magnitudes. The reflectance of both mirrors was assumed to be the same since they experienced the same reflective coating. The MATLAB® curve-fitting application using a trust-region algorithm was used to extract a value of for reflectance, R in equation 21. The reflectance was found to be 0.83±0.0082 as the 95% confidence interval from the curve-fitting model.

Next, the quality factor of the resonance feature was estimated using the inverse

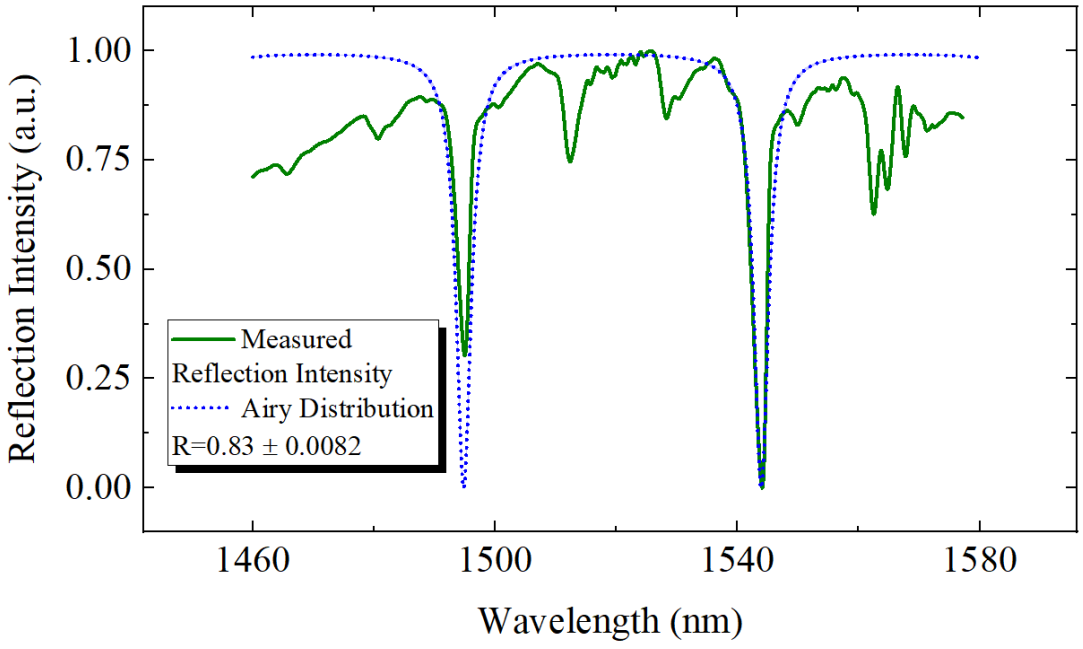

Figure 32: Airy distribution fit to the reflection spectrum of the mechanically enabled FP cavity RI sensor in air at room temperature to determine reflectance.

Lorentzian line shape [107],

$$L = \frac{(1/(v - v_0))^2}{(1/\tau)^2 + (v - v_0)^2} \tag{24}$$

where v is the frequency of a given wavelength, v_0 is the frequency of the resonant wavelength, and τ is related to the quality factor Q by,

$$\tau = \frac{2Q}{v_0} \tag{25}$$

The model was compared to the second resonance feature of the mechanically enabled FP cavity in air at room temperature. The curve fitting application from MATLAB® was used again with a trust-region algorithm to fit equation 24 with a value of Q. With a 95% confidence interval, the curve-fitting model predicted a quality factor of 492.3 ± 25.8, which is pictured in figure 33. The assymetry of the measured reflection is likely due to a misalignment of the hinged cavity. Future work could explore the physical meaning behind a skewed-Loretzian fit which would likely fit the data more accurately.

The FSR of the response was also measured and compared to the theoretical value. The first resonance occurred at $1495.8nm \pm 0.52nm$. This uncertainty stems from the measurement techniques described in subsection 3.2.4. Using equation 13, 1.0003 for the RI of air, and the cavity length of $22\mu m$, the FSR was predicted to be 50.84, putting the second resonant peak at 1546.6. The second resonance was measured at $1546.2nm \pm 0.52nm$ for a FSR of $50.35 \pm 1.04nm$, agreeing closely with the predicted values.

Liquid RI measurements were made in solutions of IPA and water at various concentrations. The IPA component was varied from 40 to 100 percent by volume. The % weight of IPA in the solution was calculated using a density of 1g/ml for

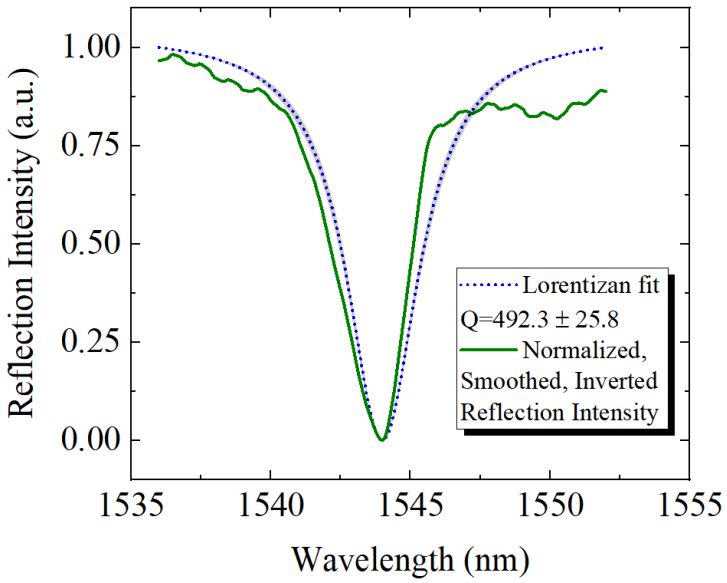

Figure 33: Lorentzian fit normalized and fit to the second resonant peak of the mechanically enabled FP cavity RI sensor in air at room temperature to determine quality factor.

water and 0.785g/ml for IPA. A solution with more than 60% water by volume was unable to enter the device. This was a downside of the small cavity, as liquids with strong cohesion could not overcome the surface tension of the small opening. Since IPA has a higher RI than water (n=1.3776 for IPA and n=1.333 for water) increasing the concentration of IPA was expected to cause a red-shift in the resonant feature according to equation 3. This can be seen in the selection of three measurements included in figure 34.

The RI of IPA and water solutions has been shown experimentally to vary non-linearly [105], which was captured in the results of this experiment. The measured locations of the resonant features are plotted in figure 35. The error bars capture both the uncertainty of the measurement equipment and 1 standard error from the repeated readings as described in equation 20. They are compared with the results of equation 3. The cavity length and mode orders for the calculations were chosen within the length design tolerance of $22 + 5\mu m$ to align as closely as possible with

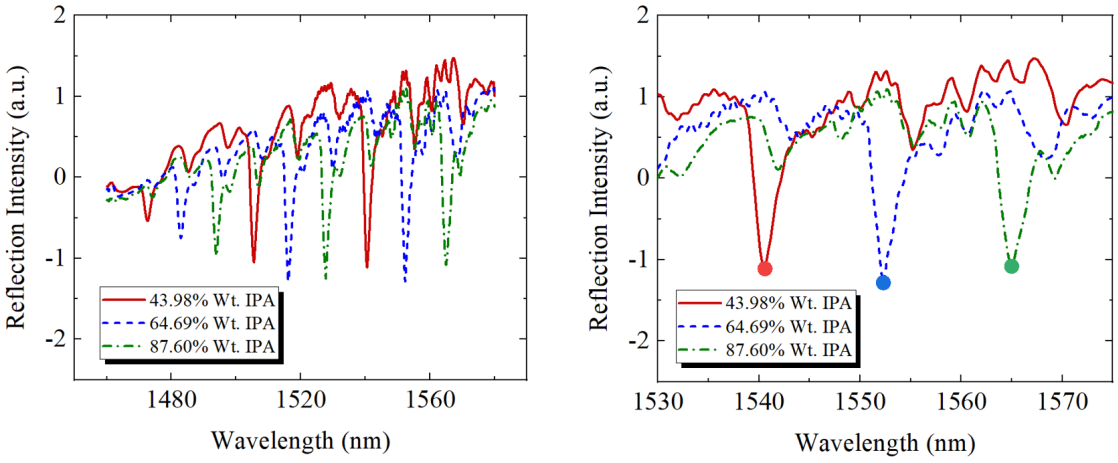

Figure 34: Three select reflection readings demonstrating the red-shift in resonant wavelength as a function of solution composition.

the measured data, based on visual inspection. The extracted cavity length varied between experiments, but falls well within the $\pm 1.25 \mu m$ tolerance allowed by the clearance of the pin within its housing.

A close-up view of a particular resonance event is pictured in figure 36. This also includes a polynomial fit that could be used to extract the weight concentration of liquid RI from the shift in resonant wavelength. This is included in equation 26. The fit and its prediction band were calculated from repeated measurements only, not the equipment measurement error:

$$\lambda_0 = (1.71 \pm 0.20)_{[\frac{nm}{\%Wt\ IPA}]} C - (0.0089 \pm 0.0015)_{[\frac{nm}{\%Wt\ IPA^2}]} C^2 + (1479.77 \pm 6.17)_{[nm]} \quad (26)$$

.

Taking the values from the experiments performed in [105] for each % weight measured, the actual RI value can also be determined. Figure 36 contains a plot of the measured resonance feature locations in terms of the solution's RI. These are compared to the resonant wavelengths predicted by equation 3, with the same l and m

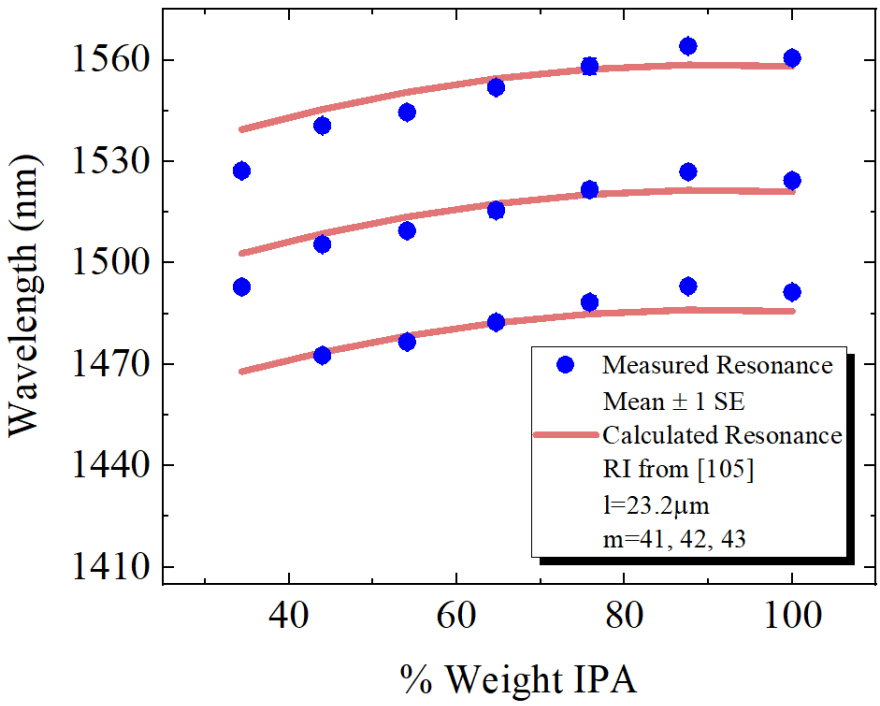

Figure 35: Resonant wavelength locations in different solutions of IPA and water. The error bars represent both ±1 standard error of the mean from the repeated measurements combined with the instrument uncertainty, but are difficult to see on this scale. The calculated resonant peaks were found with equation 3 at a length and modes extracted to match measured data within the design tolerances.

values extracted from figure 35. A linear fit and 95% prediction band were calculated again based on the repeated measurements. The fit indicates a sensitivity of 1992.47 ± 102.85 nm/RI, and is included in equation 27. A plot of the resonant wavelength shift in terms of the solution RI is included in figure 37.

$$\lambda_0 = (1992.47 \pm 102.85)_{[\frac{nm}{RI}]} RI - (1182.84 \pm 141.0)_{[nm]} \tag{27}$$

The mechanically enabled FP cavity RI sensor also showed a linear response with changes in its surrounding temperature. Figure 38 shows the measured resonant wavelengths as the temperature was both raised and lowered. The error bars include only the instrument induced measurement error, since these measurements were not

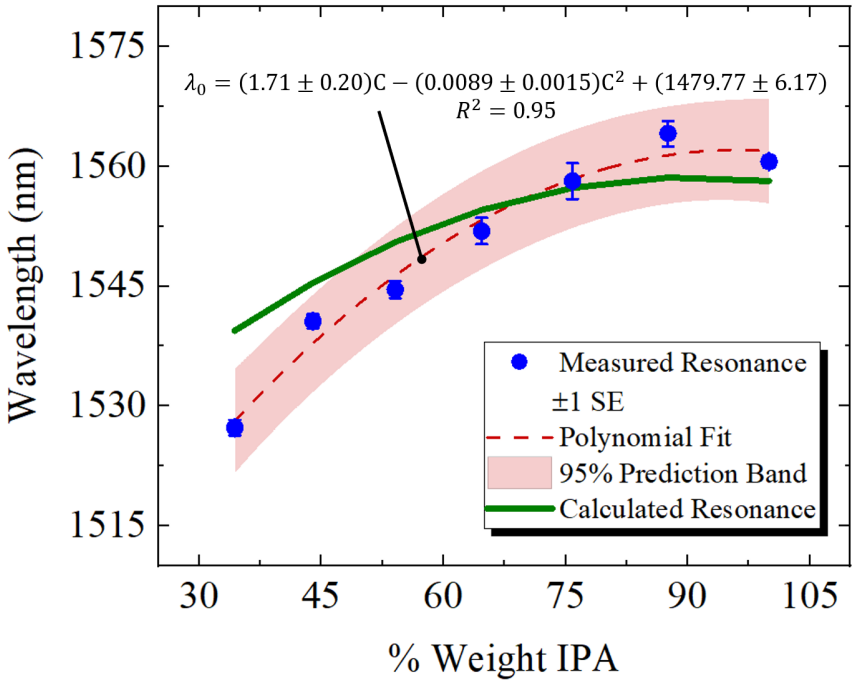

Figure 36: Shift in resonant wavelength due to changes in concentration of IPA and water solutions. The error bars represent both ±1 standard error of the mean from the repeated measurements and the instrument uncertainty. The calculated resonant peaks were found with equation 3 at a length and modes extracted to match measured data within the design tolerances. The horizontal error bars from the accuracy of the graduated cylinder were too small to view at this scale. The polynomial fit and its prediction band were calculated from on the repeated measurements only.

combined statistically due to the significant hysteresis. Equation 3 was again used to extract values for l and m that agree with the fabrication tolerance, the pin-clearance, and the values extracted in the liquid RI sensing experiment. When both the thermal expansion of the base and mirror are combined with the change in refractive index of air in response to temperature, the linear fit between the two measurement series aligns well with the resonant wavelengths predicted by equation 3. The fit is included in equation 28, and was calculated with 95% prediction bounds based on the two repeated measurements.

$$\lambda_0 = (0.20 \pm 0.052)_{[\frac{nm}{^\circ C}]}T + (1549.19 \pm 1.86)_{[nm]} \tag{28}$$

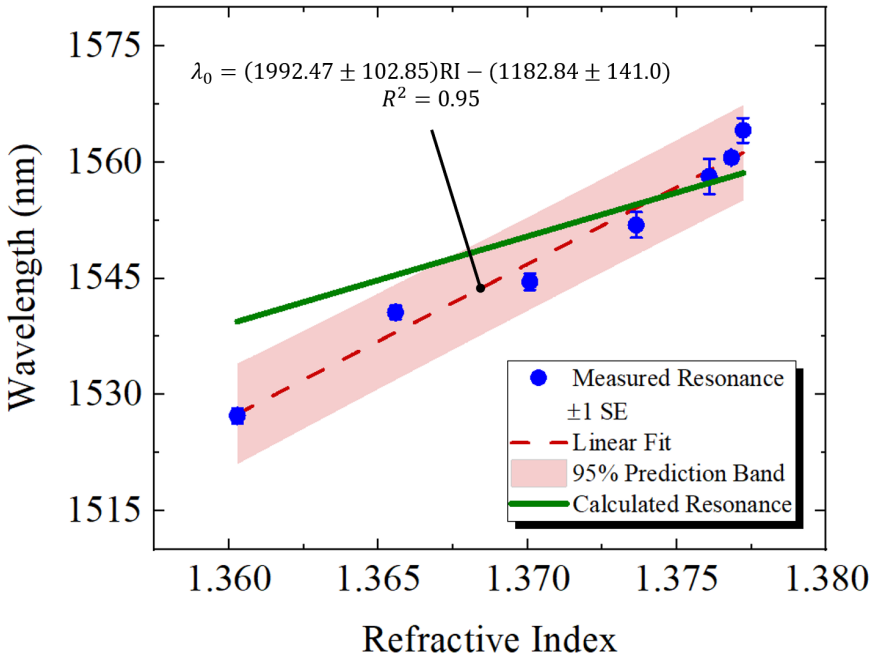

Figure 37: Shift in resonant wavelength as a function of the RI change in the solutions. The error bars represent both ±1 standard error of the mean from the repeated measurements and the instrument uncertainty. The calculated resonant peaks were found with equation 3 at a length and modes extracted to match measured data within the design tolerances. The horizontal error bars from the accuracy of the graduated cylinder were too small to view at this scale. The linear fit and its prediction band were calculated from the repeated measurements only.

Figure 39 contains a close-up plot of a resonance event and these equations. The hysteresis is likely caused by a slow thermal response of the polymer when expanding and contracting with temperature changes. Future work could evaluate and quantify this time-dependence to improve the calibration of the device as a temperature sensor.

The pressure test showed another predominately linear response. The results represent two runs, one raising the pressure and one lowering the pressure. Equation 3 was used to extract a cavity length and mode orders that aligned with the measured results and design tolerances. The RI of air at each pressure was predicted with the NIST metrology database [28]. The measured resonant peaks compared to those calculated with these parameters are included in figure 40. The vertical error bars

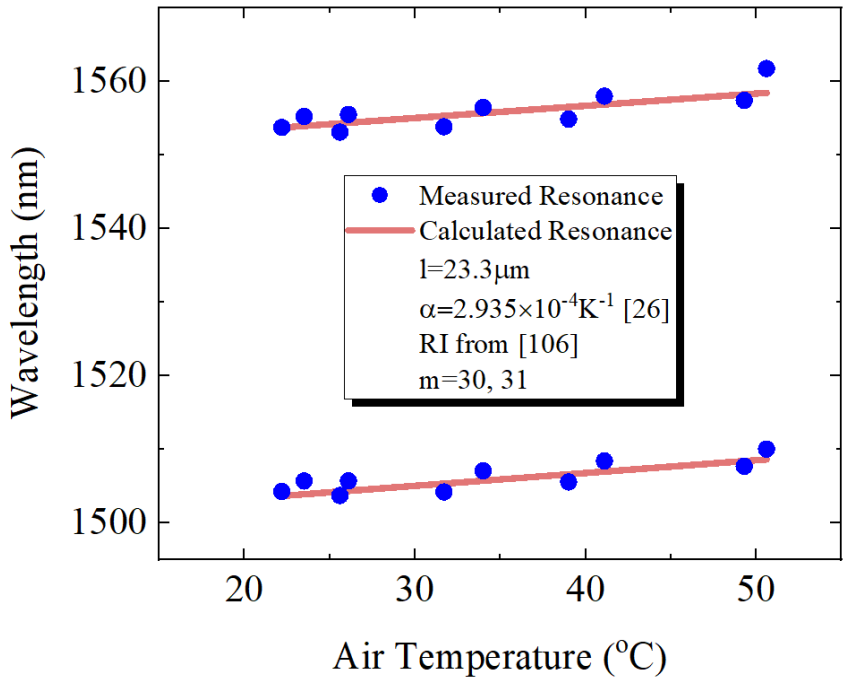

Figure 38: Measured resonant wavelength locations compared to values calculated with equation 3, and extracted values of l and m that match known dimensions and the measured results. Error bars include only the uncertainty estimated from the measurement instruments, but are difficult to see on this scale.

represent the estimated measurement error from the equipment, as each point was plotted separately to observe the hysteresis. The horizontal error bars represent the accuracy of the thermocouple. They are not seen in the scale of figure 40, but can be seen in the close-up image in figure 41. The hysteresis is likely caused by outgassing from the polymer cavity slightly changing its length, and a drop in relative humidity after the chamber was evacuated initially. Further experimentation in positive pressure and repeated measurements at vacuum pressures are needed to further evaluate the cause of the hysteresis.

A linear model was fit to the combined data, and plotted in figure 41. The fit and its prediction band were calculated using the measured data, not the equipment uncertainty. Calculations done in the NIST database were performed assuming a constant relative humidity of 40%. The calculated resonant peaks per equation 3 fall

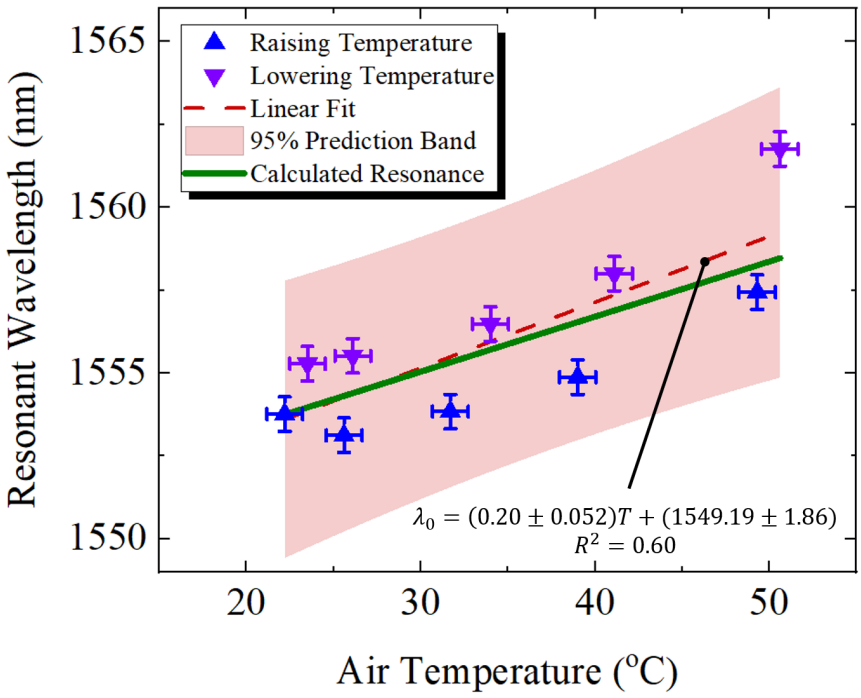

Figure 39: Measured resonant wavelength locations compared to values calculated with equation 3, and the extracted values of l and m seen in figure 38. The vertical error bars show only the measurement instrument uncertainty. The linear fit and its prediction band were calculated from the repeated measurements only. The horizontal error bars show the accuracy of the thermocouple.

within the 95% prediction band of the linear model, but outside of the measurement uncertainty of the individual values. The steeper slope is again likely caused by initial outgassing and change in relative humidity, which repeated testing could verify. The model exhibited an R^2 value of only 0.46, due to the hysteresis difference, and is included in equation 29.

$$\lambda_0 = (0.016 \pm 0.0049)_{[\frac{nm}{kPa}]}P + (1524.32 \pm 0.32)_{[nm]} \tag{29}$$

The results gathered from the mechanically enabled FP cavity device are compiled in table 5.

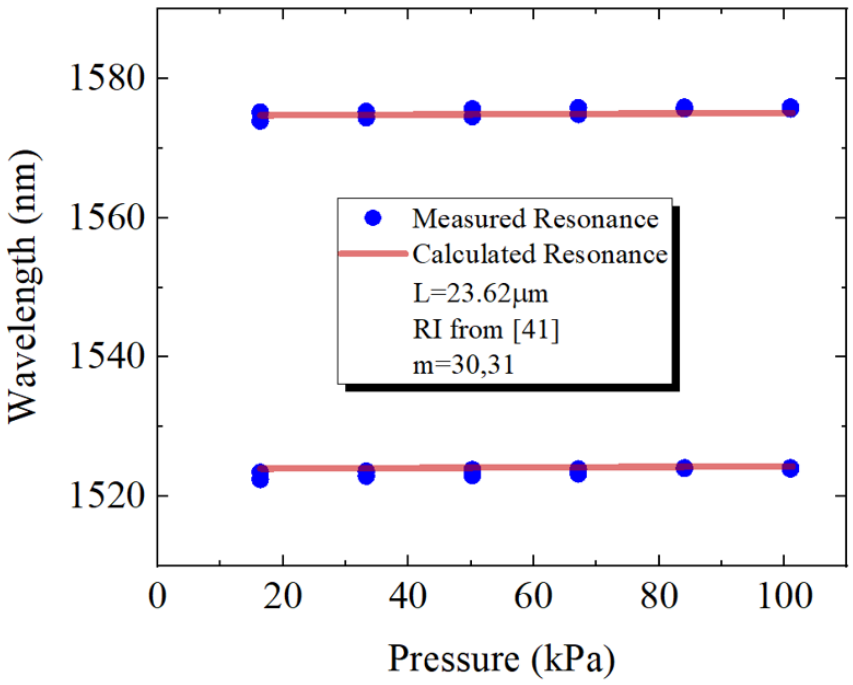

Figure 40: Locations of the resonance features at different pressure values inside a vacuum chamber. The measured values are compared to the calculated resonant peaks from equation 3 with a length extracted from the design tolerance and RI provided by [28].

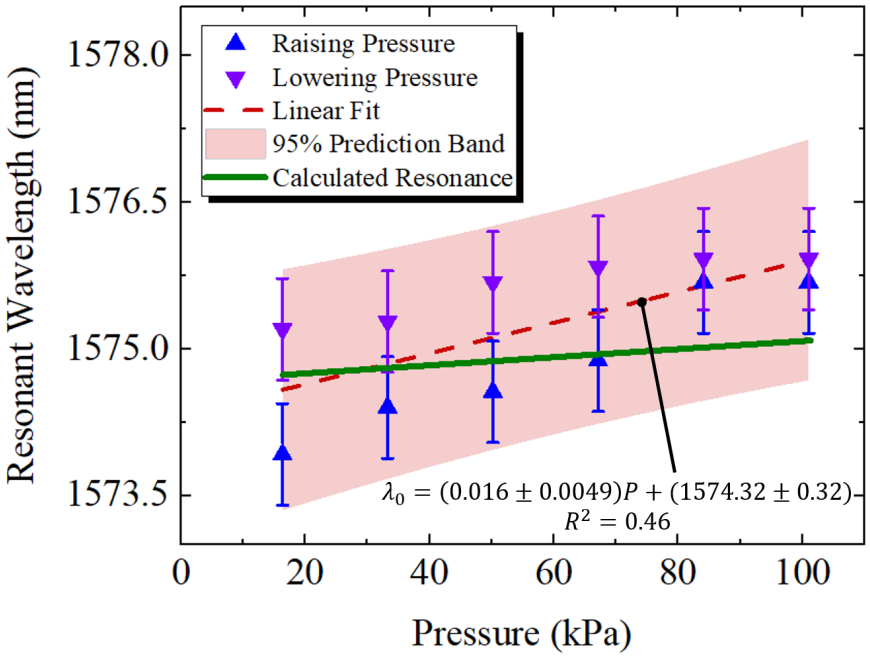

Figure 41: Locations of one resonance features at different pressure values. The measured values are compared to the calculated resonant peaks from equation 3 with a length extracted from the design tolerance and RI provided by [28]. The vertical error bars represent the instrument uncertainty. The horizontal error bars of the vacuum level uncertainty were not visible at this scale. The linear fit and its prediction band were calculated from the repeated measurements only.

Table 5: Mechanically enabled FP cavity RI sensor results.

FSR	50.35 ± 1.04nm
Reflectance	83%±0.82%
Quality Factor	492.3 ± 25.8
RI Sensitivity (Linear Fit)	1992.47 ±102.85 nm/ΔRI
Total Observed Shift from RI	33.35 ±1.36 nm/0.017 ±1.79 × 10^{-5} ΔRI
Smallest ΔRI Measured	8.63×10^{-}5 ±2.32×10^{-}5
Temp. Sensitivity (Linear Fit)	0.20±0.052 nm/°C
Total Observed Shift from Temp.	8.0 ±1.04 nm/28.4 ±2.07°C
Smallest ΔT Measured	2.6° ±2.01°
Press. Sensitivity (Linear Fit)	0.016±0.0049 nm/kPa
Total Observed Shift from Press.	1.76 ±1.04 nm/84.66 ±1.35 kPa
Smallest ΔP Measured	16.93±1.36kPa

3.4 Conclusion

The mechanically enabled FPcavity RI sensor successfully demonstrated a monolithically integrated dynamic structure fabricated with extensive 3D freedom at the micron scale. Selective and controllable thin film deposition with traditional semiconductor fabrication methods was realized with a multi-position hinged mirror. A reflective coating of gold was deposited to create two semi-mirrors with a reflectance of approximately 83%±0.82%, a resonance quality factor of approximately 492.3±25.8. A curved surface and latching mechanism aided in stabilizing the reflection response of the device, while a short, 22-μm cavity length further improved alignment insensitivity. The device successfully measured changes in liquid solution refractive index, ambient temperature, and vacuum pressure by monitoring shifts in the cavity's resonant wavelengths. Linear fits to experimental data indicate resonant wavelength shift sensitivities of 1992.47 ±102.85 nm/ΔRI, 0.20±0.052 nm/°C, and 0.016±0.0049 nm/kPa. Sensing resolution could be improved by fitting an appropriate distribution to each peak and avoiding the filter, and by improving the repeatability of each measurement by mechanically fixing the hinge.

Future work with the mechanically enabled FP cavity RI sensor could include,

- Test all parameters more in-depth to determine absolute resolutions, response times, and fatigue effects, and to explore the source of hysteresis effects.
- Create of a self-referencing two-cavity device by adding a mirror with greater curvature on the top of the polymer cavity and determining an appropriate reflective coating.
- Further increase reflectance and quality factor by exploring different materials and recipes for reflective coatings.
- Reduce variation in the cavity length by mechanically fixing the pin and improving the consistency of the fabrication process.
- Explore integration of 2PP microfabrication onto other substrates, such as complementary metal oxide semiconductor (CMOS) integrated circuits or Micro-Electro-Mechanical Systems (MEMS).

IV. High-Deflection Spring-Body Pressure Sensor

4.1 Chapter Overview

The high deflection spring-body pressure sensor was intended to leverage the mechanical success of the mechanically enabled Fabry–Pérot (FP) cavity and the 3D freedom afforded by the two-photon polymerization (2PP) microfabrication technique. Instead of measuring pressure by refractive index (RI) change, this device changed cavity length in response to differential pressure. This was achieved by capturing a small pocket of atmosphere inside the cavity during fabrication. When placed in the vacuum chamber, the pressure differential caused the pocket to expand. This technique is popular in Micro-Electro-Mechanical Systems (MEMS) pressure sensors, and has been demonstrated on several fiber-tip sensors as well [17, 18, 19, 63, 59, 65]. This device sought to use a spring-body to increase deflection from differential pressure. The spring-body could not be fabricated with traditional semiconductor fabrication techniques, and highlights the versatility of 2PP microfabrication. The expansion of the cavity alters which wavelengths resonate and transmit through the device.

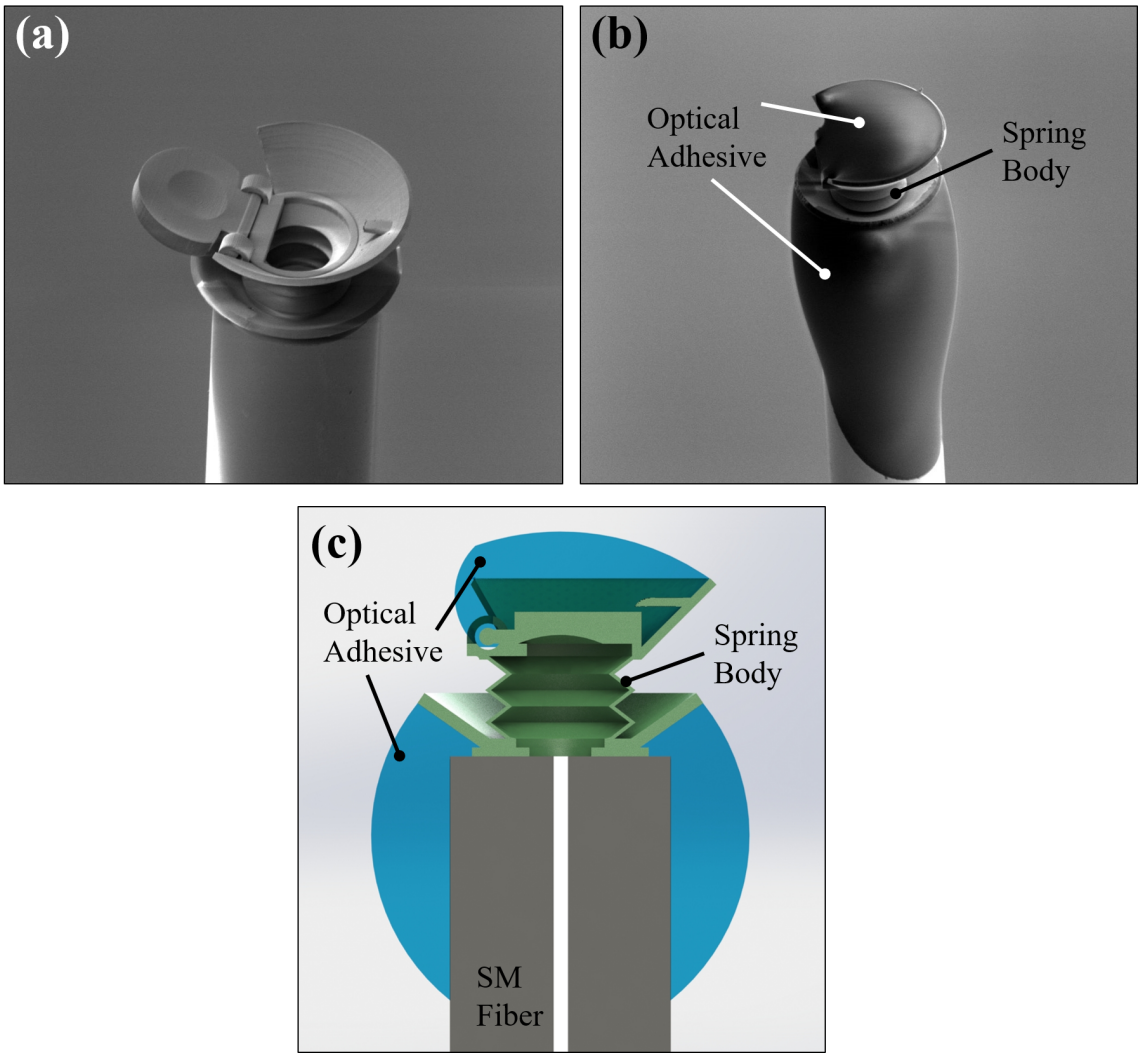

Figure 42: SEM Images of the spring-body pressure sensor. (a) Hinged mirror and cap open after metal deposition, before sealing. (b) After sealing with optical adhesive. (c) A cross-sectional rendering of the device after sealing with optical adhesive.

4.2 Methodology

4.2.1 Operating Principle

The FP cavity functions the same as with the mechanically enabled RI sensor, but instead of changing the RI of the cavity the bellows changes the cavity length by expanding in response to a pressure differential. The force acting on the spring-body will be,

$$F = \Delta P A_{top} \tag{30}$$

where only the top area will have a net effect. Pressure will be exerted on the entire wall, but its symmetry will balance the other forces. The displacement caused by this force is found with the spring equation,

$$\delta = kF \tag{31}$$

The geometry used for the spring-body is very similar to an assembly of Belleville spring washers in series. This will be used to model the potential deflection. For a single Belleville spring, the force F is related to the deflection δ by [108],

$$F = \frac{E\delta}{MR^2(1-\mu^2)}[t^3 + t(h - \frac{\delta}{2})(h - \delta)] \tag{32}$$

where R is the outer radius, E is the material's modulus of elasticity, μ is Poisson's ratio, t is the washer thickness, h is the inner washer height, and M is defined as [108],

$$M = \frac{6}{\pi ln A}\frac{(A-1)^2}{A^2} \tag{33}$$

where A is the ratio of the outer diameter to the inner diameter D/d. Most importantly, Belleville spring washers arranged top to bottom in a stack act in series. This reduces the effective spring constant and increases the deflection such that,

$$k_{eff} = [\frac{1}{k_1} + \frac{1}{k_2} + ... + \frac{1}{k_n}]^{-1} \tag{34}$$

The spring-body of the pressure sensor contains five Belleville spring washers in series, for greater deflections at lower forces. As the body expands or contracts with the

pressure differential, the reflection response of the FP cavity changes. As discussed in subsection 3.2.1, the resonant wavelength will shift with changes in the RI or cavity length. Since the spring interior is a closed environment, the pressure inside remains constant. The temperature is assumed to be constant as well, making the RI of the air inside the cavity unchanged. This makes a shift in resonant wavelength due to the expansion of the cavity, which can be calculated by equation 17, included again here,

$$\frac{\Delta\lambda_0}{\lambda_0} \approx \frac{\Delta l}{l} + \frac{\Delta n}{n} \tag{35}$$

Thus, by monitoring the change in resonant wavelength, one can determine the deflection of the bellows. The pressure differential can then be determined if the mechanical properties of the device are known.

4.2.2 Device Design

The spring-body was designed to achieve high deflection with low forces by using multiple springs in series. As shown in equation 30, the thickness of the spring-body is an important design parameter with lower thicknesses leading to greater deflection at a given force force. The spring was initially fabricated with a 4-μm thick body, but this was successfully reduced to 2-μm. The device was sturdy enough to withstand fabrication at this thickness, and greater deflection was achieved. The circular profile of the body was chosen to avoid stress concentrations that would exist at the corners of a polygon-shaped bellows. The same successful hinge and curved mirror used in the mechanically enabled RI sensor were utilized again. A small lip around the edge of the spring opening provided a resting place for the cap. A latching mechanism was added to improve stability during the sealing procedure. While the latching mechanism did not work as intended, it still aided in aligning the top mirror. There

was not enough clearance for the latch to spring back over the cap, but the latch bent down and held the cap in place by providing tension against the pin housing. A cross sectional render is presented in figure 43 that displays these design features and the multiple internal reflection that occurs inside the cavity.

A brief finite element analysis (FEA) study was performed to estimate the deflection of the spring-body and confirm the mode of operation. This was done using COMSOL® multiphysics. A simplified model of the device with the hinge and adhesive retaining features removed was used to focus on the reaction of the spring-body. Material properties of the polymerized IP-DIP were supplied by Nanoscribe and other researchers [29]. The properties used are included in table 6. The mesh and simulated deflection at -25 in-Hg are included in figure 44. The simulated deflection is greatly exaggerated for visualization. The FEA analysis confirmed the mode of deflection, but estimated higher deflections than were observed. This discrepancy is discussed

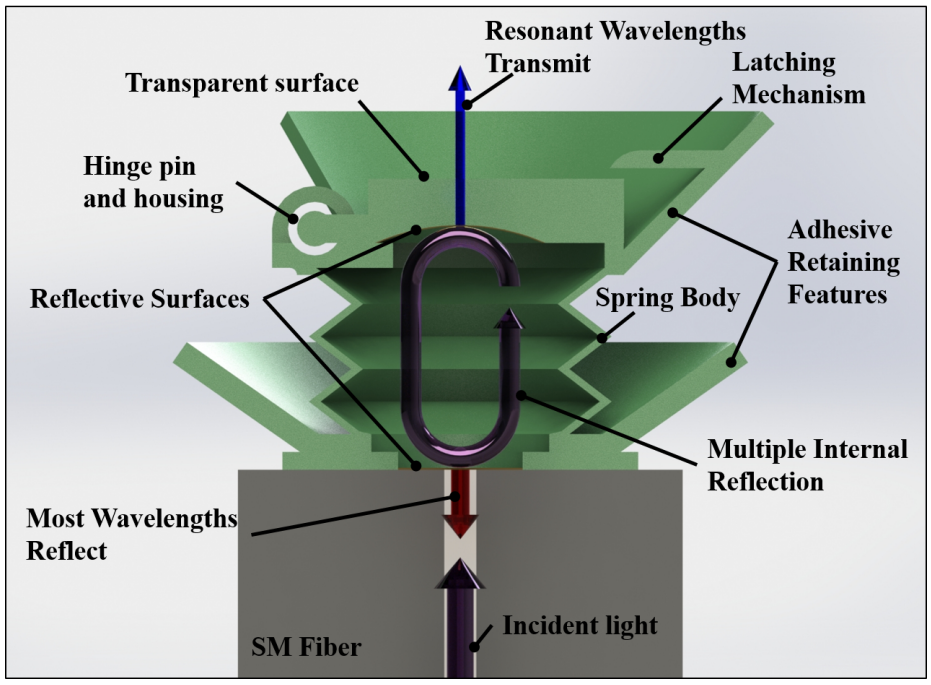

Figure 43: Cross Section view of the sensor interior picturing the spring-body and the multiple internal reflection between the two mirrored surfaces.

in section 4.3.

The device was sealed and adhered to the fiber with Norland optical adhesive 68 (NOA 68). This provided an air-tight barrier to maintain the interior pressure, and kept the device from peeling off of the fiber. Initial plans to paint the adhesive onto the rim of the cap did not work. The adhesive formed beads instead of a thin film when placed on a probe, making precise application difficult. Initial attempts covered most of the spring elements with adhesive as well as the cap. To correct this, a cup and a skirt were added to guide the adhesive around the spring elements. These features functioned as intended, and successfully sealed the device without damaging the spring elements in the body. A render of the device with the hinge in the open and closed positions is included in figuer 45. Various phases of the adhesive sealing process are included in figure 46.

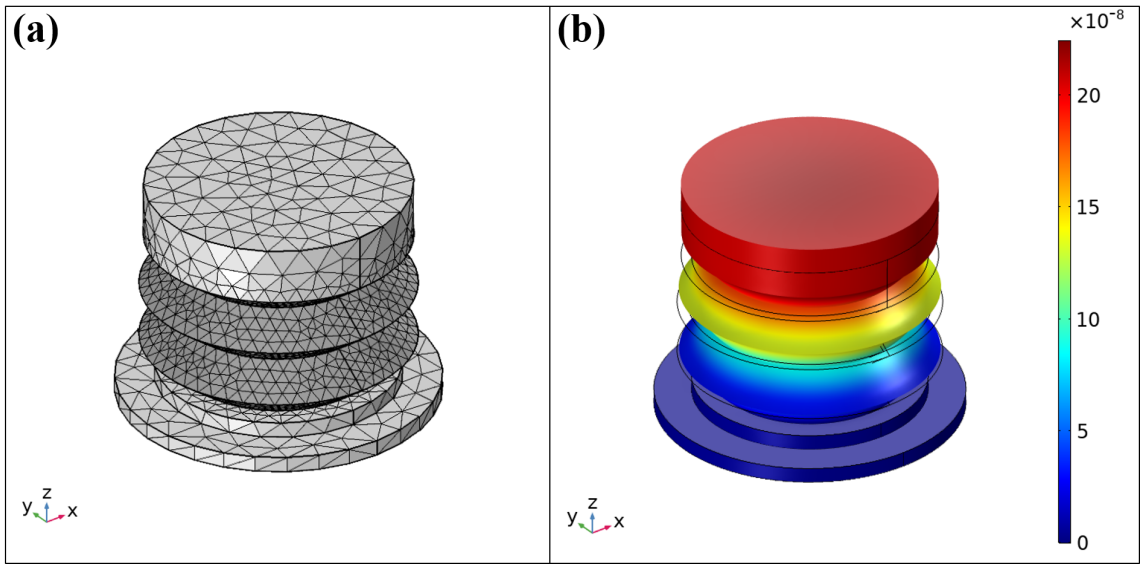

Figure 44: Model used for finite element analysis of the spring-body. (a) Generated mesh. (b) Estimated displacement in μm.

Table 6: Mechanical properties of polymerized IP-Dip used for FEA, gathered from Nanoscribe and [29].

IP-Dip Mechanical Properties for FEA		
Modulus of Elasticity	2.91	GPa
Density	1.04	g/cm^3
Poisson's Ratio	0.3	

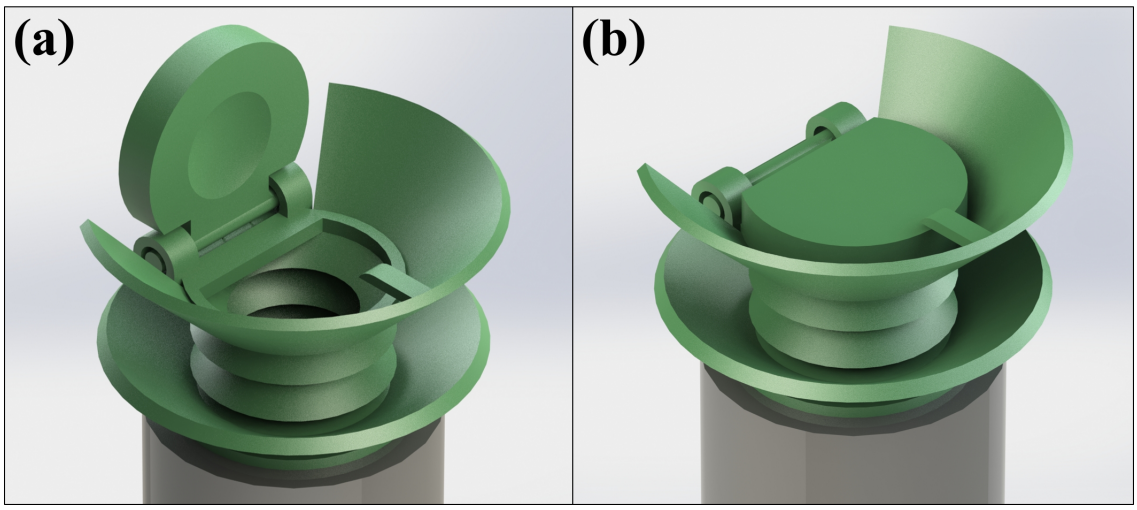

Figure 45: Computer generated render of the spring-body pressure sensor at various stages. (a) Device as fabricated. (b) Device with the top closed.

4.2.3 Fabrication

The body of the device was fabricated by 2PP microfabrication as described in 3.2.3. A slightly different Z resolution was used, and is included in table 7 with the other settings. The hinged cap was opened and closed in the same way as the RI sensor. The hinge allowed a curved mirror to be used in the cap to reduce misalignment sensitivity. The fiber face could also be exposed to receive a similar reflective coating to the top mirror. Fabricating in the open position also enabled the interior of the device to easily cleared of undeveloped photoresin. A cavity could be made full of undeveloped resin as seen in [60], but exposure to sunlight or other UV sources would start to eventually polymerize this interior. The same $5\mu m$ pad was used as in the RI sensor, giving the cavity a length of $63.66 + 5\mu m$.

Table 7: Primary 2PP Fabrication settings input to the Nanoscribe software.

2PP Fabrication Settings		
XY Resolution	0.2	μm
Z Resolution	0.3	μm
Laser Power	40	%
Scan Time	10	mm/s

Depositing a reflective coating onto the spring-body pressure sensor proved particularly challenging. The cap could be opened as with the RI sensor, but the tall walls of the spring-body significantly shaded the core during sputtering. If placed in the center of the process chamber, very little metal would be deposited on the fiber face to make the first mirror. This was corrected by moving the device to the edge of the stage, so that it passed directly under the sputtering target. With this orientation, a recipe was found that improved the reflectance of the cavity. The recipe was not fine-tuned as extensively as with the RI sensor, so only moderate improvement was achieved. Nevertheless, the reflective coating ensured that the dominant resonance features were from the internal cavity. The settings used for the deposition are included in table 8.

The pressure sensor required a unique post-processing step in applying the optical adhesive. This was done by dipping a wire-style 10-μm diameter probe into the NOA 68, then running it along a lint-free paper towel to remove the majority of the adhesive. The remaining beads were small enough to be maneuvered into the cup and skirt features without affecting the spring-body of the device. Adhesive was placed in the top cup by lowering the probe directly onto the cap of the device. The bottom was sealed by placing a drop of adhesive on the fiber and guiding it up into the skirt with the probe-tip. It then flowed around the skirt to encompass the entire bottom of the device. The gluing process is pictured in figure 46.

Table 8: Plasma sputtering deposition settings used for the spring-body pressure sensor reflective coating.

Gold in Lesker Plasma Sputtering System Cathode 1		
Cathode Power	100	Watt
Cathode Mode	DC	
Burn-in Time	30	Sec
Burn-in Pressure	10	mTorr
Deposition Time	30	Sec
Deposition Pressure	5	mTorr
Stage Rotation	5	RPM
Fiber Placement	Edge of Stage	
Fiber Orientation	Vertical	

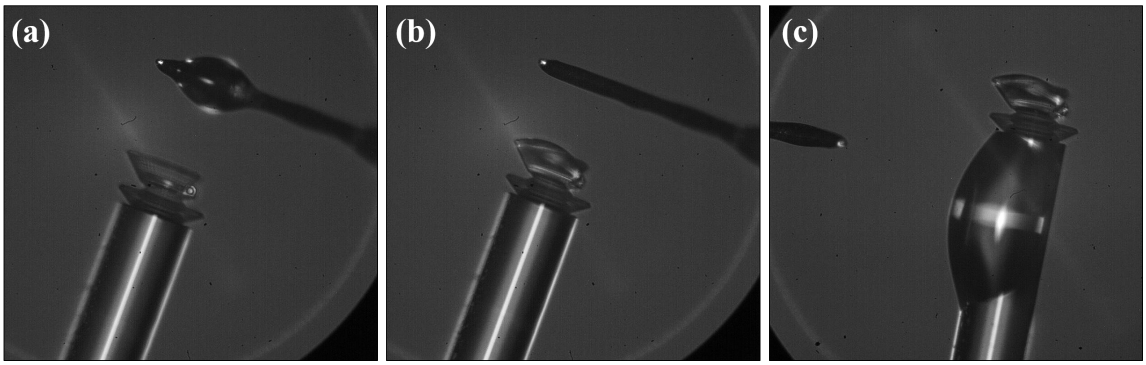

Figure 46: Optical microscope images of sealing the pressure sensor with optical adhesive. (a) Cap closed and a bead of adhesive on a probe. (b) Top sealed with adhesive. (c) Drop of adhesive on the fiber ready to be pushed onto the skirt.

4.2.4 Experiment Setup

The spring-body pressure sensor was tested with the same setup described in subsection 3.2.4, and a graphic representing the setup is included in figure 28. The vacuum inside the chamber was varied from atmospheric pressure to 16.34 kPa in increments of 16.93 kPa. The same uncertainty of two graduations (±0.68kPa) was applied to each desired pressure value. Three runs were performed, run one and run two went from atmosphere to 16.34 kPa, where run three went from 16.34 kPa to atmosphere in order to explore hysteresis effects, which did not appear to have a significant impact on results. As with the mechanically enabled RI sensor, the

motor that drives the variable-wavelength laser introduced a ringing into the reflection response. Another MATLAB® smoothing function was used to filter out the ringing and clarify the signal for analysis. Since the bellows achieved a lower reflectance than the hinged FP cavity RI sensor, the peak location was more sensitive to misplacement from the high frequency ringing. To locate the resonant wavelengths more accurately, a moving average of 50 points was used instead of the 20 points described in subsection 3.2.4. Again, the quality factor was significantly reduced, but the noise from the laser's stepper motor was suppressed, which greatly reduced the confusion as to the resonant wavelength's location. Sources of error were assumed to be the same as the RI sensor.

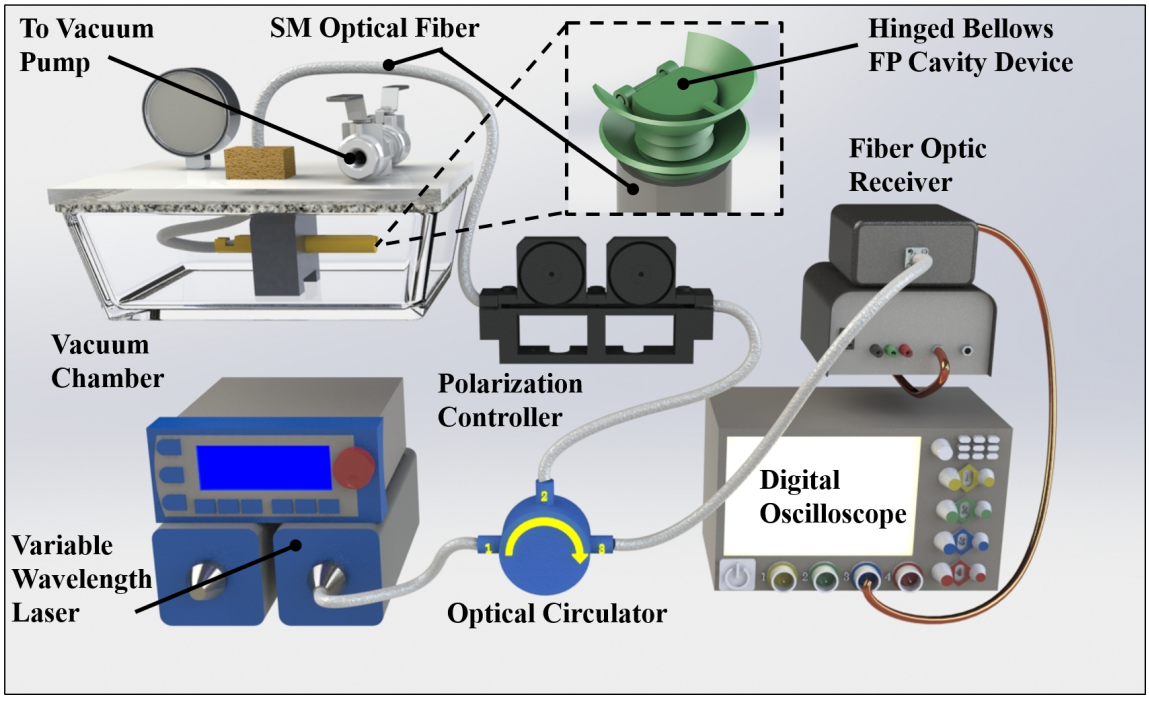

Figure 47: Test setup used to test the spring-body pressure sensor in a vacuum chamber.

4.3 Results

The spring-body pressure sensor was a successful capability demonstrator for 2PP microfabrication. The large aspect ratio spring-body and free-moving curved mirror could not be made with traditional planar microfabrication techniques. It also demonstrated a repeatable shift in resonant wavelength at different pressures. First, the reflection response of the cavity with gold was analyzed to determine the reflectance of the cavity and the quality factor of the resonant peaks. This was done with equation 21, and equation 24 as discussed in section 3.3. Both distributions were fit to the measured spectrum by normalizing the magnitude and inputting the observed resonant peak locations and free spectral range (FSR) wavelength shifts. This left only the reflectance and quality factor to be determined by fitting the respective distribution. The curve fitting application from MATLAB® was again utilized to extract values of R and Q from each model. The Airy distribution fit indicated with a 95% confidence interval that the gold coating achieved a reflectance of 17.8%±1.8%. The Lorentzian distribution fit showed, with a 95% confidence interval, a resonance quality factor of 184.3±4.8. Both of these metrics were significantly lower than achieved in the mechanically enabled FP cavity RI sensor. Unfortunately the deposition recipe was not thoroughly explored for the spring-body device in the timeline of this research, and a different recipe may be able to improve the reflection response. Specifically, several devices were lost before it was discovered they needed to be placed on the edge of the stage during deposition to overcome the shadowing of the fiber face introduced by the high aspect ratio walls. A slightly longer deposition on the edge would likely improve the response. The results of the Airy and Lorentzian fits for the portions of the reflection response evaluated are included in figure 48. The gold coating did serve to isolate the internal cavity as the primary resonator by greatly reducing interference from the top of the cap, which was un-coated polymer.

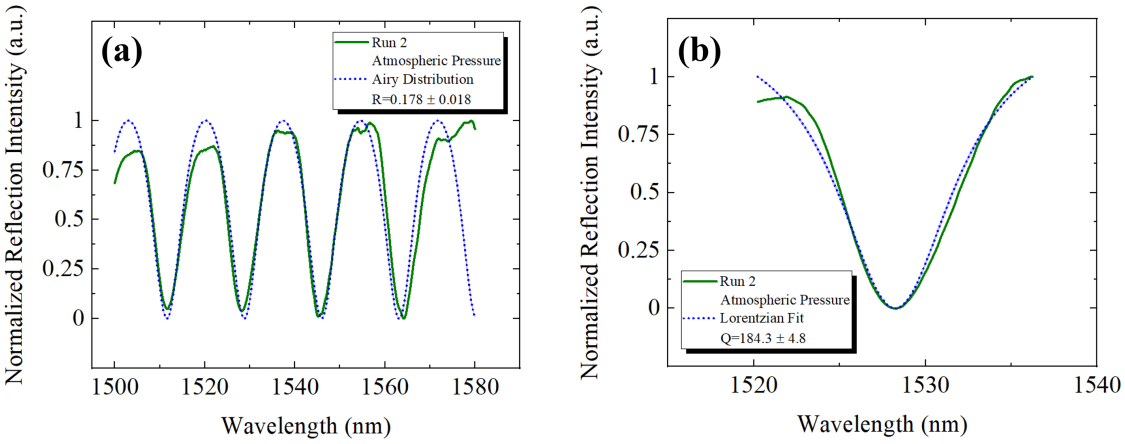

Figure 48: Analysis of the spring-body pressure sensor's reflection spectrum. (a) The Airy distribution fit to an excerpt of the response to determine reflectance. (b) The Lorentzian distribution fit to the inverse of the fourth resonant peak to determine the quality factor.

The FSR of the cavity was calculated and compared with the values predicted by equation 13. Using the measured peak locations as λ_0 and 1.0003 for the RI of air, the cavity length was extracted to align with the observed FSR results and the known length tolerance of $63.66 + 5\mu m$. This was found to be approximately 67.24 μm. This is plotted with the measured wavelength difference between peaks and included in figure 49. The vertical error bars were calculated using both instrument measurement uncertainty and the standard error of the mean from repeated measurements. The calculated FSR for the extracted cavity length can be seen to lie within the uncertainty of the measured values.

The expansion of the cavity in response to the different external pressures shifted the resonant wavelengths of the reflection spectrum as predicted by the optical and mechanical properties of the device. This was confirmed by testing a glued device against an un-glued device. The results of this confirmation experiment are included in appendix B. Since the cavity contains air at atmospheric pressure, pulling greater vacuum causes the cavity to expand. The observed red-shift follows with equation 3, which implies a longer cavity would cause resonance to occur at longer wavelengths.

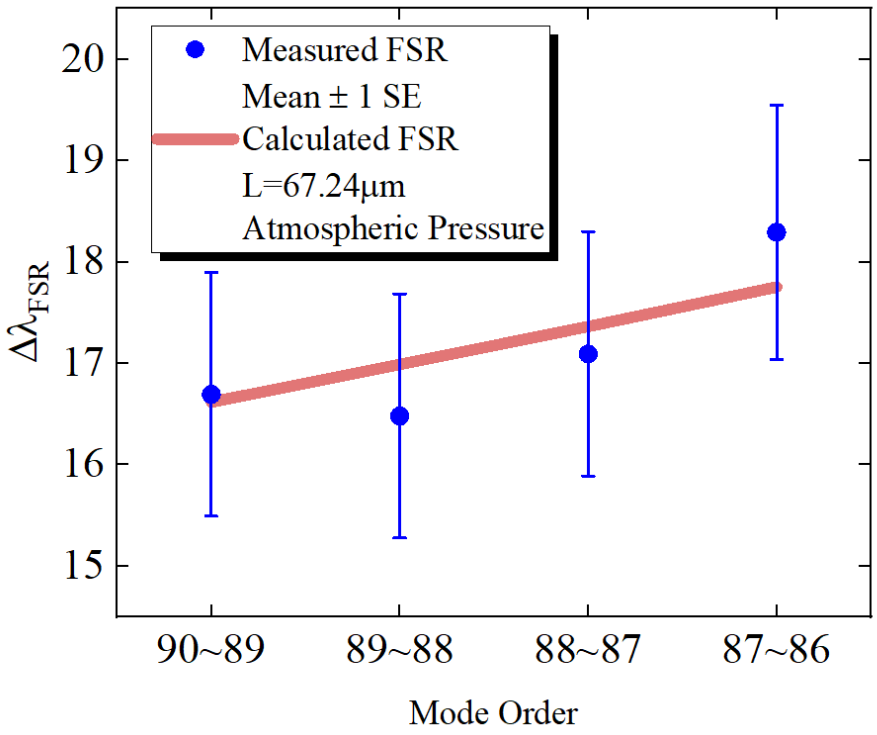

Figure 49: The measured and calculated FSR values for the spring-body pressure sensor. Error bars include both the instrument measurement error and the statistical standard error of the mean from repeated measurements.

The reflection response of the second experimental run is included in figure 50, with the third resonant wavelength highlighted. The location of this resonance at a given vacuum pressure, as found with MATLAB®, is plotted in figure 51. The response of the device was linear, but suffered from some variation between experimental runs and was limited by the accuracy of the measurement technique. Some variation could be caused by creep within the spring-body after repeated expansion, or slight variations in the vacuum level between runs. As discussed in subsection 3.2.4, there was a slight leak somewhere in the pressure setup that was compensated manually by opening the valve to the vacuum at the desired level.

The vertical error bars on the measured values include both the instrument measurement error and the 1 standard error of the mean calculated from the repeated

measurements. The uncertainty of the vacuum level was too small to appear on this scale. The uncertainty introduced by the measurement technique, particularly the MATLAB® filters. As with the RI sensor, fitting an appropriate distribution to locate the peak wavelength could reduce this uncertainty in future work and improve the accuracy of the sensor.

A linear model was fit to the results, and is pictured in figure 51. The confidence intervals were calculated from the repeated measurements. The resonant wavelength at a given pressure was fit to be,

$$\lambda_0 = (-0.027 \pm 0.0023)_{[\frac{nm}{kPa}]}P + (1514 \pm 0.15)_{[nm]}. \tag{36}$$

The deflection predicted by the finite element analysis (FEA) simulation was approximately three times larger than the deflection calculated by the linear model. The values of each are included in table 9, with the 95% prediction band calculated from the repeated measurements included on the values from the lineaer fit. Factors that likely contribute to the FEA's lack of agreement are: different material properties in the actual device and different geometric considerations caused by the adhesive, par-

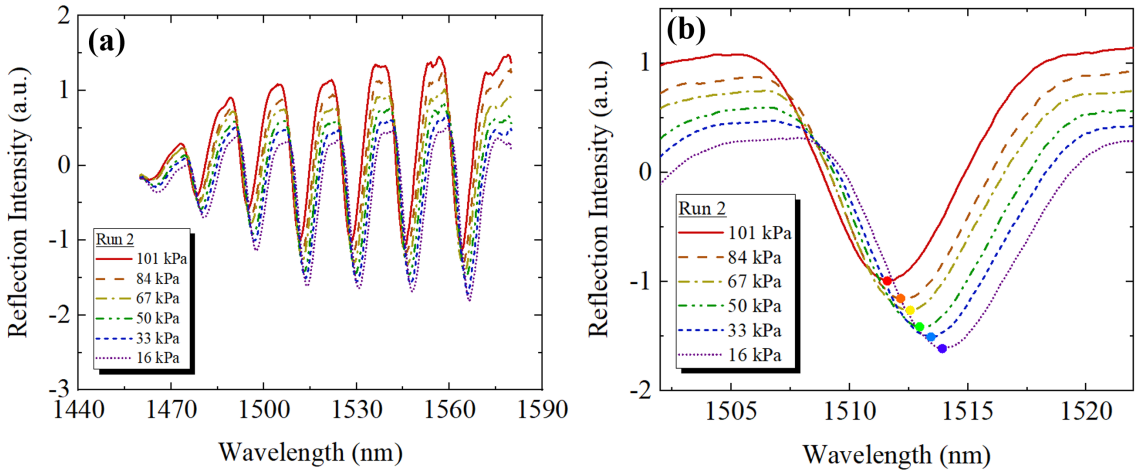

Figure 50: Reflection spectrum from the second run of the pressure series. (a) The entire spectrum. (b) The third resonance peak.

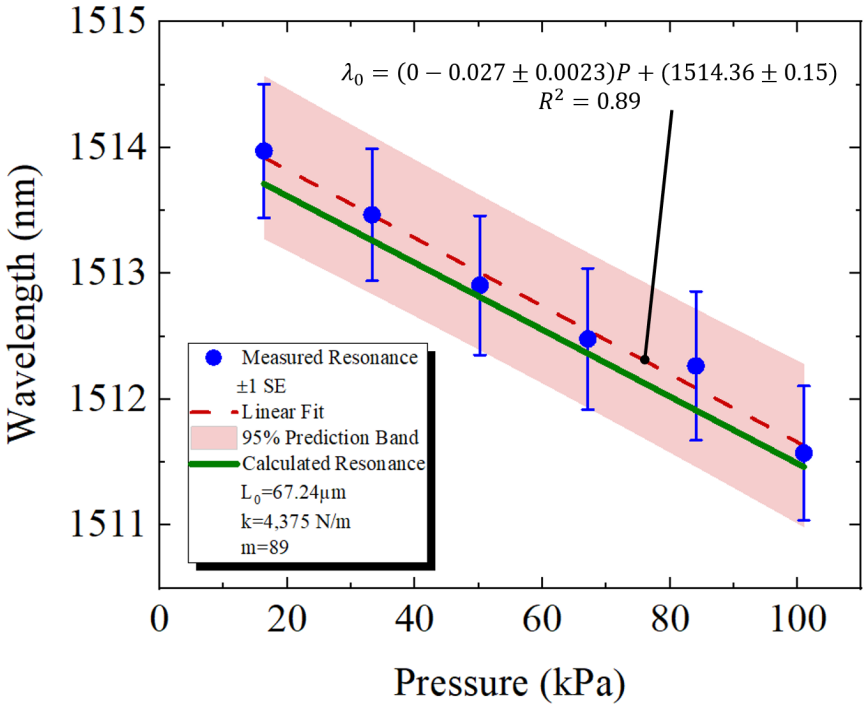

Figure 51: Shifting location of the third resonant peak at different pressures. The calculated resonance values use an initial cavity length and mode order extracted from the measured values and equation 3. The vertical error bars include 1 standard error from the repeated measurements and the instrument measurement uncertainty described in subsection 3.2.4. The horizontal error bars from the uncertainty of the vacuum level was too small to be viewed on this scale. The linear fit and its prediction band were calculated from the repeated measurements only.

ticularly on top of the spring body. The mechanical properties of polymerized IP-Dip have been shown to vary significantly with the laser power and scan time used during fabrication [29], and this could play a significant role in altering the deflection. While these devices were fabricated using the recommended settings, they were exposed to additional UV to cure the adhesive, adding another potential change to material properties. The adhesive itself was also a significant feature that was not included in the model. The weight of the hinge, cup, and adhesive would tend to compress the spring-body and work against the expansion of the cavity. Despite being lower than anticipated, it is worth noting that the bellows deflection produced a resonance shift significantly greater than the RI change due to pressure observed in the mechanically

enabled FP cavity RI sensor.

Table 9: Spring-body deflection predicted by the FEA simulation and the linear model fit to the measured results. The 95% confidence interval was established using repeated measurements.

Pressure		FEA		Linear Model	
-5	in-Hg	0.056	μm	0.017±0.062	μm
-10	in-Hg	0.112	μm	0.035±0.062	μm
-15	in-Hg	0.168	μm	0.052±0.062	μm
-20	in-Hg	0.225	μm	0.069±0.062	μm
-25	in-Hg	0.281	μm	0.087±0.062	μm

To determine the expansion that actually occured, equation 3 was used to extract the Δl that aligned with the measured results. The force caused by the pressure differential was determined with equation 30 and combined with the extracted deflection into equation 31 to determine the observed stiffness of the spring-body. This is why the slope of the calculated resonant peaks in figure 51 matches the linear fit, because it was extracted by matching the observed change in cavity length. The results regarding the reflection spectrum and pressure measurements of the spring-body pressure sensor are compiled in table 10.

Table 10: Spring-body pressure sensor results.

FSR	17.18 ± 1.04nm
Reflectance	17.8%±1.8%
Quality Factor	184.3±4.8
Press. Sensitivity (Linear Fit)	0.027±0.0023 nm/kPa
Total Observed Shift from Press.	2.4 ±1.06 nm/84.66 ±1.35 kPa
Smallest ΔP Measured	16.93±1.36kPa

4.4 Conclusion

The spring-body FP cavity pressure sensor successfully measured pressure changes by altering its resonant frequency. The stiffness of the spring-body was extracted from

the observed resonant wavelength shift, and could easily by modified by changing geometry of the spring. This exemplifies the 3D freedom capabilities of 2PP microfabrication over planar fabrication techniques. A reflective coating was achieved despite the high aspect ratio, 360 degree side-walls, to utilize a curved mirror for improved alignment insensitivity and isolate a single resonator from interference with top third wall. Adhesive retaining features were successfully implemented to precisely guide UV curable optical adhesive at the micron scale. A linear shift in the resonant wavelength within the same order of magnitude as a COMSOL® FEA simulation was observed. Deviation from the model was likely caused by different material properties altered during fabrication and curing, and an incomplete model that ignored the weight of the optical adhesive. A linear model fit to the data indicated a red shift of the resonance feature by 0.027 ± 0.0023 nm/kPa. The deflection mechanism also produced a 169% greater shift in resonant wavelength than observed in the FP cavity RI sensor, making it more sensitive to smaller pressure changes. The resolution was limited by the poor quality factor and measurement uncertainty. This could easily be improved by further refining the reflective coating deposition recipe and fitting an appropriate distribution to locate the resonant wavelength. Overall, this proof-of-concept spring-body pressure sensor presented a functional pressure sensor while exploring advanced 3D features made with 2PP microfabrication.

Future work to improve the spring-body pressure sensor could include:

- Perform more robust finite element analysis to optimize the spring-body geometry and allowable wall thickness.

- Further test the device at higher vacuums, positive pressures, and finer steps to explore the hysteresis, operational range, fatigue effects, and maximum resolution of the device.

- Explore the spring-body's response to high frequency, acoustic signals for use as a micro-microphone.
- Optimize the reflective coating through adjusting the recipe or exploring new materials to further improve the quality factor of the reflection response.

V. Micro-Anemometer Flow Sensor

5.1 Chapter Overview

This chapter describes a micro-anemometer flow sensor constructed onto the cleaved end of a low loss optical fiber by two-photon polymerization (2PP) micro-fabrication. A dynamic structure was created featuring a rotor moving around a stator powered by axial fluid flow impinging on three cup-like blades. The bottom of each blade is a flat mirror featuring a high reflective gold coating that is parallel to the fiber face. As the rotor spins, these mirrors pass over the center of the fiber. Light is input to the fiber, and reflected back down the core when the blades pass over it. These reflections are counted to determine the velocity of the incident flow, and with the dimensions of the nozzle, the mass flow rate. This chapter discusses the design of the device, the experiment used to evaluate the device, the results of this experiment, and concluding remarks with possible future work. A scanning electron microscope (SEM) image of the flow sensor used in this work is included in figure 52.

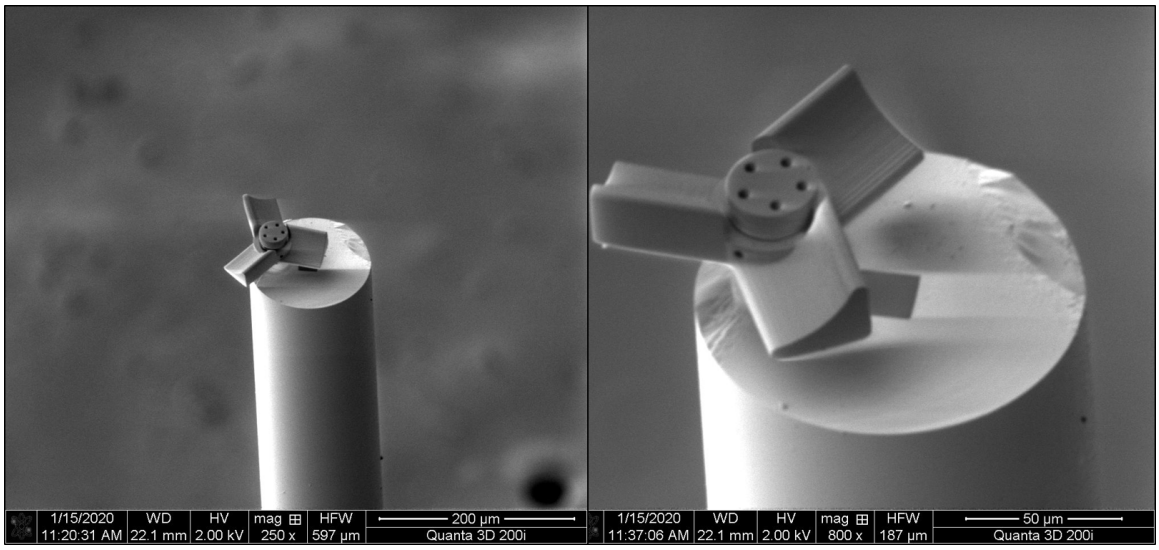

Figure 52: SEM images of the final flow sensor.

5.2 Methodology

5.2.1 Operating Principle

The flow sensor was designed to rotate in response to incident flow impinging on the curved blades to create a reaction force with a component perpendicular to the flow capable of producing torque around the stator. The aerodynamic forces acting on each blade in this scenario are pictured in figure 53. The incident flow in this work was directed out of a nozzle as described further in subsection 5.2.4. The velocity of the flow exiting the nozzle can be calculated with,

$$v = \frac{A}{\dot{V}} \tag{37}$$

where $\dot{V}$ is the mass flow rate and A is the area of the nozzle aperture. The device was placed approximately $4mm$ away from the nozzle and aligned along the center axis of the orifice. This analysis assumes the drop in velocity of the air while traveling to the device is negligible because the device is located relatively close to the nozzle. The flow is also considered to be in-compressible, because it has a Mach number less than 0.3, a common cutoff critera for compressible flow [109]. The largest Mach number, the ratio of the flow to the speed of sound in the fluid, for this experiment was,

$$M = \frac{v}{c} \tag{38}$$

$$c = \sqrt{\gamma RT} \tag{39}$$

Where v is the velocity of the flow, calculated to be $52.63m/s$ for a flow of 25LPM and equation 37, γ is the ratio of a gas's heat capacity at constant pressure, C_p, to its heat capacity at constant volume, C_V, which is 1.4 for nitrogen, R is the specific

gas constant, $296.8 Jkg^{-1}K^{-1}$ for nitrogen. The largest Mach number experienced is then,

$$M = \frac{v}{c} = \frac{A/\dot{V}}{\sqrt{\gamma RT}} = \frac{52.63[m/s]}{353.07[m/s]} = 0.15. \tag{40}$$

Assuming in-compressible flow greatly simplifies the aerodynamic situation at the blades. The dynamic pressure exerted by the flow can then be estimated with,

$$P_{fl} = \frac{\rho v^2}{2} \tag{41}$$

where ρ is the density of the flow and v is the velocity of the flow. The shape of the blade, as seen in figure 53, causes a reaction force with both an axial and a perpendicular component. The perpendicular, driving force would be,

$$F_{fl} = P_{fl} A_{top} cos(\theta) \tag{42}$$

and the axial component would be,

$$F_{ax} = P_{fl} A_{top} sin(\theta). \tag{43}$$

After accelerating to a given velocity, the sum of moments action on the rotor is zero. The moments acting on the rotor at steady state are: the perpendicular component of the flow pressure, the drag on each rotating blade, and the friction between the rotor and the stator. The drag force on each blade is,

$$F_{dr} = C_d A_{front} \frac{\rho v_{rot}^2}{2} \tag{44}$$

where C_d is the drag coefficient determined by the cross-sectional shape of the blade, v_{rot} is the instantaneous velocity of the blade, and ρ is the density of the flow gas. The

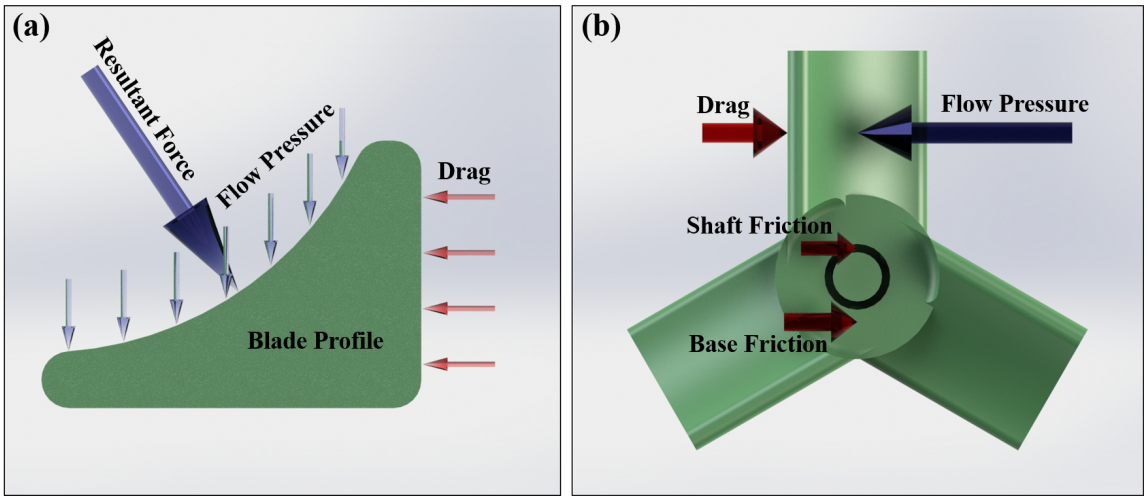

Figure 53: Graphical representation of the flow sensor dynamics. (a) Aerodynamic forces acting on each blade. (b) Moments action on the rotor, only the forces of one blade are pictured.

friction is caused by both the central shaft and contact with the hemisphere features on the flat base of the stator. Assuming the same coefficient of dynamic friction μ_k, and the weight of the device is small compared to the flow pressure, the friction force acting on the rotor would be,

$$F_{fr} = \mu_k(F_{fl} + F_{ax}) = \mu_k P_{fl} A_{top}(sin(\theta) + cos(\theta)) \tag{45}$$

The aerodynamic forces and the moments acting on the device are pictured in figure 53. The sum of moments is,

$$\sum M = M_{fl} - M_{fr} - M_{dr} = 0 \tag{46}$$

The moment arms and corresponding forces acting on a blade can be seen in figure 53 as the distance of each force from the center of the device. Adding moment arms and combining equations 42, 44, and 45 with equation 46 yields,

$$PA_{top}cos\theta l_1 = \mu_k(F_{fl} + F_{ax}) = \mu_k P_{fl} A_{top}(sin(\theta)l_2 + cos(\theta)l_3) + C_d A_{front}\frac{\rho v_{rot}^2}{2} l_1 \quad (47)$$

Equation 47 shows the relationship between the rotational velocity and the incident flow pressure, which is driven by the flow rate. Unfortunately the experimental results, discussed in section 5.3, were significantly different than the ideal calculations derived from equation 47. Errors in the drag and friction coefficients likely contributed, but the interaction of the fiber in the flow field likely had the greatest effect. The rotor was suspended only $25\mu m$ above the flat face of the fiber, which was also perpendicular to the flow. The turbulence caused by the abrupt stop of the flow at the fiber undoubtedly kicked back into the blades to contribute to the instability and variability of the results. This was a complicated microfluidic situation that could be modelled with computation fluid dynamics (CFD) to better understand the effects on the spin of the rotor. The effects of the fiber could also be reduced by re-designing the blades to operate in response to lateral flow. Both of these topics were beyond the scope of this research to produce a technology demonstrator, but would make for informative future work.

5.2.2 Device Design

The first iterations of the flow sensor attempted to utilize lifting airfoils at a low angle of attack to drive the rotor. A rendering of this early design is included in figure 54. Initial testing showed this mechanism to be ineffective. This was most likely due to the short length of the wings. To visualize these different mechanisms, consider a propeller-driven airplane. The wings are oriented toward the flow of the air around the plane, and produce lift roughly orthogonal to this flow, but they are long compared to the body of the plane. The propeller blades produce thrust

perpendicular to their direction of travel as they spin with the motor, and they are significantly shorter than the wings and body of the plane. This arrangement inspired the next design iteration of the flow sensor, cup-like blades to produce rotation from incident flow. Similar arrangements can be seen in vane anemometers, American farm-style windmills, industrial fans, and even simple pinwheels.

Once the orientation of the blades was determined, a clear on-off condition was needed. In early designs, a flat brick was included to provide a mirror. This was abandoned in intermediate designs for using the blades themselves as mirrors because the bricks reduced aerodynamic performance and made spinning more unbalanced. Traditional, thin, angled blades were attempted, but they did not provide a clear reflection while passing over the core. A flat bottom was used on the blades to reflect more light down the core as they passed over it.

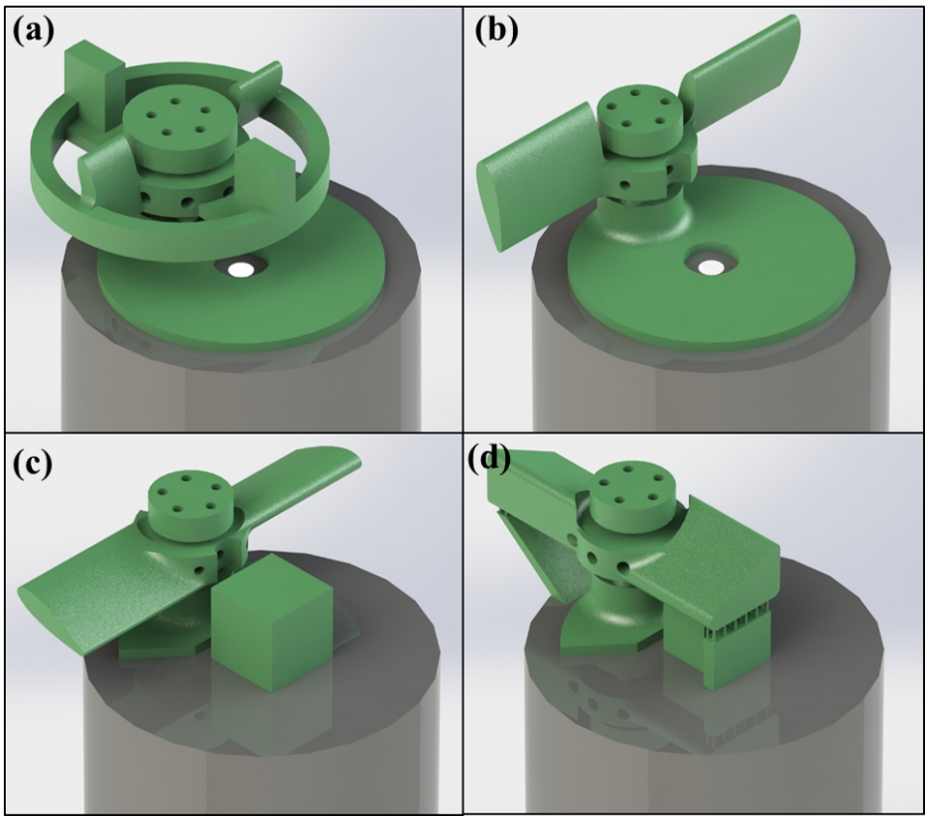

Figure 54: Previous iterations of the micro flow sensor.

The retaining ring used in early designs was abandoned when the length of the blades was extended. The ring began to fail during fabrication, and was no longer needed to support the sturdier blade designs. The top of the flat-bottomed blades was originally flat as well. The curve was added to increase the surface area in contact with the incident flow, A_{top} in equation 47, thus increasing the driving force. This proved to be the most successful blade shape of this work.

A third blade was added to also improve the driving force. The polymerized photoresin is very light, so the increase in friction was negligible compared to the 50% increase in top area. The front area was also significantly smaller than the top area, so the increase in drag would be less than the increase in driving force. Only three blades were used as too many blades could make it difficult to identify individual passes over the core. Each additional blade also added to the complexity of fabrication because it needed to be supported.

The longer blades used in later designs experienced delamination failures during fabrication. The furthest unsupported portions of the blades appeared tapered upwards after developing. The initial polymerized layers were sinking through the resin during the laser scan, and washing away during development. This altered the angle of the bottom mirror and changed the profile of the top, reducing both the signal and aerodynamic performance of the device. The delamination was stopped by supporting the tips of each blade with break-away structures rooted to the face of the fiber. The geometry that was chosen consists of a 10-μm thick extrusion topped with two rows of 10-μm tall 1-μm diameter pillars. These structures were removed with a semiconductor analysis probe after development, releasing the properly shaped rotor. The removal of the supports took approximately 20 minutes, and required similar manual dexterity to precise wirebonding.

The center of the rotor was also supported above the stator by three, 1-μm pillars.

These broke away when the rotor was initially spun by a probe. Three hemispheric protrusions were fabricated on the base of the stator to reduce friction with the rotor. The stability of the device's spinning was improved by reducing the clearance between the rotor and stator from $4\mu m$ to $2\mu m$. Holes were added in the rotor and the top of the stator to allow the developer access to the small clearances around the center shaft.

A masking brick was added to cover the core during metal deposition. It was a successful masking technique, allowing light to exit and enter the fiber unimpeded by the reflective coating covering the rest of the device. Gold was deposited by plasma sputtering to make the reflective coating. A highly reflective surface was desired on the blades, and the with the core entirely masked, a relatively thick coating was used. The settings for the deposition are included in table 11. These settings deposited 60 nm onto a silicon wafer. The flow sensor was placed in the process chamber such that the blades were orthogonal to the sputtering target. The exact deposition thickness on this 90° surface is unknown, but examination with an SEM and optical microscope showed a complete coating of the device.

5.2.3 Fabrication

The 2PP microfabrication was performed as described in subsection 4.2.3 with the same Nanoscribe settings. Two additional steps were performed: removing the support material and sputtering the reflective coating. The support material was removed by mounting the fiber into a Newport FPH-S side loading fiber chuck, which was loaded into a Newport 561-FC fiber chuck holder. This stainless steel block was placed under a Micromanipulator probe station. A Jmicro Technology KRN-09S magnetic probe arm was used with a Pacific Instruments ST-1 0.1-μm diameter semiconductor analysis probe to remove the support material. Ideally, the 1-μm

diameter pillars were peeled off of the blade before disconnecting the base of the support. The side-blade supports were removed before the blade over the core. Once all of the supports were removed, the probe was used to spin the rotor and break the inner support pillars.

The reflective coating was deposited with a Kurt J. Lesker company magnetron plasma sputtering system. The deposition settings used are included in table 11. The fiber was oriented perpendicular to the sputtering target, placing the bottoms of the blades at a 90° angle. After sputtering, the masking brick was removed with the 0.1-μm diameter probe. This was best accomplished pushing high on the brick with the very tip of the probe to peel it off of the fiber. After this, the flow sensor was ready to test.

After being tested in its original state, a lubricant was applied to produce more

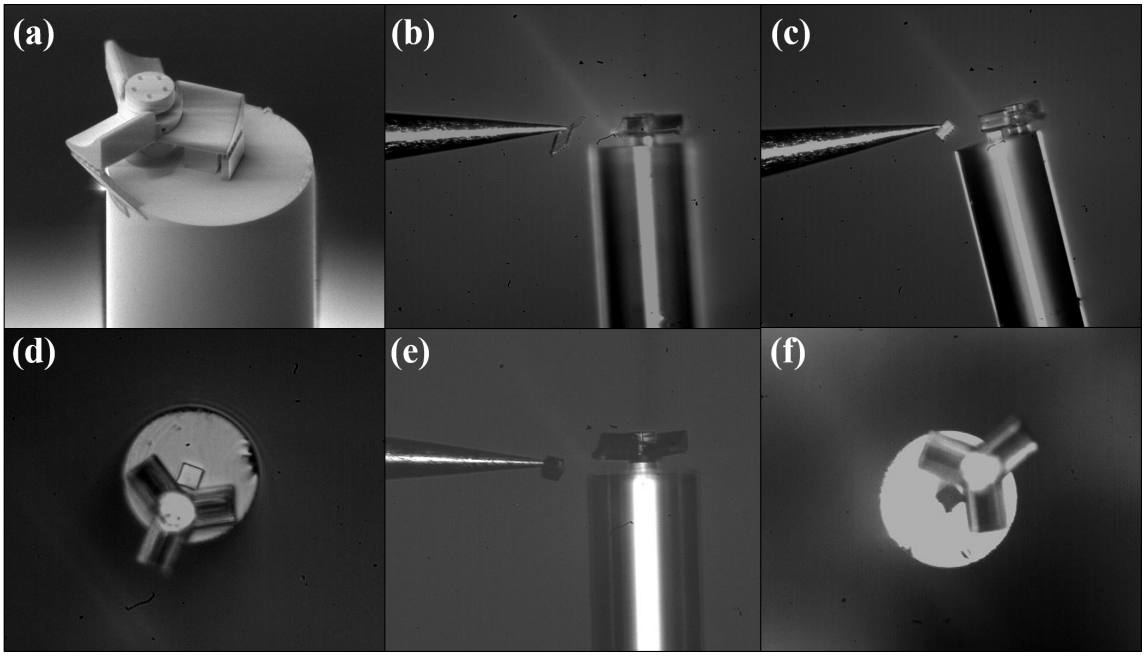

Figure 55: Flow sensor assembly process. (a) SEM image of the as-fabricated device. (b) An angled support being removed with a probe. (c) The vertical support being removed by a probe. (d) Top view of the device after sputtering. (e) Masking cap being removed by a probe. (f) Top view of the device after the masking cap has been removed, showing the core not coated with gold.

Table 11: Plasma sputtering deposition settings used for the flow sensor reflective coating.

Gold in Lesker Plasma Sputtering System Cathode 1		
Cathode Power	100	Watt
Cathode Mode	DC	
Burn-in Time	30	Sec
Burn-in Pressure	10	mTorr
Deposition Time	300	Sec
Deposition Pressure	5	mTorr
Stage Rotation	5	RPM
Fiber Placement	Center Stage	
Fiber Orientation	Horizontal	

consistent rotation. The common 3-IN-ONE all purpose silicone-oil was used. It was applied by beading it onto a 10-μm diameter wire style probe as described in subsection 4.2.3. The initial application covered one blade and most of the rotor, but was dried off with Nitrogen. The oil remained only in the area between the rotor and the stator that was blocked during blow-drying.

5.2.4 Experiment Setup

The flow sensor was tested using the AFIT house nitrogen supply. The sensor fiber was loaded into a Newport FPH-S side loading fiber chuck with about 1-2mm protruding from the end. This was mounted into a Newport UPA-FC 1" fiber chuck adapter, ensuring the set screw was aligned to press down on the slide of the fiber chuck, securing the fiber further. The adapter was fixed into a Thorlabs KM100 kinematic mirror mount. The mirror mount was used to align the device perpendicular to the flow nozzle. The small end of a Swagelock 1/8" to 1/4" compression fitting reducer was used as a nozzle. This was mounted into a 3D printed frame and positioned onto a 1" pitch optical breadboard with the mirror mount. The flow was controlled with a Brooks Instrument Sho-Rate flow meter calibrated to inert gasses, including Nitrogen. The reported accuracy of the flow sensor was $\pm 5\%$ of the full

scale, or ±1.21 LPM of Nitrogen. The reported repeatabilty of the flow meter was ±0.25% of the full scale, or ±61 sccm for Nitrogen.

A Sacher Lasertecnik TEC-520 laser and Pilot PZ 500 laser controller set at 1550 nm was used as the light source. This was fed into port one of a Thorlabs 6015-3-APC non-polarization maintaining optical circulator designed to operate from 1525-1610 nm. A Thorlabs FPC025 two-paddle manual polarization controller was connected to port two of the optical circulator. Adding the polarization improved the quality of other test as discussed in sections 3.2.4 and 4.2.4, so it was included for the flow sensor test. The polarization was maintained throughout all of the flow tests, with both paddles oriented vertically. The sensor fiber was connected to the other end of the polarization controller, and thus port two of the optical circulator. The sensor fiber was spliced to a Fiber Instrument Sales simplex 9/125 FC/APC patch cable with a 3M Fibrlok II universal fiber splice. The third port of the optical circulator was connected to a Newport model 1611 1-GHz low noise photoreceiver. The DC output of the photoreciever was read by a Agilent 54641D mixed signal oscilloscope. This experiment setup is pictured in figure 56.

A test was initiated by opening the flow controller, and raising the flow to the desired level. The flowmeter directly measures the height of the ball in millimeters, which must be translated to a flow based on the gas being used. The flow was varied from 60 - 150 mm, corresponding to (10.97 - 24.28) ±1.21 LPM of Nitrogen. Readings were taken at 60, 70, 90, 110, 130, and 150 mm. The static friction of the device was higher than the dynamic friction, so it was often necessary to increase flow above a desired reading to "kick start" the device. Once spinning, the flow was lowered to the desired value. Device motion was monitored with an optical microscope also mounted on the breadboard. As previously discussed, the spinning of the device was too erratic to create an observable frequency due to the rotor sticking to the stator

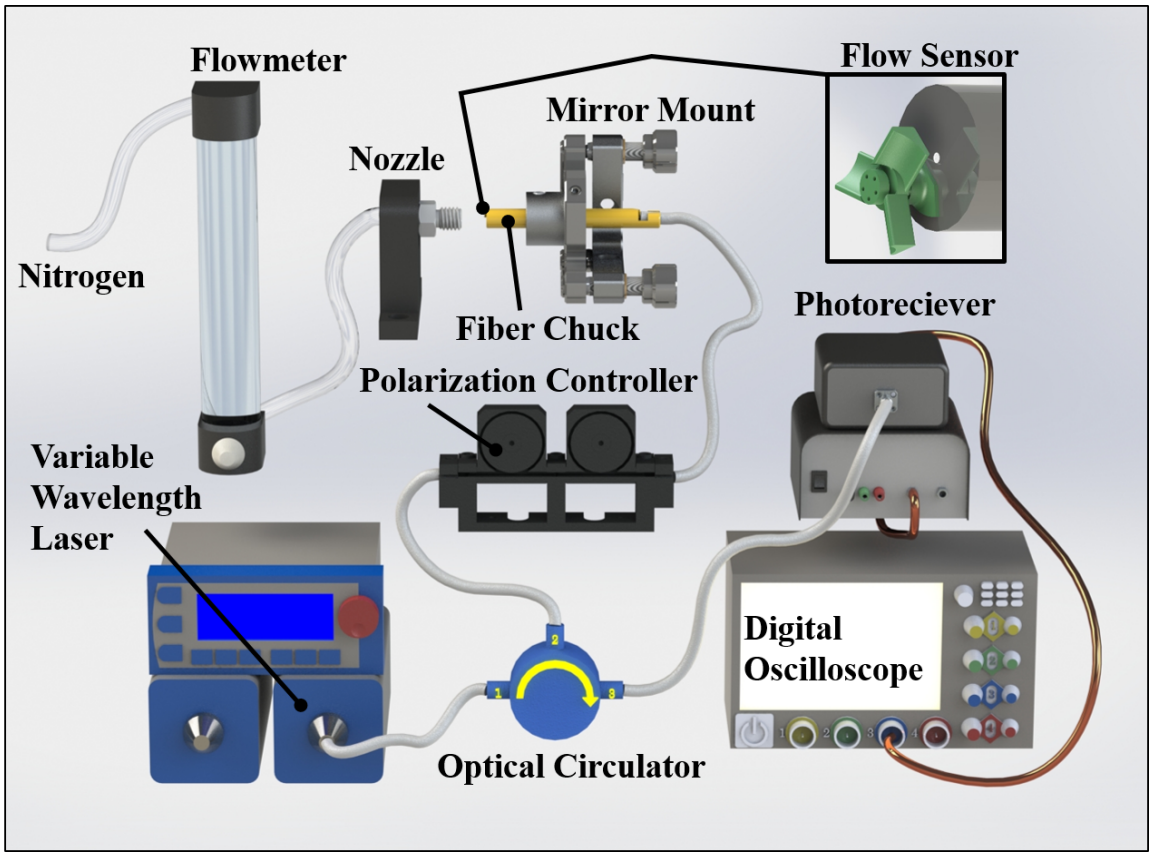

Figure 56: Experimental setup used to test the flow sensor.

and high turbulence at the fiber face flowing up into the blades. This inconsistency was also observed with a high speed camera. Changes in flow could still be measured, but by counting the number of reflection events over a small time period instead of monitoring a constant frequency. The oscilloscope measured 1 sec of spinning for each test.

MATLAB® was used to count the peaks over each reading. Counting criteria including minimum peak width, minimum peak prominence, and minimum peak distance were chosen by observing a small segment of the output signal for each flow rate. The parameters for the peak finding algorithm were varied and judged qualitatively to determine a criteria that counted the majority of the reflection events once. The same counting method was applied to each measurement. An excerpt of this count-

ing criteria and the raw reflection data from a test is included in figure 57. Future work could further refine the algorithm or evaluate a different numerical method to improve the peak counting accuracy. Each flow rate was tested three times, with the test order randomized by Microsoft Excel. These results are plotted in figure 58 and discussed in section 5.3. A small-adjustment experiment was also performed from a float height of 70 - 75 mm, (10.97 - 11.95)±1.21 LPM, to determine if the device could match the finest resolution of the flow meter. These results are included in figure 59, and discussed in section 5.3.

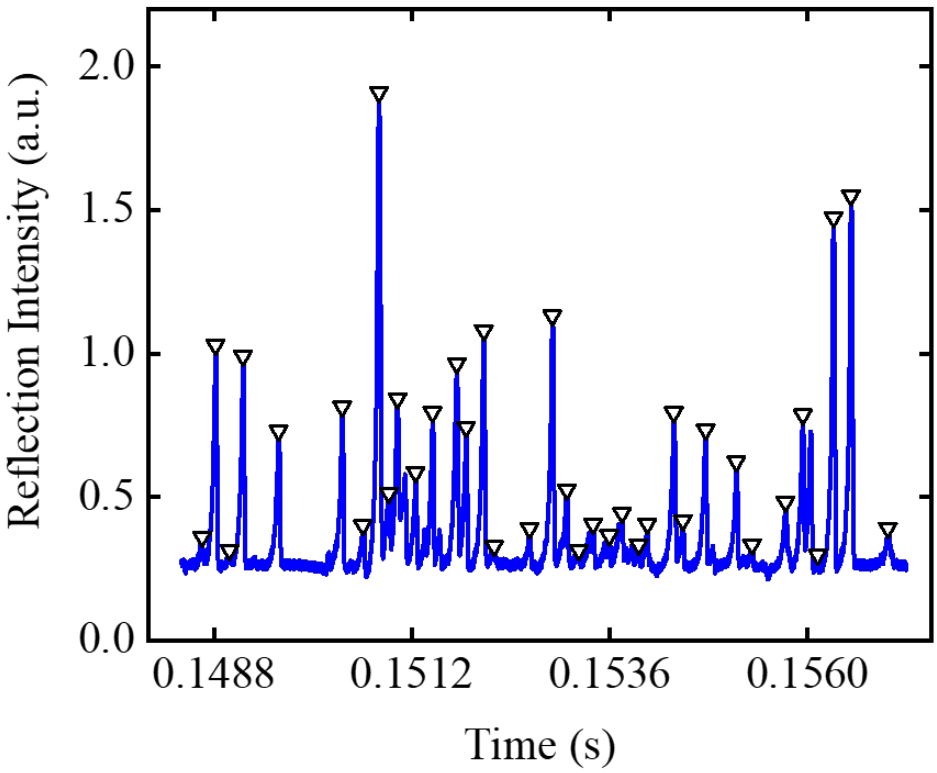

Figure 57: Excerpt of MATLAB® peak counting results.

5.3 Results

The flow sensor successfully demonstrated increased rotational velocity in response to increases in flow rate. While the experimental results did not correspond well to the theoretical results quantitatively, the qualitative response matches the aerodynamic and frictional forces at work.

There was significant variation within the repeated measurement at lower rates, with greater variability until 17.55±1.21LPM, corresponding to a speed of 36.94±2.55m/s. This is most likely due to either the rotor reaching its maximum speed, where stronger flow rate no longer overcame the drag, friction, and back-flow from the fiber face, or a limit in the peak counting algorithm. Visually examining excerpts of the high flow rates after applying the counting algorithm indicated that all the notable peaks were being detected, so the rotor had liklely reached its maximum velocity. A dynamic algorithm with different settings for each measurement could eliminate this possibility, but was not examined in this work. The tighter grouping at higher speeds is likely caused by the increased stability. At lower flows the rotor tended to stick to the stator for short periods, causing variations in the spin speed. At higher flows the greater force would overcome more of these sticking events and increase the consistency of the rotation.

The coarse flow test indicates that the maximum operating flow for this device and measurement method in Nitrogen is around 22.58±1.21 LPM (47.54±2.55 m/s). At this point, the greater flow did not increase rotational velocity. At higher flows, both the turbulence and the back-flow from the fiber face increased as well, dramatically altering the fluid dynamic situation. If ever used beyond a technology demonstrator, an in-depth calibration would be required to understand the expected reading and confidence interval of any given device. The results of the course flow test are included in figure 58. The vertical error bars represent 1 standard deviation of the repeated

measurements. The repeatability of the flow meter was included with horizontal error bars, but is too small to be seen on this scale. Parts of the lower-flow regime did present a linear trend, which was explored in the next experiment.

A fine flow test was performed at the resolution limit of the flow meter in a linear region of the response curve from (10.97 - 11.79)±1.21 LPM. The indicator was raised 1mm at a time, the smallest graduation on the flow meter, which corresponded to a change in flow rate of 0.165 LPM (165 sccm, 0.347m/s). The repeatablity of any measurement was reported to be ±0.25% of the full scale, or ±61sccm (±0.128m/s). A linear model was fit to the repeated measurements of the experiment which produced an R-squared value of 0.904 and a p-value of 5.7×10^{-16}, strongly rejecting the null hypothesis. Each setting does contain significant variation, again likely caused by the instability of the rotation. The linear fit produced the following relationship over this

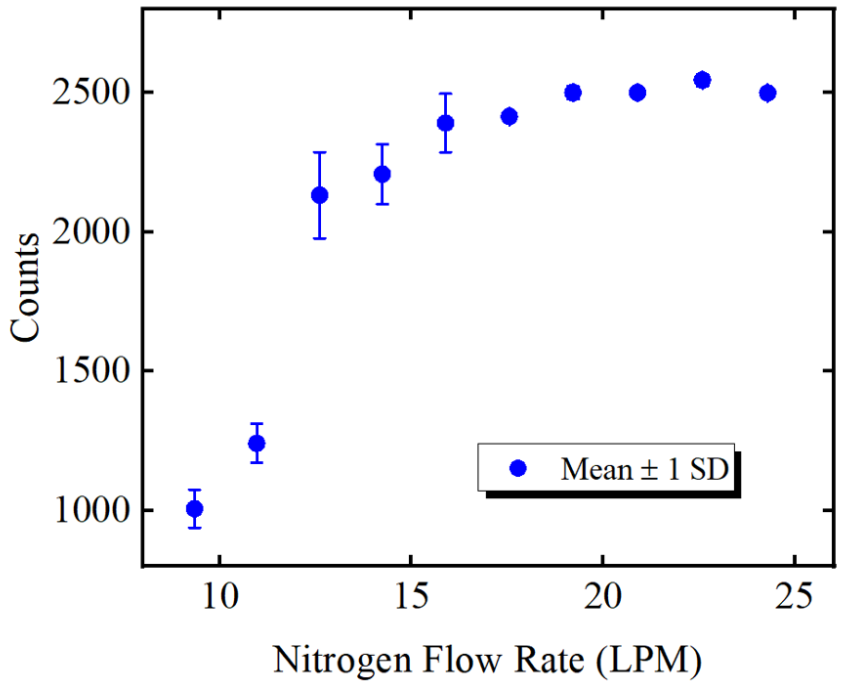

Figure 58: Large flow study results. Vertical error bars indicate 1 standard deviation calculated from the measured results at each flow rate. The horizontal error bars represent the repeatability of the flow meter, but are not visible at this scale.

flow regime:

$$N_{counts} = (600 \pm 36)_{[\frac{counts}{LPM}]}(\dot{V}) - (5399 \pm 414)_{[counts]} \tag{48}$$

The linearity of the response indicates 0.82 ±0.061 LPM is a more realistic operating range for the device. Future testing could work to identify the largest possible linear operating range. The results also show, when using average values, that the device can detect changes as small as 165±61 sccm (0.347±0.128m/s) consistently. The linear model suggests a resolution of 600±36, or 285±17 counts/ms^{-1} assuming the velocity at the device matches the velocity at the nozzle. The uncertainty of the linear model was derived from repeated measurements. The high-frequency of the device's rotation allows it to theoretically detect changes of 1.667 sccm and 0.0351 ms^{-1} as a change of 1 count, but the observed variability would make these readings inaccurate. The variability from the repeated measurements dominated the uncertainty of the sensor and limited its resolution. Improving the consistency of the rotation should be the target area for improving this device. The results of the fine flow test are included in figure 59. The calculated results from these experiments are included in table 12.

The vast majority of testing was performed with the dry device after depositing the reflective coating and removing the supports. One series of measurements was made with the silicone oil lubricant added to the device in an attempt to stabilize the rotation. The results were very promising for future work. The rotational became much more stable, at the cost of low-speed operation. The increased surface tension from the oil meant the rotor would only start spinning very slowly at approximately 10.97±1.21 LPM (23.09±2.55m/s), and only spinning consistently around 14.24±1.21 LPM (29.98±2.55m/s). A 0.5sec sample of the periodic reflection spectrum for each test is included in figure 60. Only four flows were tested, from (14.24 - 24.28)±1.21

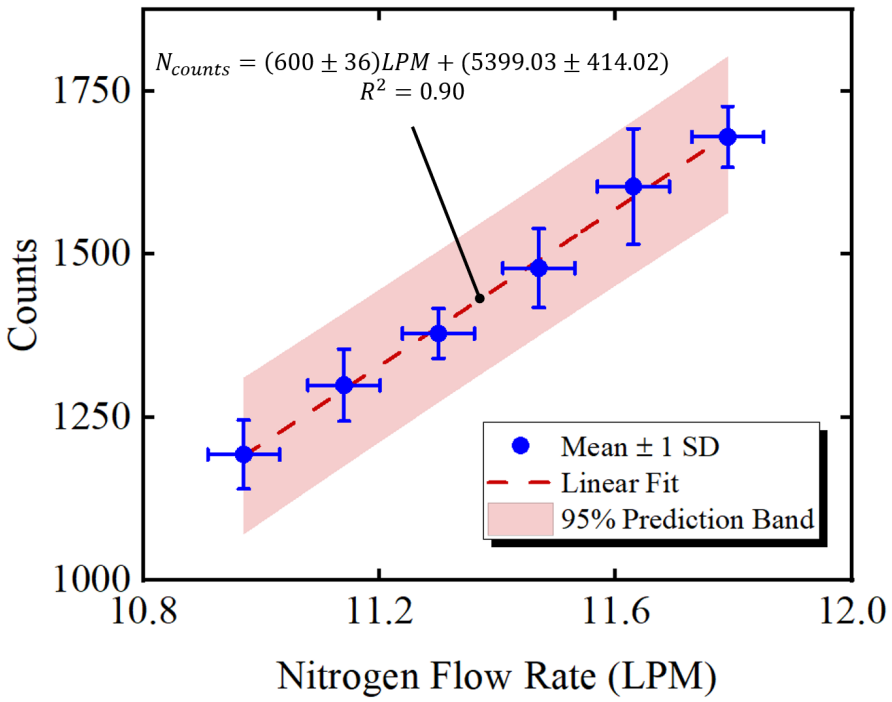

Figure 59: Fine flow study result. Vertical error bars were calculated from repeated measurements and represent 1 standard deviation from the mean value. The horizontal error bars represent the repeatability of the flow meter. The 95% prediction band for the linear fit was calculated from the repeated measurements only.

LPM (29.98 - 51.11±2.55m/s). The results are plotted in figure 61, in rotations per minute (RPM) instead of counts. The rotation was consistent enough to calculate rotational speed by sampling a small portion of the response. A fine study was not performed in the scope of this work, but the greatly increased stability may increase the reliability and resolution of the device. The lubrication may also help the device perform at even higher flow rates and velocities, as the rotation trended upward in higher flows as the speed helps overcomes the friction between the rotor and stator through the lubricant. The upward non-linear response is likely due to the new friction coefficient and surface tension introduced with the liquid lubricant. The turbulence introduced by the fiber face would continue to play a major role in the flow field as well. Further study is required to fully characterize the effects of the lubricant on the

nature and repeatability of the rotational response.

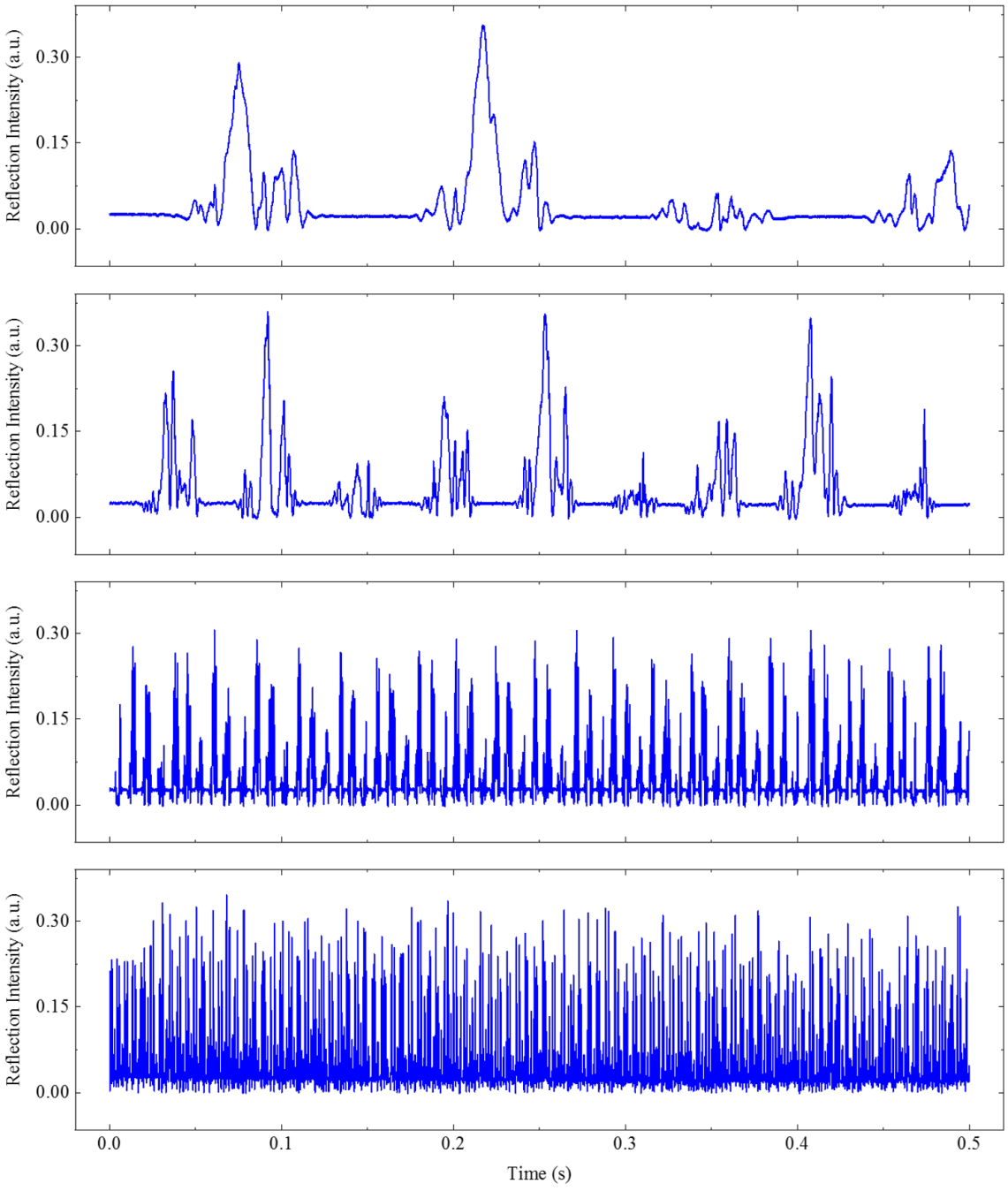

Figure 60: Excerpt of the reflection response of the lubricated device over 0.5 seconds at four flows: (a) 14.24±1.21 LPM (29.98±2.55m/s) (b) 17.55±1.21 LPM (36.95±2.55m/s) (c) 20.89±1.21 LPM (43.98±2.55m/s) (d) 24.28±1.21 LPM (51.11±2.55m/s)

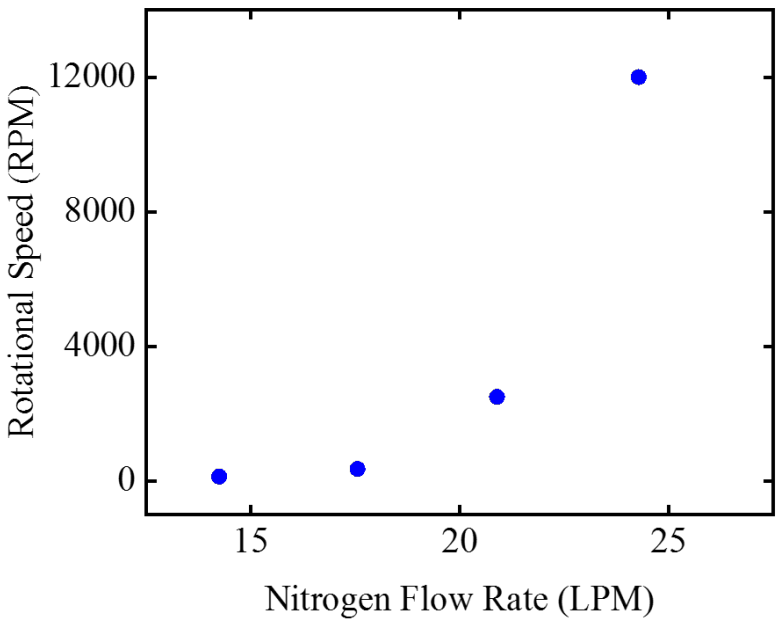

Figure 61: Calculated RPM of the lubricated device at four different flow rates.

Table 12: Micro flow sensor results.

Operating Range	(9.35 - 24.28)±1.21 LPM
	(19.68 - 51.11)± 2.55 m/s
Flow Sensitivity (Linear Fit)	600±36 Counts/LPM
	(285±17 Counts/ms^{-1})
Smallest Measured	165±61 sccm
	(0.347±0.128m/s)

5.4 Conclusion

This device successfully demonstrated a microscale flow sensor fabricated onto a fiber optic tip by two-photon polymerization. The device utilized an aerodynamic geometry that can not be produced by traditional planar micro fabrication to create a low size, weight, and power (SWAP) sensor. Integration onto an fiber optic enabled remote sensing, potentially over kilometers, with a single cable. The sensor was shown to operate at high gas flows at a resolution on-par with the commercial flow meter used for testing. Moving parts with 2-μm clearance, 0.1-μm fabrication resolution, and arbitrary curved geometries were demonstrated. The device showed a linear response over a flow regime of 0.82 ±0.061 LPM, and appears to respond linearly over a significant portion of its operating range. The operating speed could also be adjusted by changing the geometry of the blades, a simple prospect for batch fabrication with 2PP microfabrication. The resolution is currently limited by the repeatability of each measurement, which could be improved with superior stability. Initial tests were performed with a silicone-oil lubricant that greatly increased the rotational stability and paved the way for future research.

Future work can look to this device as a demonstrator of the physical capabilities of 2PP microfabrication. To improve this sensor, some specific ideas are to:

- Test the current sensor in liquid flow.

- Explore different lubrications, perform repeated measurements with a lubricated device, determine the response profile of a lubricated device, and measure small resolution changes with a lubricated device.
- Improve the aerodynamics of the rotor with a curved front to reduce drag, and a longer, taller blade to improve propulsive force.
- Design and test an on-fiber cup-style anemometer for sensing lateral flow and potentially improving rotational stability.
- Model the complete flow scenario in CFD, including the turbulence induced by the fiber face in order to predict rotational response and inform future designs.

Appendix A. Software and MATLAB Code

Two nanoscribe programs were used during fabrication, the slicer DeScribe and the machine UI NanoWrite. The DeScribe files used for each device are included in figures 66, 67, and 68. The NanoWrite screen is included in figure 69.

The variable wavelength laser sweep was controlled by a Labview-based VI from Sacher Lasertecnik called Motor Motion Controller. This was implimented onto a PC and used to determine the length, speed, and start time of the sweep. The operating window and settings used during each measurement are included in figure 62.

Two free programs were used to create a trigger on the variable wavelength laser. The first was called SoundArb, and it controlled the on-board sound card of a PC to create a function generator. The operating window and settings used to create the impulse is pictured in figure 63. The other program was a mouse-macro recorder called Mini Mouse Macro. This was used to record the clicks necessary to start the

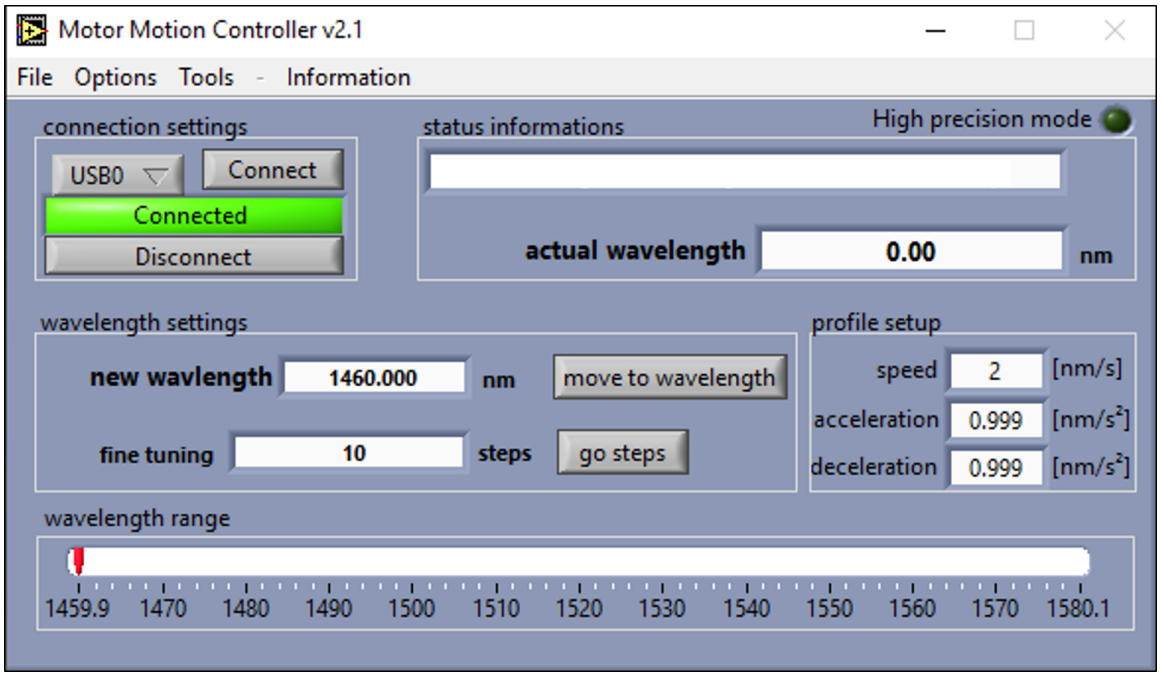

Figure 62: Motor Motion Controller variable wavelength laser VI used to control the sweep.

wavelength sweep and the trigger from SoundArb and repeat them identically for every measurement. The operating window and the macro used is pictured in figure 64.

To analyze data, MATLAB was used extensively. Each measurement required a slight changes to the basic program that filtered out the high frequency noise from the laser's motor and located the resonant peaks. An example of the code used is included in figure 65.

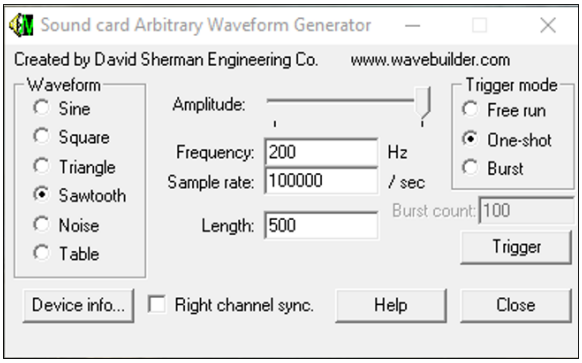

Figure 63: SoundArb software used to control a PC sound card as a function generator and create the trigger impulse for each measurement.

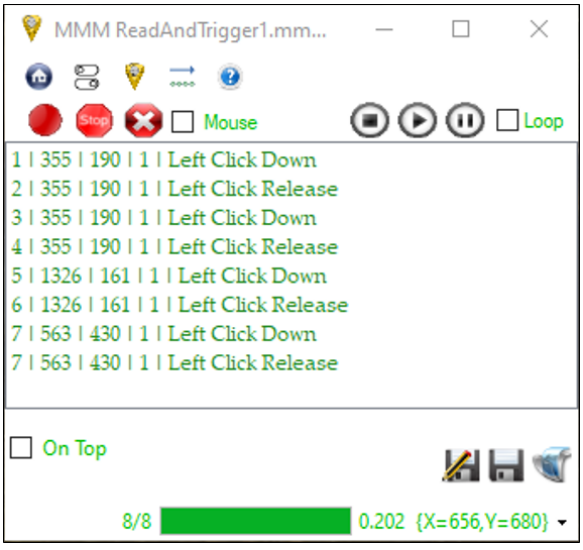

Figure 64: MiniMouseMacro used to record and repeat the clicks necessary to initiate the sweep and impulse 7ms apart for each measurement.

```
%Loading wavelength-dependent power floor from an average of three measurements
power=readtable('AvgRefl.txt');
power=table2array(power);
power=power;

%Defining varaibles
Air=1;
LocsAir=2;

%Loading reflection spectrum
Air=readtable('Air.txt');
Air=table2array(Air);

%Subtracting power floor
Air(:,2)=Air(:,2)-power;
Air(:,2)=Air(:,2)*-1;

%Filtering to reduce noise from the laser motor vibration
Air(:,2)=smooth(Air(:,2),20);

%Finding the peaks with a minimum prominence of 1V on either side
[Q,LocsAir]=findpeaks(Air(:,2)*-1,'MinPeakProminence',1);
LocsAir=Air(LocsAir,1);

%Output filtered reflection spectrum
Air=table(Air);
writetable(Air,'Air Smooth and Flat.txt','Delimiter',' ');

%Output resonant peak locations
LocsAir=table(LocsAir);
writetable(LocsAir,'Air Peak Wavelengths.txt','Delimiter',' ');
```

Figure 65: Example MATLAB code used to filter noise from the vibration of the laser motor and find the resonant peaks.

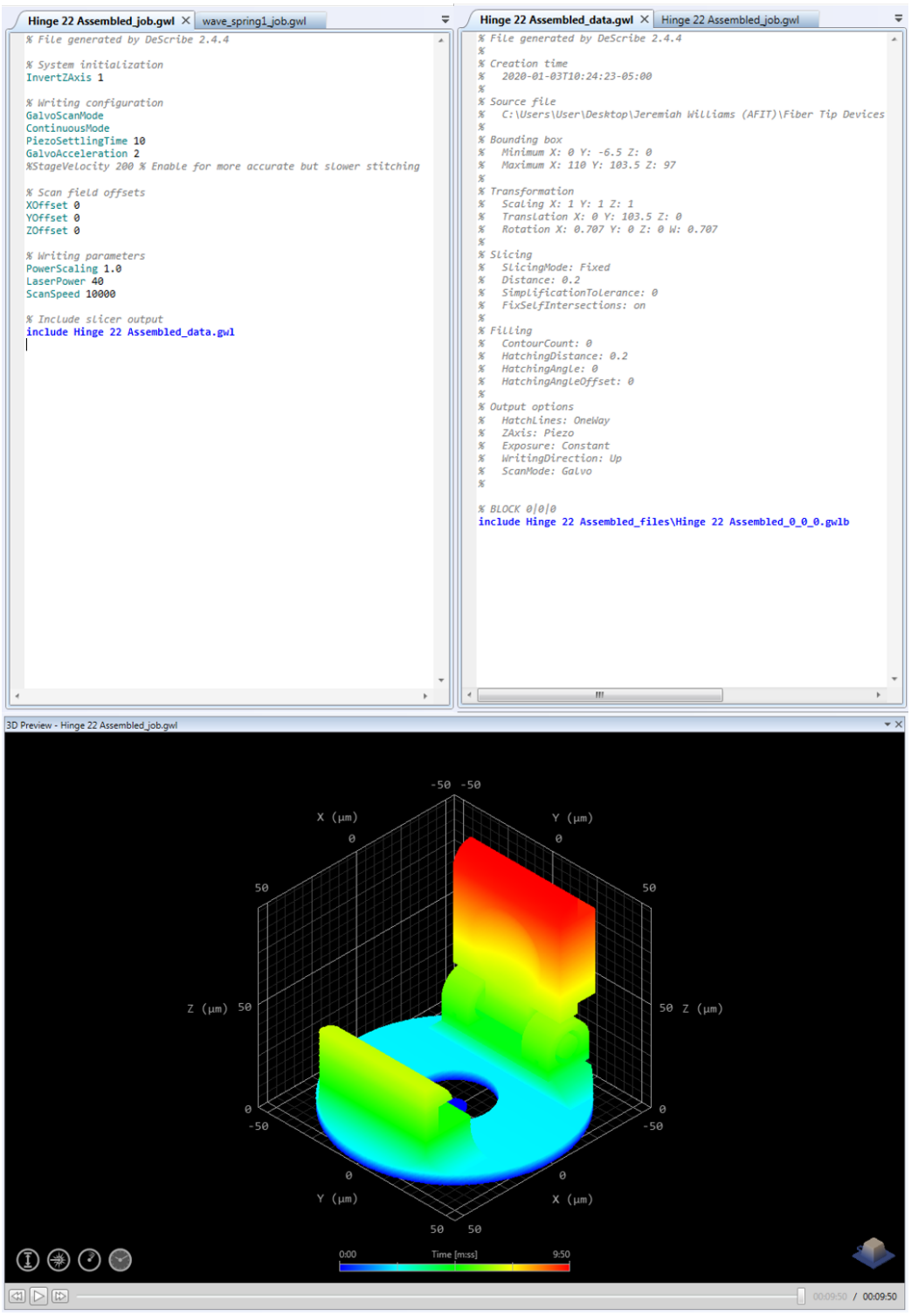

Figure 66: DeScribe slicer files used to fabricate the hinged FP cavity RI sensor.

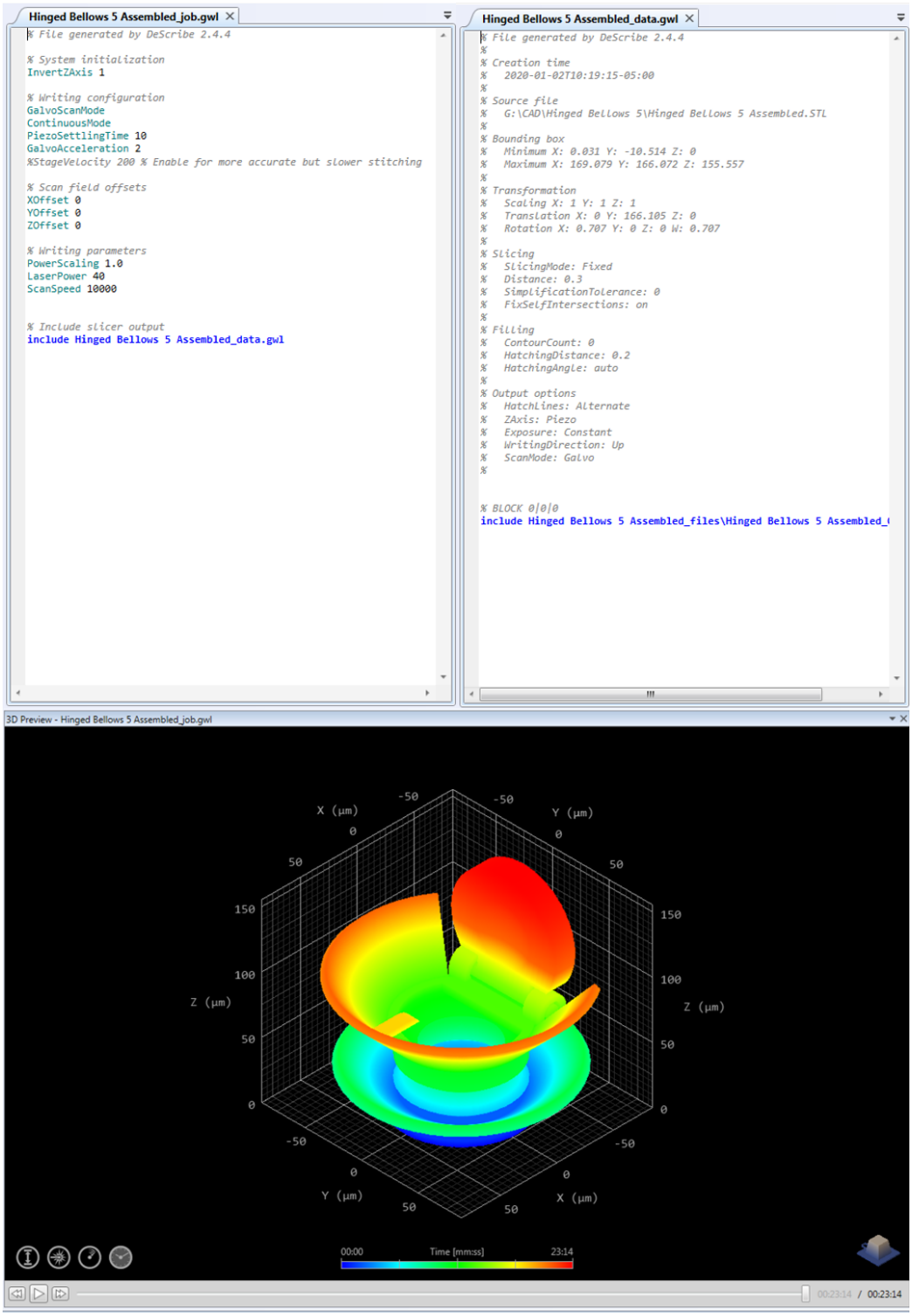

Figure 67: DeScribe slicer files used to fabricate the hinged spring-body pressure sensor.

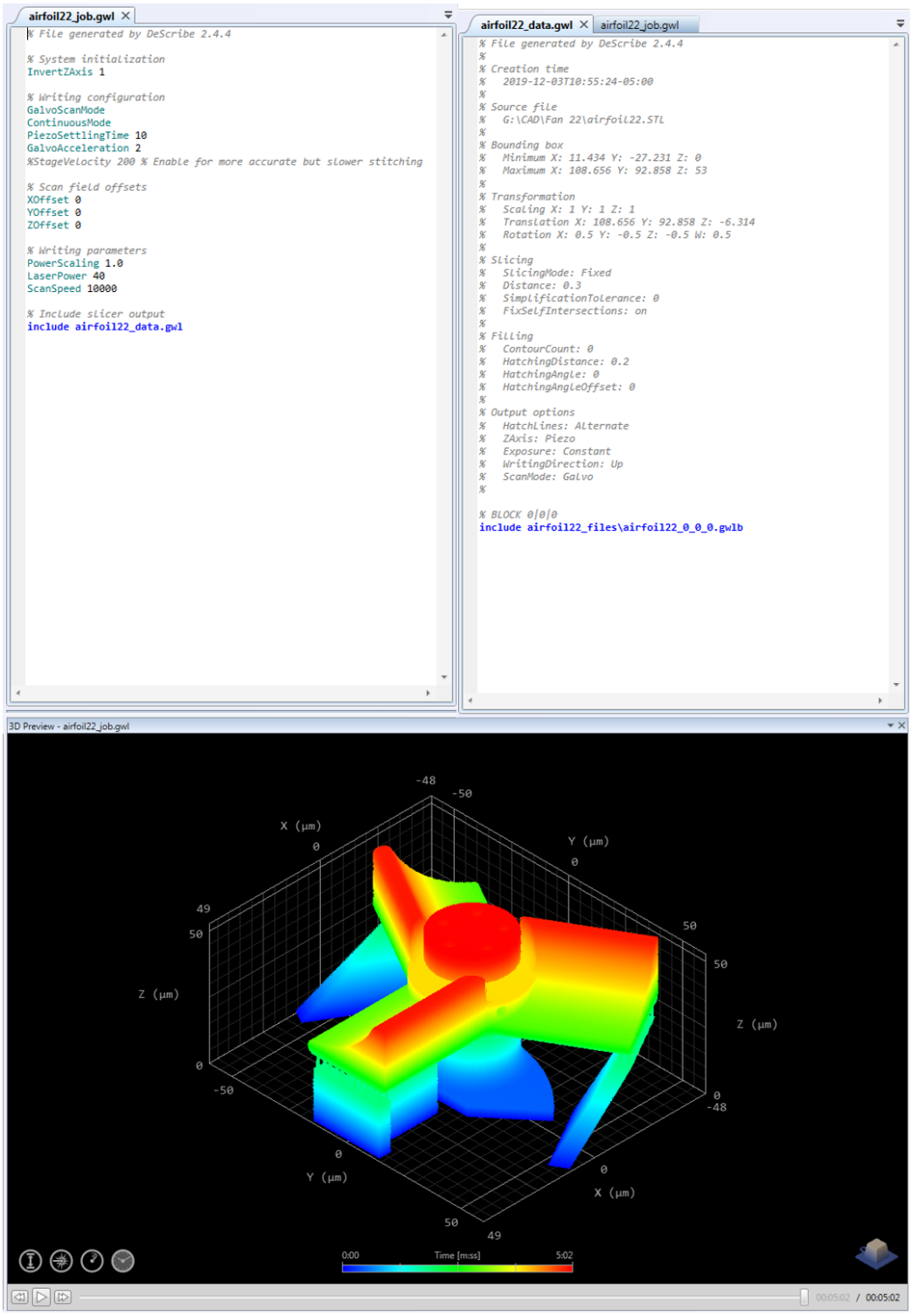

Figure 68: DeScribe slicer files used to fabricate the spinning flow sensor.

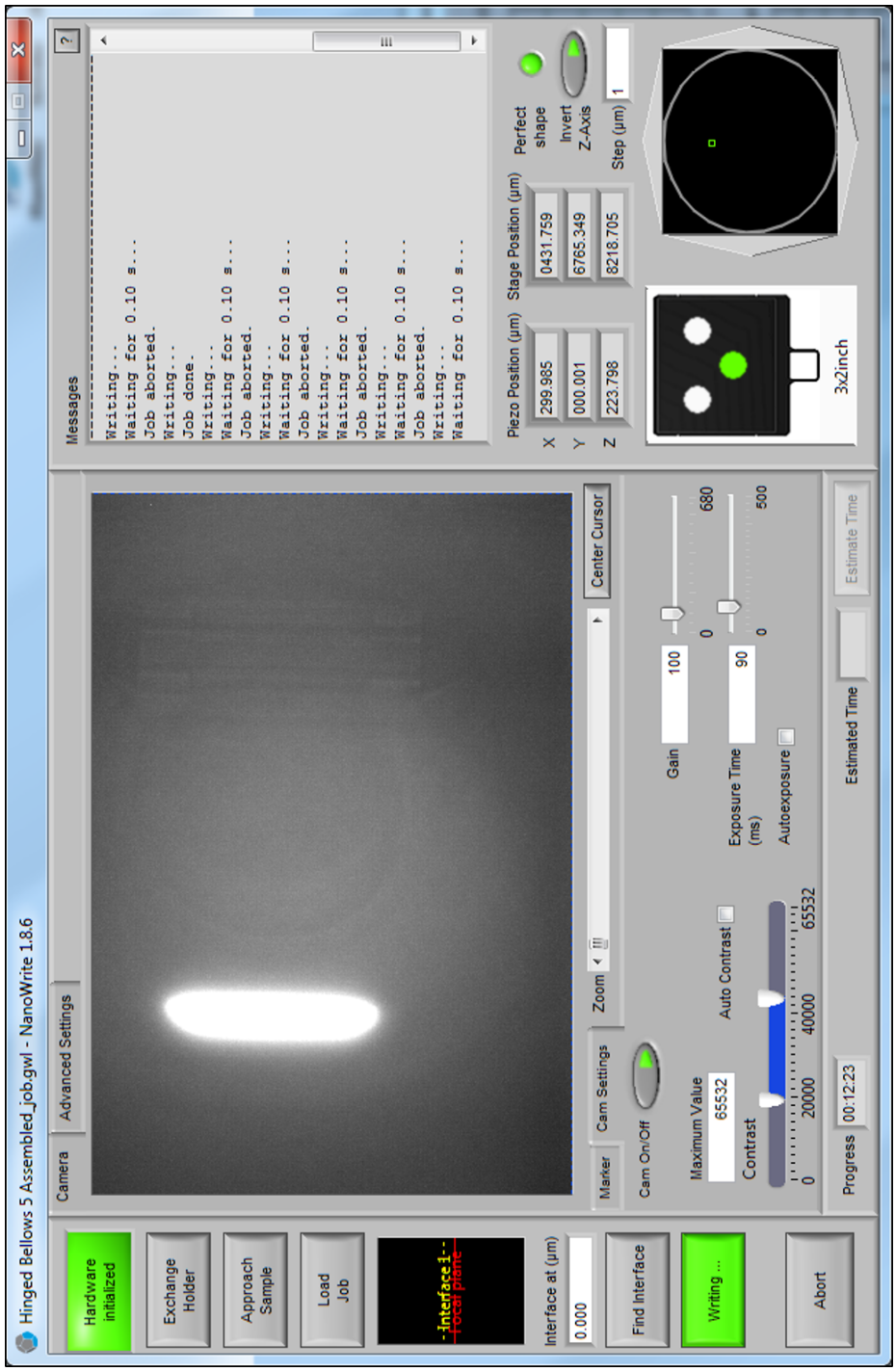

Figure 69: Screen capture of the NanoWrite VI used to operate the Nanoscribe system. A spring-body pressure sensor is being polymerized.

Appendix B. Spring-Body Pressure Sensor Confirmation Experiment

This test was performed to confirm that the cavity of the spring-body pressure sensor was successfully sealed and not simply changing with the RI of air leaking into the cavity. First, a device was measured with the cap in position but without cured optical adhesive. A small amount of adhesive was placed on the hinge to prevent the top falling open, as the latching mechanism of this device was broken. This un-sealed device was exposed to the test described in subsection 4.2.4, but starting measurements at -10 in-Hg of vacuum. The location of a resonant peak is included in figure 70 (a). There is a large initial change as vacuum is applied and the top opens to allow the air inside the cavity to escape. After this, there is no significant trend observable on this scale. The reflection intensity also lowered significantly after vacuum was applied, indicating the top had moved out of alignment.

Next the device was sealed with optical adhesive as described in subsection 4.2.3. The same test was then repeated. The device exhibited a clearly linear response in the opposite direction as the hinged FP cavity RI sensor, which is included in figure 70. This was taken as confirmation that the spring body was sealed and expanding with different pressures. Additionally, there was no significant loss in reflection intensity at higher vacuum pressures.

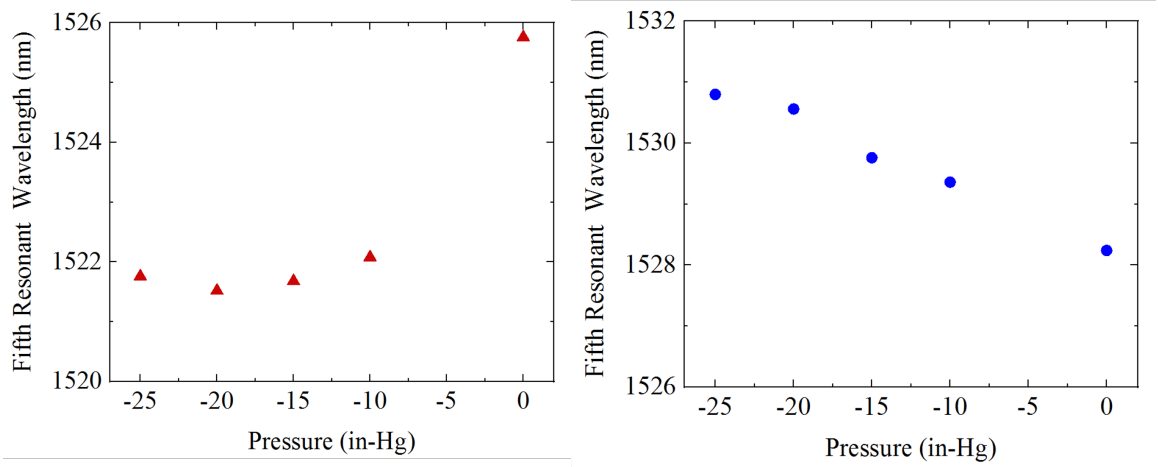

Figure 70: Resonant peak locations of the spring-body pressure sensor confirmation experiment. (a) The unglued device. (b) The glued and sealed device.

Appendix C. Technical Drawings of Devices

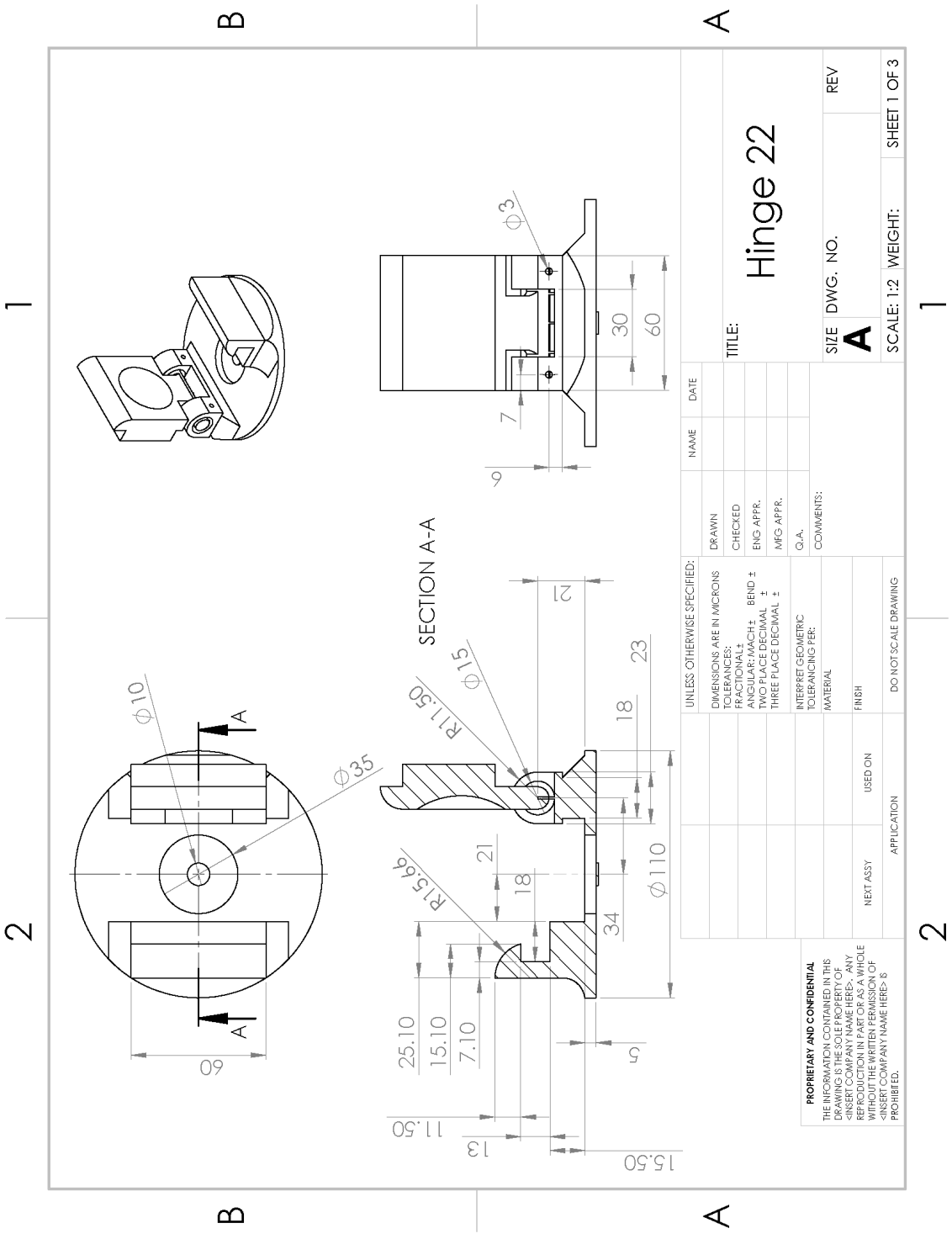

Figure 71: Technical drawing of the hinged FP cavity RI sensor, page 1.

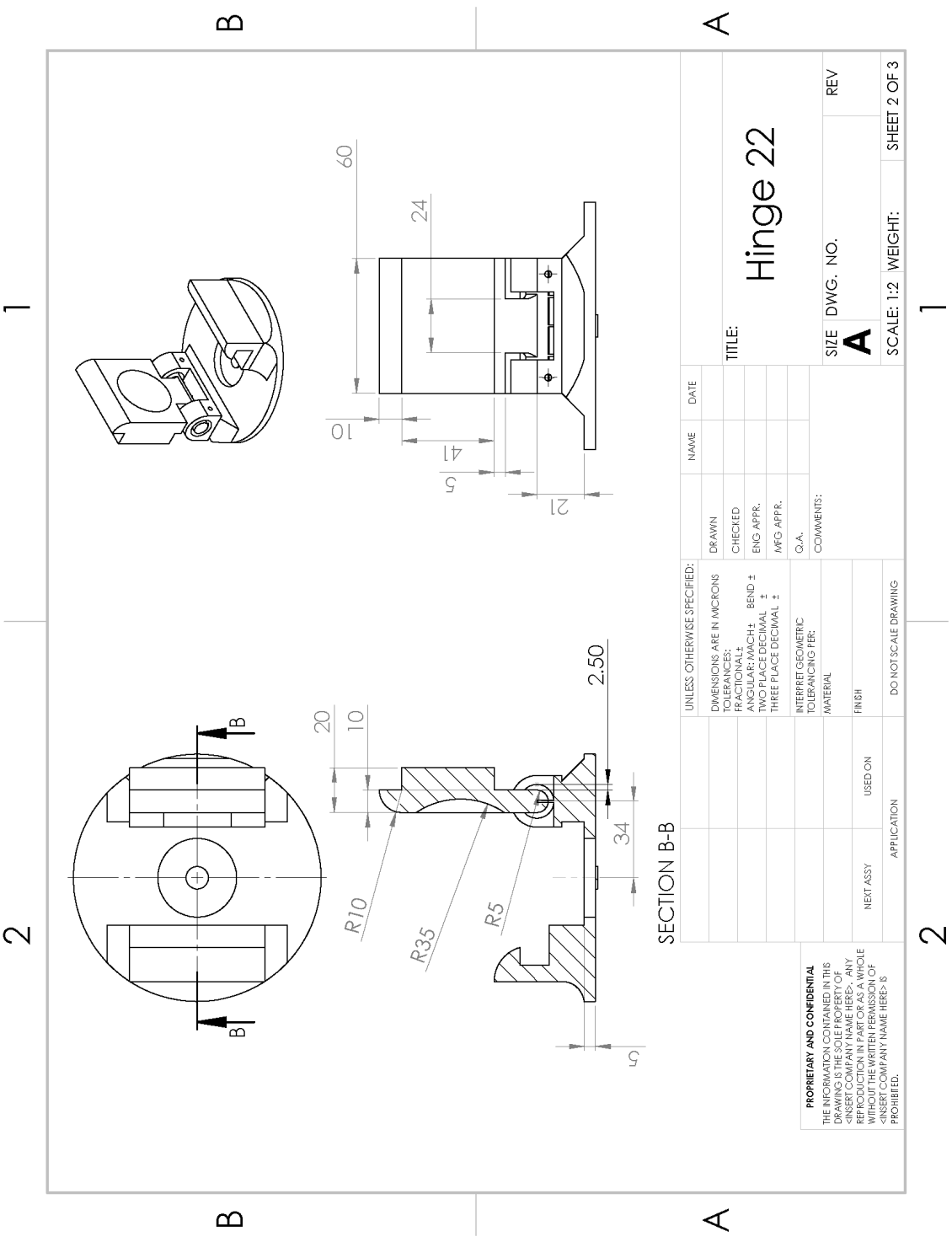

Figure 72: Technical drawing of the hinged FP cavity RI sensor, page 2.

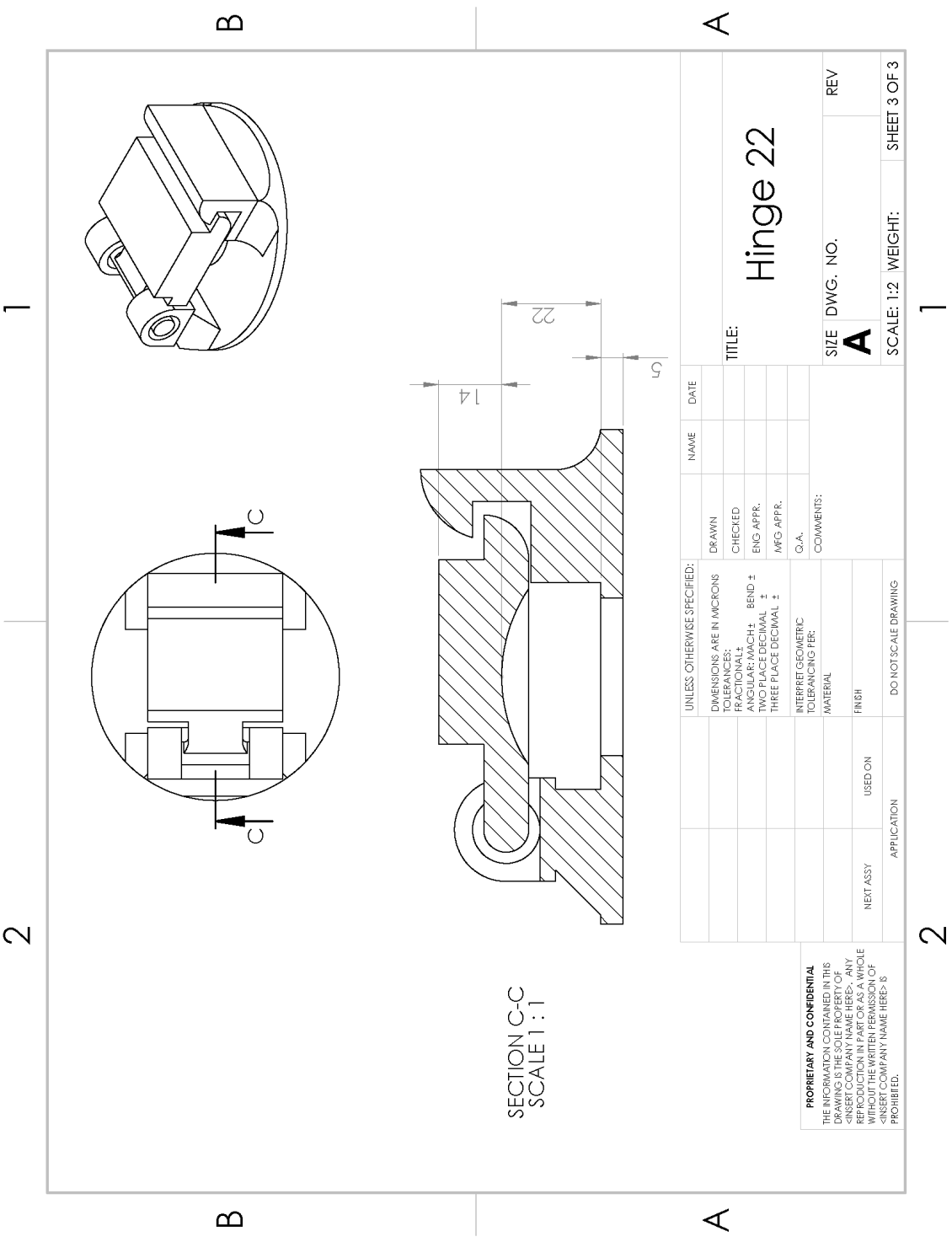

Figure 73: Technical drawing of the hinged FP cavity RI sensor, page 3.

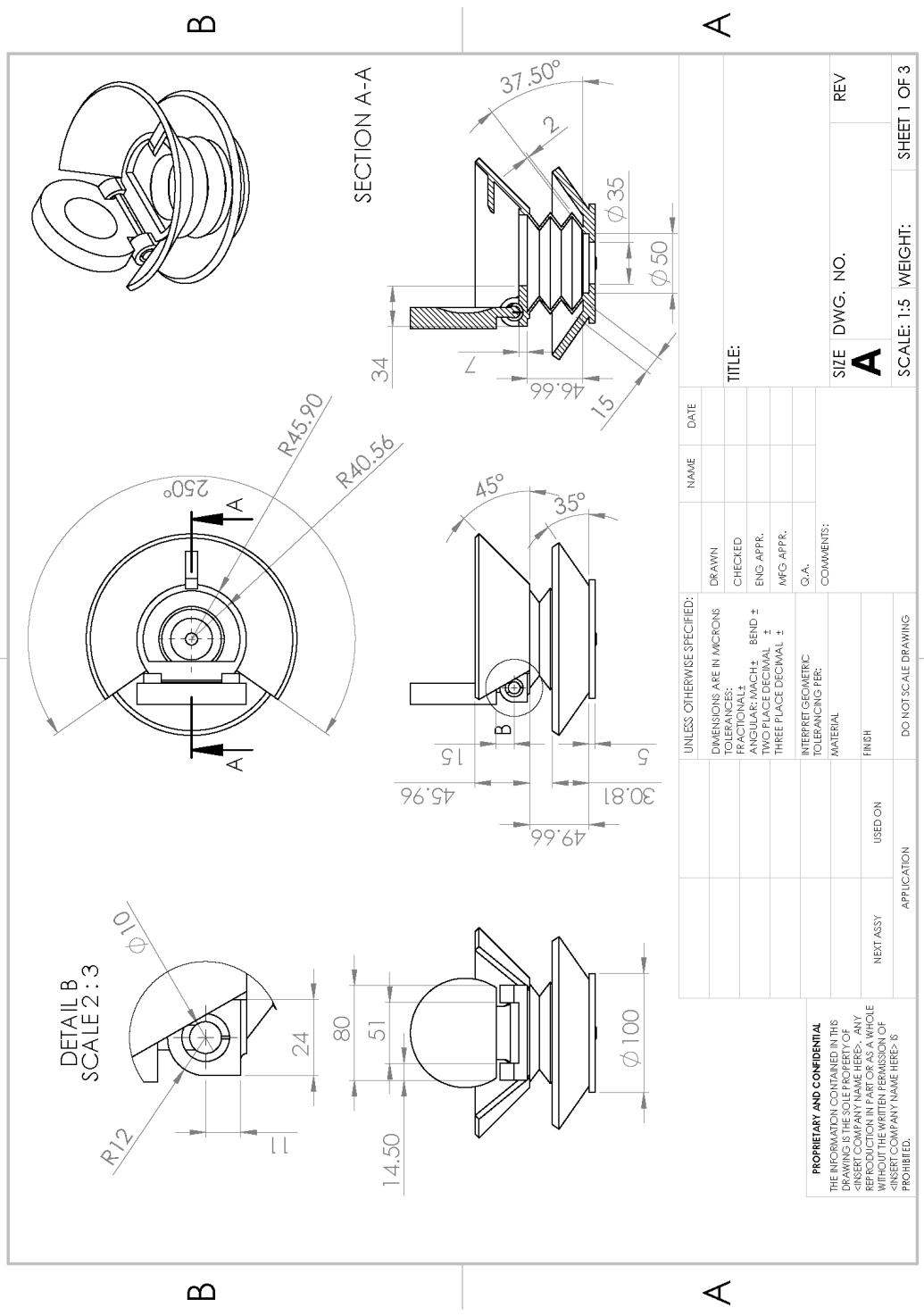

Figure 74: Technical drawing of the spring-body pressure sensor, page 1.

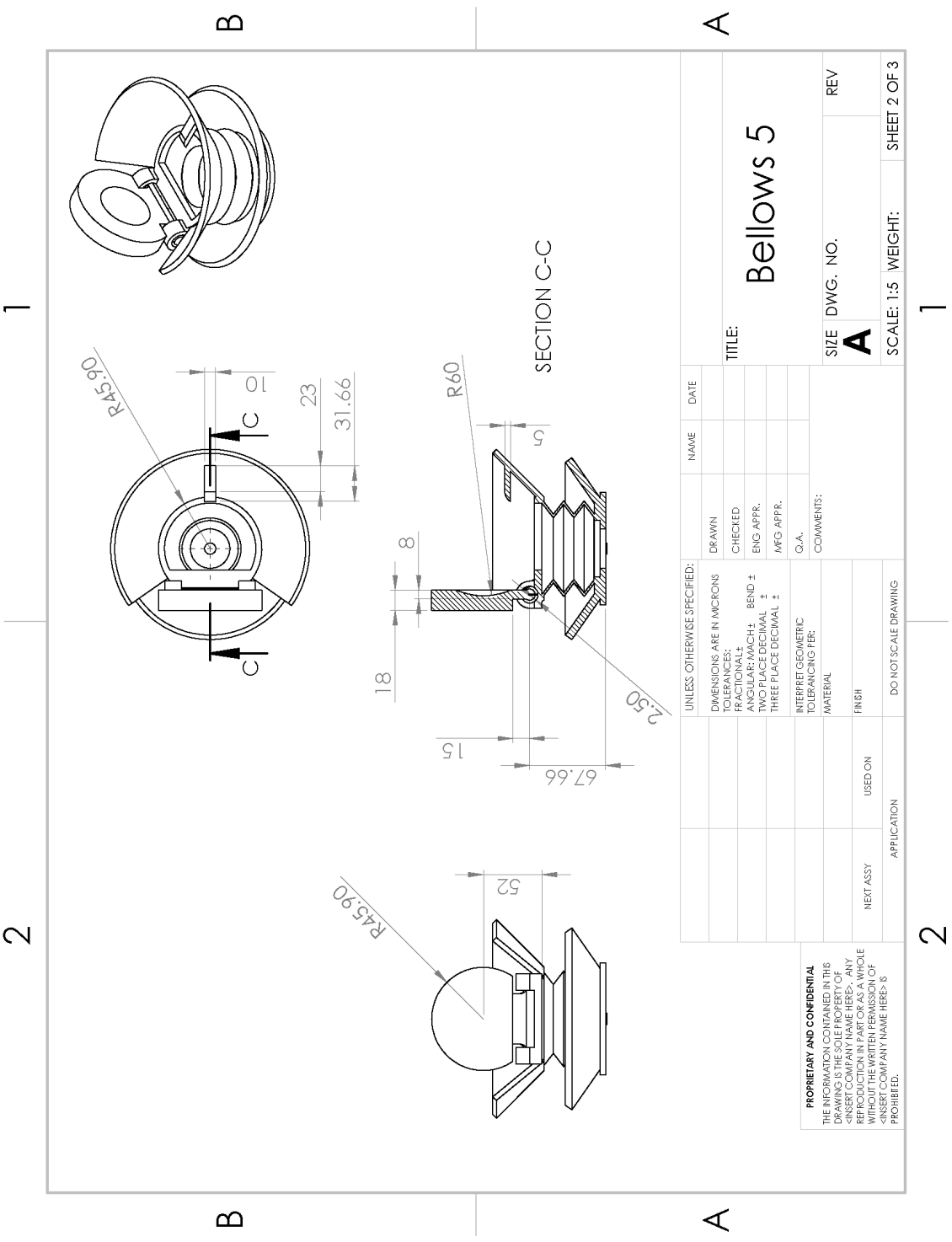

Figure 75: Technical drawing of the spring-body pressure sensor, page 2.

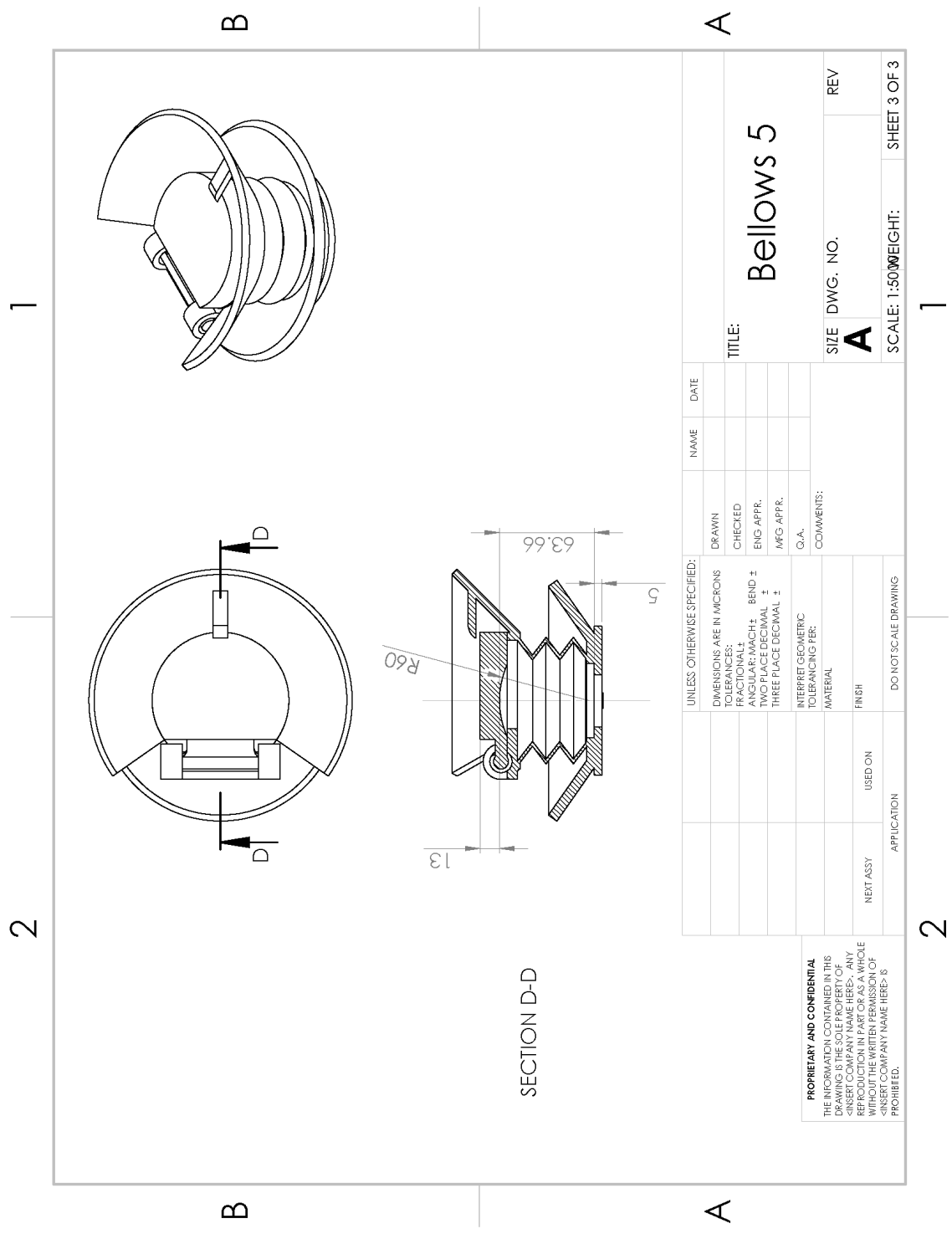

Figure 76: Technical drawing of the spring-body pressure sensor, page 3.

Figure 77: Technical drawing of the spinning flow sensor device, page 1.

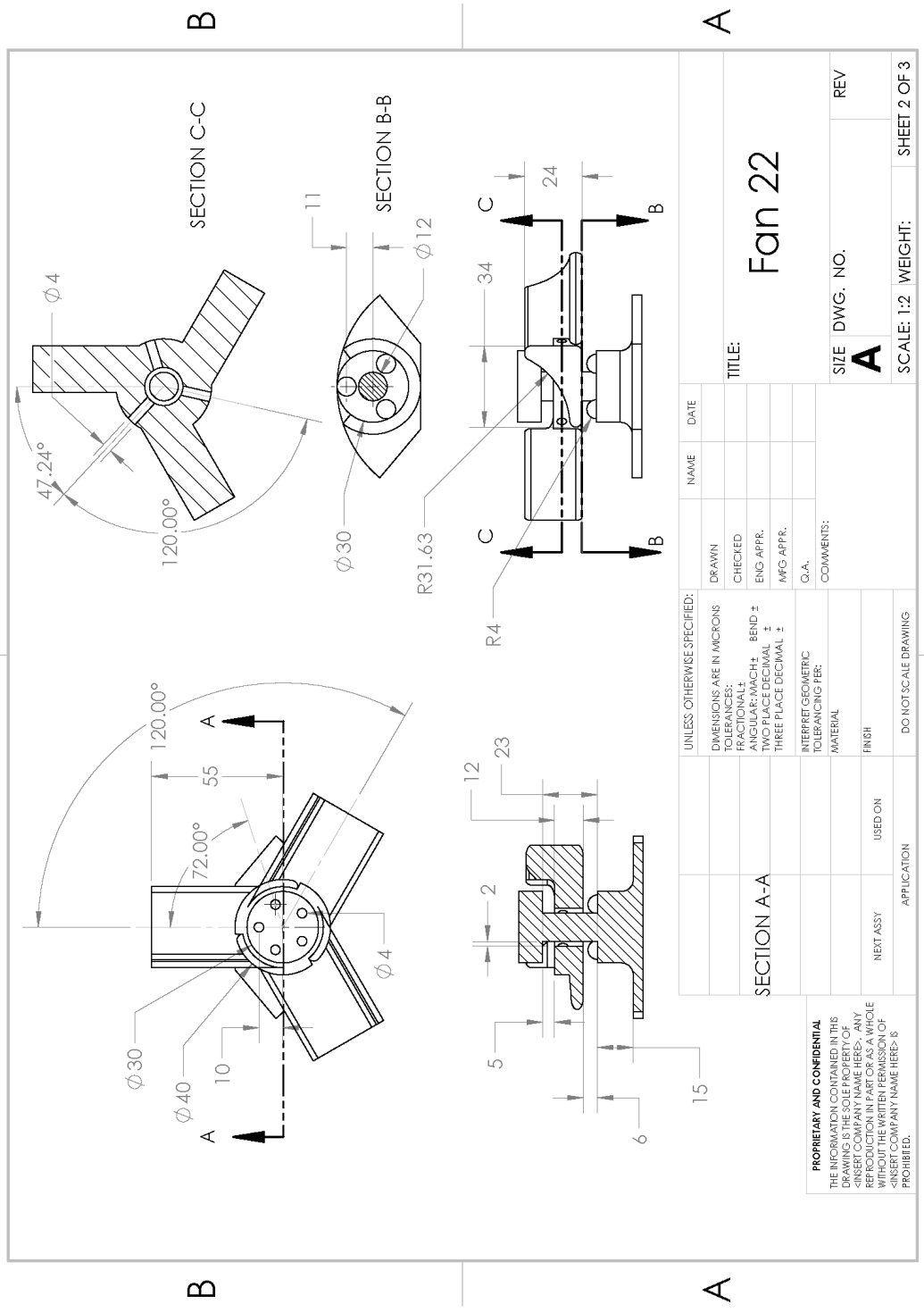

Figure 78: Technical drawing of the spinning flow sensor device, page 2.

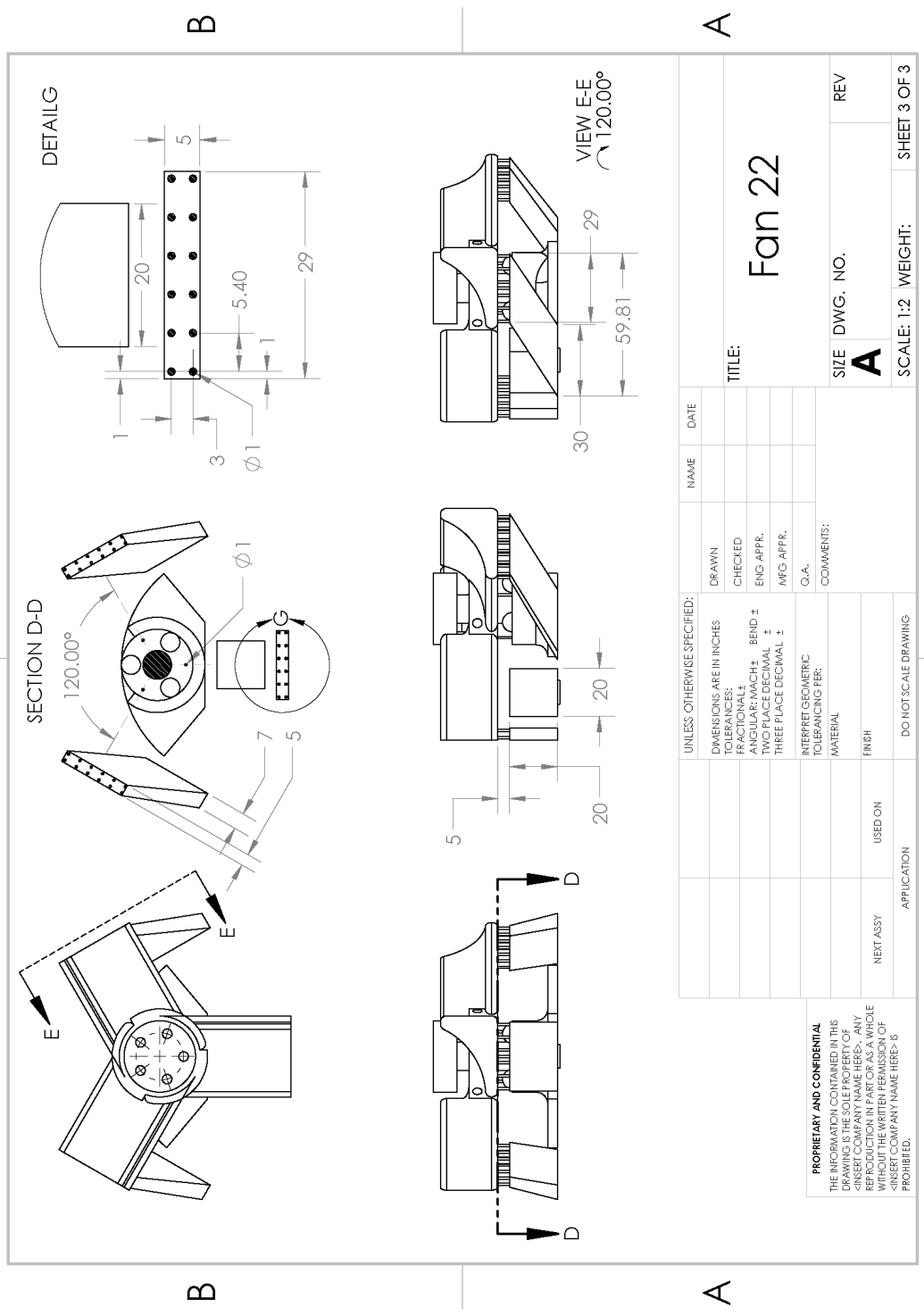

Figure 79: Technical drawing of the spinning flow sensor device, page 3.

Appendix D. Wavelength Dependent Power of the Variable Wavelength Laser Source

The laser used in this work had wavelength dependent power, which was subtracted from each measurement to flatten the result for more accurate analysis. The value used for this "power floor" was obtained by replacing the device with a cleaved fiber that had a thick reflective coating of gold. The reflection spectrum of this was read three times. The mean was taken as the power floor to be subtracted from subsequent measurements. This pure reflection is included in figure 80.

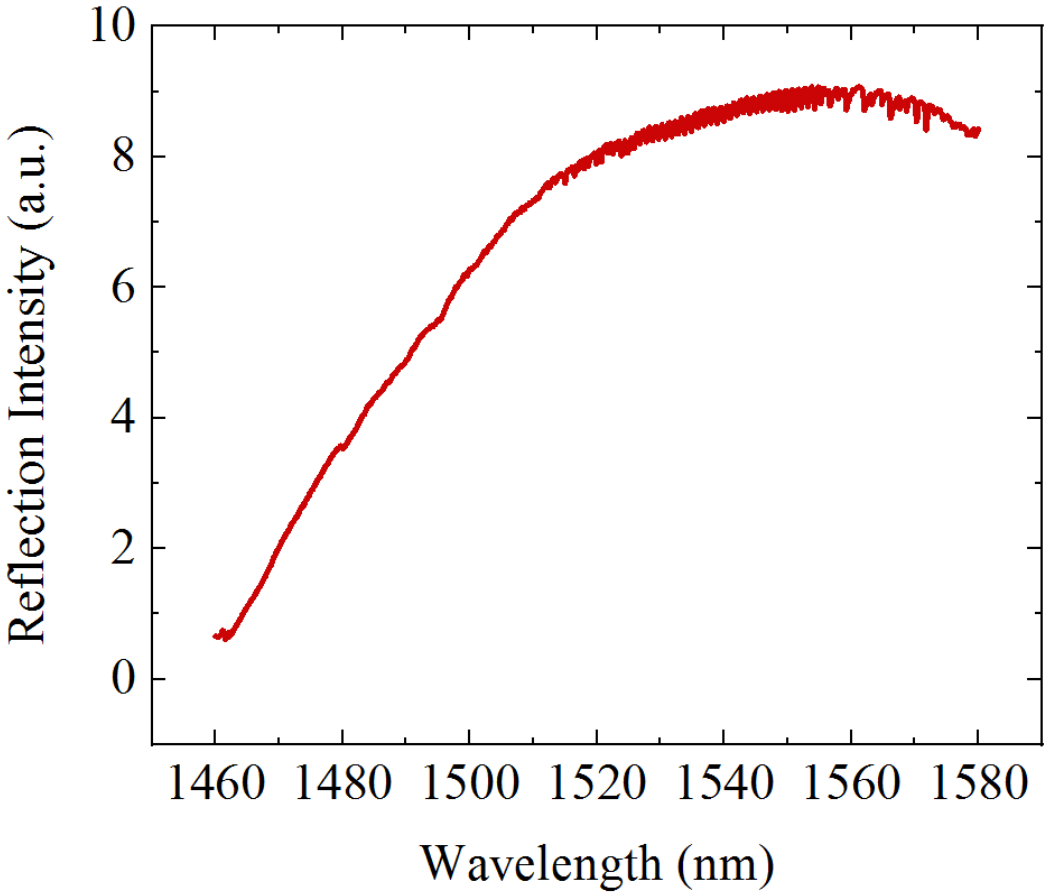

Figure 80: Wavelength-dependent power of the laser that was subtracted from each measurement to flatten the result and improve analysis.

Bibliography

1. Wikipedia contributors. Optical fiber — Wikipedia, the free encyclopedia, 2020. [Online; accessed 26-January-2020].

2. Fraunhofer Institute for Silicate Research ISC. Two-photon polymerization: Femtosecond laser pulses as a tool for true 3d micromachining, Mar 2020.

3. Shoji Maruo, Koji Ikuta, and Hayato Korogi. Force-controllable, optically driven micromachines fabricated by single-step two-photon microstereolithography. *Journal of Microelectromechanical Systems*, 12(5):533–539, 2003.

4. J Serbin, A Egbert, A Ostendorf, BN Chichkov, R Houbertz, G Domann, J Schulz, C Cronauer, L Fröhlich, and M Popall. Femtosecond laser-induced two-photon polymerization of inorganic–organic hybrid materials for applications in photonics. *Optics letters*, 28(5):301–303, 2003.

5. Simon Thiele, Kathrin Arzenbacher, Timo Gissibl, Harald Giessen, and Alois M Herkommer. 3d-printed eagle eye: Compound microlens system for foveated imaging. *Science advances*, 3(2):e1602655, 2017.

6. Vasileia Melissinaki, Maria Farsari, and Stavros Pissadakis. A fiber-endface, fabry–perot vapor microsensor fabricated by multiphoton polymerization. *IEEE Journal of Selected Topics in Quantum Electronics*, 21(4):344–353, 2014.

7. K Markiewicz and P Wasylczyk. Photonic-chip-on-tip: compound photonic devices fabricated on optical fibers. *Optics express*, 27(6):8440–8445, 2019.

8. Maura Power, Alex J Thompson, Salzitsa Anastasova, and Guang-Zhong Yang. A monolithic force-sensitive 3d microgripper fabricated on the tip of an optical fiber using 2-photon polymerization. *Small*, 14(16):1703964, 2018.

9. Henry E Williams, Daniel J Freppon, Stephen M Kuebler, Raymond C Rumpf, and Marco A Melino. Fabrication of three-dimensional micro-photonic structures on the tip of optical fibers using su-8. *Optics express*, 19(23):22910–22922, 2011.

10. Wikipedia contributors. Fiber bragg grating — Wikipedia, the free encyclopedia, 2019. [Online; accessed 26-January-2020].

11. CR Liao, TY Hu, and DN Wang. Optical fiber fabry-perot interferometer cavity fabricated by femtosecond laser micromachining and fusion splicing for refractive index sensing. *Optics express*, 20(20):22813–22818, 2012.

12. Jun Ma, Jian Ju, Long Jin, Wei Jin, and Dongning Wang. Fiber-tip micro-cavity for temperature and transverse load sensing. *Optics express*, 19(13):12418–12426, 2011.

13. Mingran Quan, Jiajun Tian, and Yong Yao. Ultra-high sensitivity fabry–perot interferometer gas refractive index fiber sensor based on photonic crystal fiber and vernier effect. *Optics letters*, 40(21):4891–4894, 2015.

14. AA Said, M Dugan, S De Man, and D Iannuzzi. Carving fiber-top cantilevers with femtosecond laser micromachining. *Journal of Micromechanics and Microengineering*, 18(3):035005, 2008.

15. Jing Feng, Ming Ding, Jun-Long Kou, Fei Xu, and Yan-Qing Lu. An optical fiber tip micrograting thermometer. *IEEE Photonics Journal*, 3(5):810–814, 2011.

16. Tao Wei, Yukun Han, Yanjun Li, Hai-Lung Tsai, and Hai Xiao. Temperature-insensitive miniaturized fiber inline fabry-perot interferometer for highly sensitive refractive index measurement. *Optics Express*, 16(8):5764–5769, 2008.

17. Xiaoling Tan, Xuejin Li, Youfu Geng, Zhen Yin, Lele Wang, Wenyuan Wang, and Yuanlong Deng. Polymer microbubble-based fabry–perot fiber interferome-

ter and sensing applications. *IEEE Photonics Technology Letters*, 27(19):2035–2038, 2015.

18. Silas C Nesson, Miao Yu, XM Zhang, and Adam H Hsieh. Miniature fiber optic pressure sensor with composite polymer-metal diaphragm for intradiscal pressure measurements. *Journal of biomedical optics*, 13(4):044040, 2008.

19. Hyungdae Bae, David Yun, Haijun Liu, Douglas A Olson, and Miao Yu. Hybrid miniature fabry–perot sensor with dual optical cavities for simultaneous pressure and temperature measurements. *Journal of Lightwave Technology*, 32(8):1585–1593, 2014.

20. Zhenwei Xie, Shengfei Feng, Peijie Wang, Lisheng Zhang, Xin Ren, Lin Cui, Tianrui Zhai, Jie Chen, Yonglu Wang, Xinke Wang, et al. Demonstration of a 3d radar-like sers sensor micro-and nanofabricated on an optical fiber. *Advanced Optical Materials*, 3(9):1232–1239, 2015.

21. Yanwen Qi, Siyao Zhang, Shengfei Feng, Xinke Wang, Wenfeng Sun, Jiasheng Ye, Peng Han, and Yan Zhang. Integrated mach-zehnder interferometer on the end facet of multicore fiber for refractive index sensing application. In *2017 International Conference on Optical Instruments and Technology: IRMMW-THz Technologies and Applications*, volume 10623, page 106230T. International Society for Optics and Photonics, 2018.

22. Peter Gaso, Daniel Jandura, and Jana Durisova. Optical fiber tip wth integrated mach-zehnder interferometer for sensor applications. *Advances in Electrical and Electronic Engineering*, 17(4):466–471, 2019.

23. Simon Pevec and Denis Donlagic. Miniature fiber-optic pitot tube sensor. *IEEE Sensors Journal*, 2020.

24. Po-Yau Ju, Chien-Hsiung Tsai, Lung-Ming Fu, and Che-Hsin Lin. Microfluidic flow meter and viscometer utilizing flow-induced vibration on an optic fiber cantilever. In *2011 16th International Solid-State Sensors, Actuators and Microsystems Conference*, pages 1428–1431. IEEE, 2011.

25. Guigen Liu, Qiwen Sheng, Weilin Hou, and Ming Han. Optical fiber vector flow sensor based on a silicon fabry–perot interferometer array. *Optics letters*, 41(20):4629–4632, 2016.

26. Matthew R Maschmann, Gregory J Ehlert, Benjamin T Dickinson, David M Phillips, Cody W Ray, Greg W Reich, and Jeffery W Baur. Bioinspired carbon nanotube fuzzy fiber hair sensor for air-flow detection. *Advanced Materials*, 26(20):3230–3234, 2014.

27. Jonathan W Smith. 3-d multifunctional sensors fabricated on fiber tips using a two-photon polymerization process. 2019.

28. Jay H. Zimmerman and Jack A. Stone. Index of refraction of air, Nov 2004.

29. Enrico Domenico Lemma, Francesco Rizzi, Tommaso Dattoma, Barbara Spagnolo, Leonardo Sileo, Antonio Qualtieri, Massimo De Vittorio, and Ferruccio Pisanello. Mechanical properties tunability of three-dimensional polymeric structures in two-photon lithography. *IEEE transactions on nanotechnology*, 16(1):23–31, 2016.

30. Jesus Delgado Alonso, David Berry, Narciso Guzman, Sarah Mottino, George Hellstern, Armando Soto, Lloyd Tripp, and Cinda Chullen. Sensor integrated pilot mask for on-board, real-time, monitoring of pilot breathing gas. 2018.

31. Welcome to nanoguide.

32. Mohammad H Bitarafan and Ray G DeCorby. On-chip high-finesse fabry-perot microcavities for optical sensing and quantum information. *Sensors*, 17(8):1748, 2017.

33. Eugene Hecht. *Optics, 5e*. Pearson Education, 2017.

34. Xiaoqin Wu, Yipei Wang, Qiushu Chen, Yu-Cheng Chen, Xuzhou Li, Limin Tong, and Xudong Fan. High-q, low-mode-volume microsphere-integrated fabry–perot cavity for optofluidic lasing applications. *Photonics Research*, 7(1):50–60, 2019.

35. Xiaoqin Wu, Qiushu Chen, Yipei Wang, Xiaotian Tan, and Xudong Fan. Stable high-q bouncing ball modes inside a fabry–perot cavity. *ACS Photonics*, 6(10):2470–2478, 2019.

36. Wenjie Wang, Chunhua Zhou, Tingting Zhang, Jingdong Chen, Shaoding Liu, and Xudong Fan. Optofluidic laser array based on stable high-q fabry–pérot microcavities. *Lab on a Chip*, 15(19):3862–3869, 2015.

37. C Toninelli, Y Delley, T Stöferle, A Renn, Stephan Götzinger, and Vahid Sandoghdar. A scanning microcavity for in situ control of single-molecule emission. *Applied Physics Letters*, 97(2):021107, 2010.

38. David Hunger, Christian Deutsch, Russell J Barbour, Richard J Warburton, and Jakob Reichel. Laser micro-fabrication of concave, low-roughness features in silica. *Aip Advances*, 2(1):012119, 2012.

39. Yu-Cheng Chen, Qiushu Chen, Tingting Zhang, Wenjie Wang, and Xudong Fan. Versatile tissue lasers based on high-q fabry–pérot microcavities. *Lab on a Chip*, 17(3):538–548, 2017.

40. Xiangfeng Duan, Yu Huang, Ritesh Agarwal, and Charles M Lieber. Single-nanowire electrically driven lasers. *Nature*, 421(6920):241–245, 2003.

41. Bassam Saadany, Maurine Malak, Masanori Kubota, Frdric Marty, Yoshio Mita, Diaa Khalil, and Tarik Bourouina. Free-space tunable and drop optical filters using vertical bragg mirrors on silicon. *IEEE journal of selected topics in quantum electronics*, 12(6):1480–1488, 2006.

42. H Cai, B Liu, XM Zhang, AQ Liu, J Tamil, T Bourouina, and QX Zhang. A micromachined tunable coupled-cavity laser for wide tuning range and high spectral purity. *Optics express*, 16(21):16670–16679, 2008.

43. Jonathan Masson, Raphael St-Gelais, Alexandre Poulin, and Yves-Alain Peter. Tunable fiber laser using a mems-based in plane fabry-pérot filter. *IEEE Journal of Quantum Electronics*, 46(9):1313–1319, 2010.

44. Michael J Thorpe, David Balslev-Clausen, Matthew S Kirchner, and Jun Ye. Cavity-enhanced optical frequency comb spectroscopy: application to human breath analysis. *Optics Express*, 16(4):2387–2397, 2008.

45. R St-Gelais, J Masson, and Y-A Peter. All-silicon integrated fabry–pérot cavity for volume refractive index measurement in microfluidic systems. *Applied physics letters*, 94(24):243905, 2009.

46. Marco Pisani and Massimo Zucco. Compact imaging spectrometer combining fourier transform spectroscopy with a fabry-perot interferometer. *Optics express*, 17(10):8319–8331, 2009.

47. WZ Song, XM Zhang, AQ Liu, CS Lim, PH Yap, and Habib Mir M Hosseini. Refractive index measurement of single living cells using on-chip fabry-pérot cavity. *Applied physics letters*, 89(20):203901, 2006.

48. Yves Colombe, Tilo Steinmetz, Guilhem Dubois, Felix Linke, David Hunger, and Jakob Reichel. Strong atom–field coupling for bose–einstein condensates in an optical cavity on a chip. *Nature*, 450(7167):272–276, 2007.

49. Sébastien Garcia, Francesco Ferri, Konstantin Ott, Jakob Reichel, and Romain Long. Dual-wavelength fiber fabry-perot cavities with engineered birefringence. *Optics express*, 26(17):22249–22263, 2018.

50. Manuel Uphoff, Manuel Brekenfeld, Gerhard Rempe, and Stephan Ritter. Frequency splitting of polarization eigenmodes in microscopic fabry–perot cavities. *New Journal of Physics*, 17(1):013053, 2015.

51. H Snijders, JA Frey, J Norman, VP Post, AC Gossard, JE Bowers, MP van Exter, W Löffler, and D Bouwmeester. Fiber-coupled cavity-qed source of identical single photons. *Physical Review Applied*, 9(3):031002, 2018.

52. Xuan Liu, Iulian I Iordachita, Xingchi He, Russell H Taylor, and Jin U Kang. Miniature fiber-optic force sensor based on low-coherence fabry-pérot interferometry for vitreoretinal microsurgery. *Biomedical optics express*, 3(5):1062–1076, 2012.

53. Jun-long Kou, Jing Feng, Liang Ye, Fei Xu, and Yan-qing Lu. Miniaturized fiber taper reflective interferometer for high temperature measurement. *Optics express*, 18(13):14245–14250, 2010.

54. Jaehoon Jung, Hui Nam, Byoungho Lee, Jae Oh Byun, and Nam Seong Kim. Fiber bragg grating temperature sensor with controllable sensitivity. *Applied optics*, 38(13):2752–2754, 1999.

55. Xuefeng Li, Shuo Lin, Jinxing Liang, Hiroshi Oigawa, and Toshitsugu Ueda. High-sensitivity fiber-optic fabry–perot interferometer temperature sensor. *Japanese Journal of Applied Physics*, 51(6S):06FL10, 2012.

56. Onur Kilic, Michel Digonnet, Gordon Kino, and Olav Solgaard. External fibre fabry–perot acoustic sensor based on a photonic-crystal mirror. *Measurement Science and Technology*, 18(10):3049, 2007.

57. Zeng Ling Ran, Yun Jiang Rao, Wei Jun Liu, X Liao, and Kin Seng Chiang. Laser-micromachined fabry-perot optical fiber tip sensor for high-resolution temperature-independent measurement of refractive index. *Optics express*, 16(3):2252–2263, 2008.

58. Jun-long Kou, Jing Feng, Liang Ye, Fei Xu, and Yan-qing Lu. Miniaturized fiber taper reflective interferometer for high temperature measurement. *Optics express*, 18(13):14245–14250, 2010.

59. Bing Sun, Yiping Wang, Junle Qu, Changrui Liao, Guolu Yin, Jun He, Jiangtao Zhou, Jian Tang, Shen Liu, Zhengyong Li, et al. Simultaneous measurement of pressure and temperature by employing fabry-perot interferometer based on pendant polymer droplet. *Optics express*, 23(3):1906–1911, 2015.

60. Min Li, Yi Liu, Renxi Gao, Yan Li, Xiuli Zhao, and Shiliang Qu. Ultracompact fiber sensor tip based on liquid polymer-filled fabry-perot cavity with high temperature sensitivity. *Sensors and Actuators B: Chemical*, 233:496–501, 2016.

61. Mian Yao, Xia Ouyang, Jushuai Wu, A Ping Zhang, Hwa-Yaw Tam, and PKA Wai. Optical fiber-tip sensors based on in-situ μ-printed polymer suspended-microbeams. *Sensors*, 18(6):1825, 2018.

62. Jiajun Tian, Yujie Lu, Qi Zhang, and Ming Han. Microfluidic refractive index sensor based on an all-silica in-line fabry–perot interferometer fabricated with microstructured fibers. *Optics express*, 21(5):6633–6639, 2013.

63. Mian Yao, Xia Ouyang, Jushuai Wu, A Ping Zhang, Hwa-Yaw Tam, and PKA Wai. Optical fiber-tip sensors based on in-situ μ-printed polymer suspended-microbeams. *Sensors*, 18(6):1825, 2018.

64. Hui Wang, Zhenwei Xie, Mile Zhang, Hailin Cui, Jingsuo He, Shengfei Feng, Xinke Wang, Wenfeng Sun, Jiasheng Ye, Peng Han, et al. A miniaturized optical fiber microphone with concentric nanorings grating and microsprings structured diaphragm. *Optics & Laser Technology*, 78:110–115, 2016.

65. Radhika K Poduval, Jo Coote, Charles A Mosse, Malcolm C Finlay, Ioannis Papakonstantinou, and Adrien E Desjardins. 3d printed micro-scale fiber optic probe for intravascular pressure sensing. In *Biosensing and Nanomedicine XI*, volume 10728, page 107280B. International Society for Optics and Photonics, 2018.

66. Radhika K Poduval, Jo Coote, Charles A Mosse, Malcolm C Finlay, Ioannis Papakonstantinou, and Adrien E Desjardins. 3d printed micro-scale fiber optic probe for intravascular pressure sensing. In *Biosensing and Nanomedicine XI*, volume 10728, page 107280B. International Society for Optics and Photonics, 2018.

67. Stacy Wise, G Mueller, D Reitze, DB Tanner, and Bernard F Whiting. Linewidth-broadened fabry–perot cavities within future gravitational wave detectors. *Classical and Quantum Gravity*, 21(5):S1031, 2004.

68. Kazem Zandi, Joseph André Bélanger, and Yves-Alain Peter. Design and demonstration of an in-plane silicon-on-insulator optical mems fabry–pérot-based accelerometer integrated with channel waveguides. *Journal of Microelectromechanical systems*, 21(6):1464–1470, 2012.

69. Mingran Quan, Jiajun Tian, and Yong Yao. Ultra-high sensitivity fabry–perot interferometer gas refractive index fiber sensor based on photonic crystal fiber and vernier effect. *Optics letters*, 40(21):4891–4894, 2015.

70. Eric Udd and William B Spillman Jr. *Fiber optic sensors: an introduction for engineers and scientists*. John Wiley & Sons, 2011.

71. Gerd Keiser. *Optical Fiber Communications, 2e*. McGraw-Hill Science, Engineering & Mathematics, 1991.

72. Peter J Winzer, David T Neilson, and Andrew R Chraplyvy. Fiber-optic transmission and networking: the previous 20 and the next 20 years. *Optics express*, 26(18):24190–24239, 2018.

73. Daiki Soma, Yuta Wakayama, Shohei Beppu, Seiya Sumita, Takehiro Tsuritani, Tetsuya Hayashi, Takuji Nagashima, Masato Suzuki, Masato Yoshida, Keisuke Kasai, et al. 10.16-peta-b/s dense sdm/wdm transmission over 6-mode 19-core fiber across the c+ l band. *Journal of Lightwave Technology*, 36(6):1362–1368, 2018.

74. Kwang-Sup Lee, Ran Hee Kim, Dong-Yol Yang, and Sang Hu Park. Advances in 3d nano/microfabrication using two-photon initiated polymerization. *Progress in Polymer Science*, 33(6):631–681, 2008.

75. Andreas Ostendorf and Boris N Chichkov. Two-photon polymerization: a new approach to micromachining. *Photonics spectra*, 40(10):72, 2006.

76. Muamer Kadic, Graeme W Milton, Martin van Hecke, and Martin Wegener. 3d metamaterials. *Nature Reviews Physics*, 1(3):198–210, 2019.

77. Hong Xia, Juan Wang, Ye Tian, Qi-Dai Chen, Xiao-Bo Du, Yong-Lai Zhang, Yan He, and Hong-Bo Sun. Ferrofluids for fabrication of remotely controllable micro-nanomachines by two-photon polymerization. *Advanced Materials*, 22(29):3204–3207, 2010.

78. Maciej Kowalczyk, Jakub Haberko, and Piotr Wasylczyk. Microstructured gradient-index antireflective coating fabricated on a fiber tip with direct laser writing. *Optics express*, 22(10):12545–12550, 2014.

79. Hannah West, Yehudit Garcia, Lior Rechtman, Miri Blau, and Dan M Marom. Subwavelength nano-pyramids 3d printed directly on optical fiber tip serving as anti-reflection coating. In *2018 International Conference on Optical MEMS and Nanophotonics (OMN)*, pages 1–5. IEEE, 2018.

80. Timo Gissibl, Simon Thiele, Alois Herkommer, and Harald Giessen. Two-photon direct laser writing of ultracompact multi-lens objectives. *Nature Photonics*, 10(8):554, 2016.

81. Silvio Bianchi, VP Rajamanickam, Lorenzo Ferrara, E Di Fabrizio, Carlo Liberale, and Roberto Di Leonardo. Focusing and imaging with increased numerical apertures through multimode fibers with micro-fabricated optics. *Optics letters*, 38(23):4935–4938, 2013.

82. Timo Gissibl, Simon Thiele, Alois Herkommer, and Harald Giessen. Sub-micrometre accurate free-form optics by three-dimensional printing on single-mode fibres. *Nature Communications*, 7(1):1–9, 2016.

83. Siyao Zhang, Shui-Jing Tang, Shengfei Feng, Yun-Feng Xiao, Wanyin Cui, Xinke Wang, Wenfeng Sun, Jiasheng Ye, Peng Han, Xinping Zhang, et al. High-q polymer microcavities integrated on a multicore fiber facet for vapor sensing. *Advanced Optical Materials*, 7(20):1900602, 2019.

84. Andrea Bertoncini and Carlo Liberale. Polarization micro-optics: circular polarization from a fresnel rhomb 3d printed on an optical fiber. *IEEE Photonics Technology Letters*, 30(21):1882–1885, 2018.

85. C Liberale, E Di Fabrizio, G Cojoc, G Perozziello, P Candeloro, F Bragheri, L Ferrara, P Minzioni, and I Cristiani. Optical fiber tweezers fabricated by two photon lithography. In *The European Conference on Lasers and Electro-Optics*, page CLEB5_6. Optical Society of America, 2011.

86. Ivan Martincek, Matej Goraus, and Daniel Kacik. Polymer photonic structures for lab-on-a-fiber applications. In *21st Czech-Polish-Slovak Optical Conference on Wave and Quantum Aspects of Contemporary Optics*, volume 10976, page 109760W. International Society for Optics and Photonics, 2018.

87. M Goraus, I Martincek, and D Pudis. 3d polymer based fabry-pérot interferometer for lab-on-fiber applications. In *2018 12th International Conference on Advanced Semiconductor Devices and Microsystems (ASDAM)*, pages 1–4. IEEE, 2018.

88. Boonsong Sutapun, Massood Tabib-Azar, and Alex Kazemi. Pd-coated elastooptic fiber optic bragg grating sensors for multiplexed hydrogen sensing. *Sensors and Actuators B: Chemical*, 60(1):27–34, 1999.

89. HJ Patrick, GM Williams, AD Kersey, JR Pedrazzani, and AM Vengsarkar. Hybrid fiber bragg grating/long period fiber grating sensor for strain/temperature discrimination. *IEEE Photonics Technology Letters*, 8(9):1223–1225, 1996.

90. Athanasios N Chryssis, Sang M Lee, Sang B Lee, Simarjeet S Saini, and Mario Dagenais. High sensitivity evanescent field fiber bragg grating sensor. *IEEE Photonics Technology Letters*, 17(6):1253–1255, 2005.

91. Yong Zhao, Peng Wang, Riqing Lv, and Xu Liu. Highly sensitive airflow sensor based on fabry–perot interferometer and vernier effect. *Journal of Lightwave Technology*, 34(23):5351–5356, 2016.

92. Onur Kilic, Michel Digonnet, Gordon Kino, and Olav Solgaard. External fibre fabry–perot acoustic sensor based on a photonic-crystal mirror. *Measurement Science and Technology*, 18(10):3049, 2007.

93. Jose A Garcia, David Monzón-Hernández, Oswaldo Cuevas, Berenice Noriega-Luna, and Erika Bustos. Optical fiber detector for monitoring volatile hydrocarbons during electrokinetic treatment of polluted soil. *Journal of Chemical Technology & Biotechnology*, 91(8):2162–2169, 2016.

94. Onur Kilic, Michel Digonnet, Gordon Kino, and Olav Solgaard. External fibre fabry–perot acoustic sensor based on a photonic-crystal mirror. *Measurement Science and Technology*, 18(10):3049, 2007.

95. Onur Kilic, Michel Digonnet, Gordon Kino, and Olav Solgaard. External fibre fabry–perot acoustic sensor based on a photonic-crystal mirror. *Measurement Science and Technology*, 18(10):3049, 2007.

96. H Bae, XM Zhang, H Liu, and M Yu. Miniature surface-mountable fabry–perot pressure sensor constructed with a 45 angled fiber. *Optics letters*, 35(10):1701–1703, 2010.

97. Cheng-Ling Lee, Kai-Wen Liu, Shi-Hong Luo, Meng-Shan Wu, and Chao-Tsung Ma. A hot-polymer fiber fabry–pérot interferometer anemometer for sensing airflow. *Sensors*, 17(9):2015, 2017.

98. Guigen Liu, Weilin Hou, Wei Qiao, and Ming Han. Fast-response fiber-optic anemometer with temperature self-compensation. *Optics express*, 23(10):13562–13570, 2015.

99. Rongzhang Chen, Aidong Yan, Qingqing Wang, and Kevin P Chen. Fiber-optic flow sensors for high-temperature environment operation up to 800 c. *Optics letters*, 39(13):3966–3969, 2014.

100. Ying Li, Guofeng Yan, Liang Zhang, and Sailing He. Microfluidic flowmeter based on micro "hot-wire" sandwiched fabry-perot interferometer. *Optics Express*, 23(7):9483–9493, 2015.

101. Yong Zhao, Peng Wang, Riqing Lv, and Xu Liu. Highly sensitive airflow sensor based on fabry–perot interferometer and vernier effect. *Journal of Lightwave Technology*, 34(23):5351–5356, 2016.

102. Chao Wang, Xuezhi Zhang, Junfeng Jiang, Kun Liu, Shuang Wang, Rundong Wang, Yuanyao Li, and Tiegen Liu. Fiber optical temperature compensated anemometer based on dual fabry-perot sensors with sealed cavity. *Optics express*, 27(13):18157–18168, 2019.

103. Rong Ping Hu and Xu Guang Huang. A simple fiber-optic flowmeter based on bending loss. *IEEE Sensors journal*, 9(12):1952–1955, 2009.

104. Mohammad H Bitarafan and Ray G DeCorby. On-chip high-finesse fabry-perot microcavities for optical sensing and quantum information. *Sensors*, 17(8):1748, 2017.

105. Kwang-Yu Chu and A Ralph Thompson. Densities and refractive indices of alcohol-water solutions of n-propyl, isopropyl, and methyl alcohols. *Journal of chemical and engineering data*, 7(3):358–360, 1962.

106. Nur Ismail, Cristine Calil Kores, Dimitri Geskus, and Markus Pollnau. Fabry-pérot resonator: spectral line shapes, generic and related airy distributions, linewidths, finesses, and performance at low or frequency-dependent reflectivity. *Optics express*, 24(15):16366–16389, 2016.

107. Thomas Christopoulos, Odysseas Tsilipakos, Georgios Sinatkas, and Emmanouil E Kriezis. On the calculation of the quality factor in contemporary photonic resonant structures. *Optics express*, 27(10):14505–14522, 2019.

108. Ivana Suchy. *Handbook of die design*, volume 1998. McGraw-Hill New York, 2006.

109. J.D. Anderson. *Fundamentals of Aerodynamics*. McGraw-Hill Education, 2010.

Acronyms

2PP two-photon polymerization. viii, ix, xi, xviii, 1, 3, 4, 5, 11, 16, 17, 18, 19, 20, 23, 24, 26, 27, 28, 31, 38, 42, 45, 47, 71, 72, 78, 79, 82, 88, 90, 97

AFIT Air Force Institute of Technology. 2, 4, 35, 36

AFRL Air Force Research Laboratory. 2, 3

ALD atomic layer deposition. 26, 35

CAD computer aided design. 43

CCD charge coupled device. 29

CFD computation fluid dynamics. 94, 110

CMOS complementary metal oxide semiconductor. viii, 17, 18, 26, 71

CNTs carbon nanotubes. 29

CQED cavity quantum electrodynamics. 11

CVD chemical vapor deposition. 26

EM electromagnetic. 15, 22

FBG fiber Bragg grating. viii, 21, 22

FEA finite element analysis. xviii, 85, 87, 88

FIB focussed ion beam. ix, 24, 25

FIS Fiber Instrument Sales. 51

FP Fabry–Pérot. viii, ix, x, xi, xviii, 5, 6, 7, 8, 9, 10, 11, 12, 19, 20, 22, 23, 24, 25, 26, 27, 28, 29, 31, 32, 33, 35, 37, 38, 40, 41, 42, 46, 48, 49, 53, 54, 55, 58, 59, 60, 61, 63, 67, 70, 71, 72, 73, 75, 81, 82, 87, 88

fs femtosecond. 29, 43

FSR free spectral range. xiv, 9, 11, 32, 34, 37, 38, 58, 59, 60, 82, 83, 84

FWHM full-width half-max. 9

HCF hollow core fiber. viii, 22, 23, 26

HF hydroflouric acid. ix, 24, 25

IPA Isopropyl Alcohol. 46, 52, 60, 61

MEMS Micro-Electro-Mechanical Systems. 11, 17, 71, 72

NIST National Institute of Standards and Technology. 34, 66

PCF photonic crystal fiber. 22

PGMEA propylene glycol methyl ether acetate. 46

RI refractive index. viii, ix, xi, xii, xiii, xviii, 2, 5, 6, 7, 8, 9, 10, 11, 12, 13, 20, 21, 22, 23, 24, 27, 28, 31, 32, 33, 34, 35, 38, 48, 52, 58, 59, 60, 61, 62, 63, 64, 65, 68, 69, 70, 71, 72, 73, 75, 78, 79, 80, 81, 82, 83, 85, 86, 87, 88

SEM scanning electron microscope. viii, ix, xiv, 5, 6, 32, 37, 90, 97

SMF single mode fiber. 14, 22, 31

SWAP size, weight, and power. 1, 5, 15, 27, 109

UAVs unmanned aerial vehicles. 3

UV ultraviolet. viii, 16, 17

WGM whispering gallery mode. 9, 19, 27

WPAFB Wright-Patterson Air Force Base. 2

REPORT DOCUMENTATION PAGE

Form Approved
OMB No. 0704–0188

1. REPORT DATE *(DD–MM–YYYY)*	2. REPORT TYPE	3. DATES COVERED *(From — To)*
26–03–2020	Master's Thesis	Sept 2018 — Mar 2020

4. TITLE AND SUBTITLE

Dynamic Micromechanical Fabry–Pérot Cavity Sensors Fabricated by Multiphoton Absorption Onto Optical Fiber Tips with a Second Line

5a. CONTRACT NUMBER

5b. GRANT NUMBER

5c. PROGRAM ELEMENT NUMBER

6. AUTHOR(S)

Williams, Jeremiah C, 2d LT, USAF

5d. PROJECT NUMBER

5e. TASK NUMBER

5f. WORK UNIT NUMBER

7. PERFORMING ORGANIZATION NAME(S) AND ADDRESS(ES)

Air Force Institute of Technology
Graduate School of Engineering and Management (AFIT/EN)
2950 Hobson Way
WPAFB OH 45433-7765

8. PERFORMING ORGANIZATION REPORT NUMBER

AFIT-ENG-MS-20-M-074

9. SPONSORING / MONITORING AGENCY NAME(S) AND ADDRESS(ES)

Air Force Office of Scientific Research
875 North Randolph Street, Suite 325 Arlington, VA 22203

10. SPONSOR/MONITOR'S ACRONYM(S)

AFOSR

11. SPONSOR/MONITOR'S REPORT NUMBER(S)

12. DISTRIBUTION / AVAILABILITY STATEMENT

DISTRIBUTION STATEMENT A:
APPROVED FOR PUBLIC RELEASE; DISTRIBUTION UNLIMITED.

13. SUPPLEMENTARY NOTES

14. ABSTRACT

This research leveraged two-photon polymerization microfabrication to integrate dynamic mechanical components with Fabry-Perot resonators onto the ends of low-loss optical fibers to prototype 3 micro-optic devices. The first device featured a multi-positional mirror that enabled thin-film deposition onto cavities of any length with mirrors of significant curvature, for refractive index sensing. The second device combined an FP cavity with a spring body featuring easily scalable stiffness for pressure sensing. The third device presented a high-speed rotating micro-anemometer for measuring a wide range of gas flows. All devices represent a significant reduction in size and weight over commercially available devices.

15. SUBJECT TERMS

Fabry-Perot Cavity (FPC), Two-Photon Polymerization (2PP), Optical Fiber Tip Sensor, Micro-Optoelectromechanical Systems (MOEMS)

16. SECURITY CLASSIFICATION OF:			17. LIMITATION OF ABSTRACT	18. NUMBER OF PAGES	19a. NAME OF RESPONSIBLE PERSON
a. REPORT	b. ABSTRACT	c. THIS PAGE			Dr. Hengky Chandrahalim, AFIT/ENG
U	U	U	UU	167	19b. TELEPHONE NUMBER *(include area code)* (312) 785-3636 x4483; hengky.chandrahalim@afit.edu